UNIVERSITY OF BIRMINGHAM

Behaviour, optimisation and design of cold-formed steel purlins

A thesis submitted to University of Birmingham

for the degree of Doctor of Philosophy.

By

Meshal Almatrafi

School of Civil Engineering

University of Birmingham

Birmingham B15 2TT

United Kingdom

May 2021

UNIVERSITY OF BIRMINGHAM

University of Birmingham Research Archive

e-theses repository

Abstract

Purlins are arguably the most widely used cold-formed steel members in construction. They are employed as secondary steelwork to support roof cladding, transfer loads and offer effective restraint to the primary steel members. Owing to their thin-walled nature, they are susceptible to a variety of instabilities including local, distortional, lateral torsional buckling or interactions thereof. Currently, most cold-formed producers try to optimise their cross-section geometries to achieve maximum strength with minimum material usage and hence gain a competitive advantage in the construction market. Furthermore, most producers can customise their cross-sections on demand to suit a particular application and hence expand the scope of application for their products. Therefore, determining optimal cross-section shapes as well as the pertinent dimensions of the various parts of a cross-section for a given shape for cold-formed steel members, is a topic of great interest.

The aim of this thesis is to assess current and propose novel design approaches for cold-formed steel purlins. To this end a series of experimental tests and numerical analyses is performed focusing on the structural response of purlins subjected to loads likely to occur in practical applications. Since purlins are commonly restrained by cladding, only their cross-sectional response will be considered in this project. The failure modes considered include local and distortional buckling as well as web crippling, whilst the studied cross-section shapes are Z and Sigma purlins. Z purlins are particularly susceptible to local and distortional buckling due to their deep flat web; hence these failure modes are studied in great detail. In addition to generating structural performance data, an attempt to optimise the sections is also reported. To this end, a series of 8 tests followed by numerical investigations for a wide range of Z-

sections have been conducted. It was found that for most of sections, small lip size to flange width ratios (i.e. d/b ≤ 0.28) leads to decreased efficiency by about 8%, whilst lip size to flange width ratios above 0.4 leads to improved efficiencies particularly for deeper sections, for which gains in the region of 5% can be achieved. Furthermore, the obtained experimental and numerical results are used to assess the accuracy of the design predictions of Eurocode 3 and the Direct strength method (DSM). On the other hand, Sigma sections employ a non-flat web which offers greater strength against local and distortional buckling at the expense of reduced resistance to web crippling. Furthermore, Eurocode 3 does not currently cover the design resistance of sigma sections to web crippling, thereby necessitating the development of a novel design approach. A series of six tests was performed on sigma purlins subjected to interior one flange loading. A numerical model was generated and validated against experimental results. Upon validation of the numerical model, parametric studies were conducted to generate additional data considering a wide range of cross-section geometries. Using the obtained results, the North American specifications was assessed and found to be unsafe for sigma sections, thus a modification was proposed. A recently proposed design framework based on cross-section slenderness was successfully extended to sigma sections.

Acknowledgements

First and foremost, I am extremely grateful to my primary supervisor, Dr Marios Theofanous, for his invaluable advice, continuous support, and patience during my PhD study. Without him this thesis would never be completed.

I would also like to thank my second supervisor, Dr Samir Dirar, for his help and advice throughout my journey.

The support of the technicians in the Civil Engineering Laboratory at University of Birmingham, where the experimental programmes presented in this thesis were conducted, is very gratefully acknowledged.

The supply of specimens and financial support from Albion Sections Ltd is very gratefully acknowledged. I would also like to thank Mr Thomas Jarvis and Mr Rodrigo Carles for their involvement in the experimental part of this thesis. I would like to thank the Saudi Arabian Cultural Bureau and Umm Al Qura University for sponsoring my doctoral studies.

Finally, I would like to express my gratitude to my family, without their tremendous understanding and encouragement in the past few years, it would be impossible for me to finish my study.

Author's publications

The present PhD thesis has led to the following journal and conference publications listed below:

Journal papers:

1- Almatrafi M., Theofanous M., Bock M., Dirar S. (2021). Slenderness-based design for sigma sections subjected to interior one flange loading. Thin-Walled Structures, 158, 107194.

2- Almatrafi M., Theofanous M., Dirar S., Gkantou M. (2021). Structural response of cold-formed lipped Z purlins – Part 1: Experimental investigation. Thin-Walled Structures, 161, 107452.

3- Almatrafi M., Theofanous M., Dirar S., Bock M. (2021). Structural response of cold-formed lipped Z purlins – Part 2 numerical modelling and optimisation. Thin-Walled Structures, 161, 107453.

Conference papers:

1- Almatrafi M., Theofanous M., Dirar S. (2021). Numerical modelling and optimisation of cold-formed steel purlins. In: The 9th European Conference on Steel and Composite Structures, Sheffield, UK.

2- Almatrafi M., Theofanous M., Bock M., Dirar S. (2021). Web Crippling Behaviour of Sigma Purlins. In: The 9th European Conference on Steel and Composite Structures, Sheffield, UK.

Contents

List of Figures

List of Tables

Chapter 1: Introduction

1.1 Background

There are two main types of production for structural members in steel construction, hot-rolling (HR) and cold-forming (CF) with the main different between them being the temperature during the manufacturing process. Hot-rolled steel members are produced at high temperatures thus allowing steel members to be formed into the desired shape via successive passing through rollers which gradually transform a hot steel ingot into a predetermined structural shape. This production method is suitable for large volume production of thick sections with a simple geometry. Cold-formed steel sections are produced at room temperature via press-braking or cold-rolling of relatively this steel sheets into the desired structural shape. Cold-forming or cold-rolling is suitable for the production of thin-walled open sections often having a complex cross-section geometry (Doran and Cather, 2013). Cold-formed steel members have been first used in industry in the 1850's and became extensively utilized in construction since the 1940s (Yu et al., 2010). They are commonly employed as secondary members supporting cladding (e.g. purlins and side rails) or primary structural members not necessitating the use of a heave steel profile like floor joists.

Cold-formed steel structural members are further categorised into two types, long products used as structural framing members and panels or decks used for wall panel, roofing, bridge forms, flooring and siding materials (Yu et al., 2010). Carrying load is the main function of individual structural framing members thus the main consideration in their design is structural strength and stiffness (Yu et al., 2010). Figures 1.1 illustrates some typical cold-formed steel shapes unitised in structural framing. Typical

shapes of panels, decks and profiled sheets linear trays are illustrated in Figure 1.2 (Dubina et al., 2012).
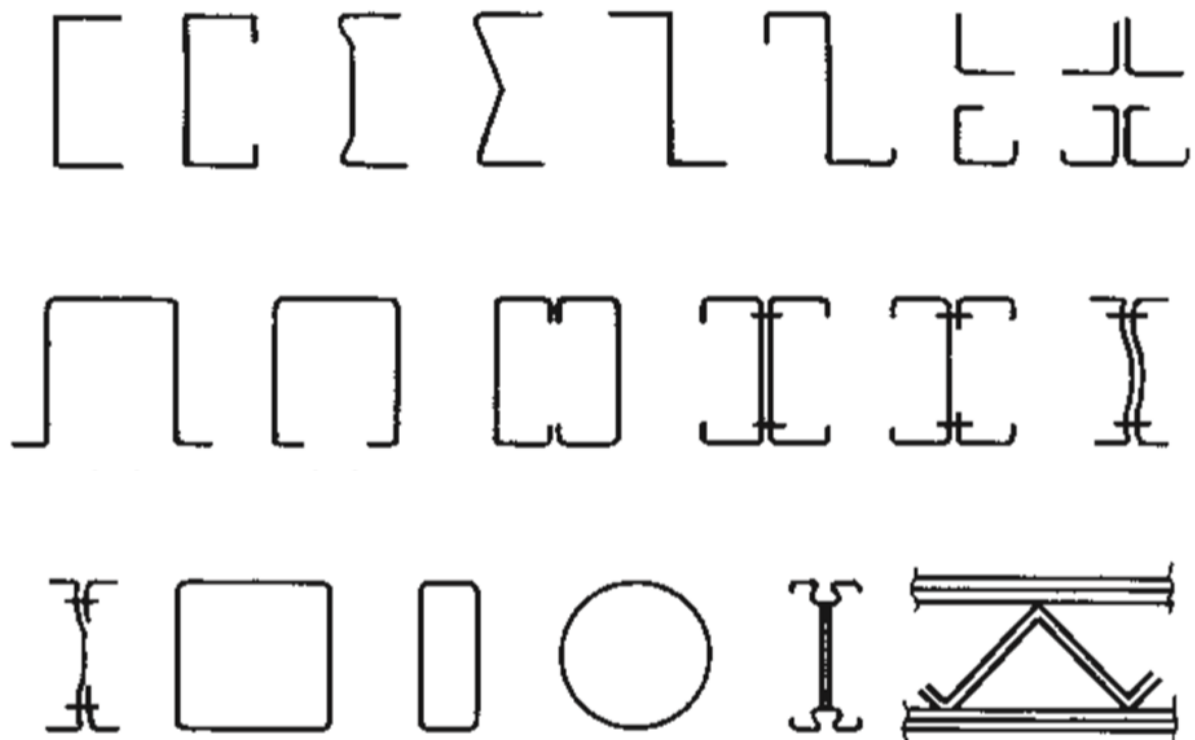
Figure 1.1 Common cold-formed steel shapes (Yu et al., 2010).
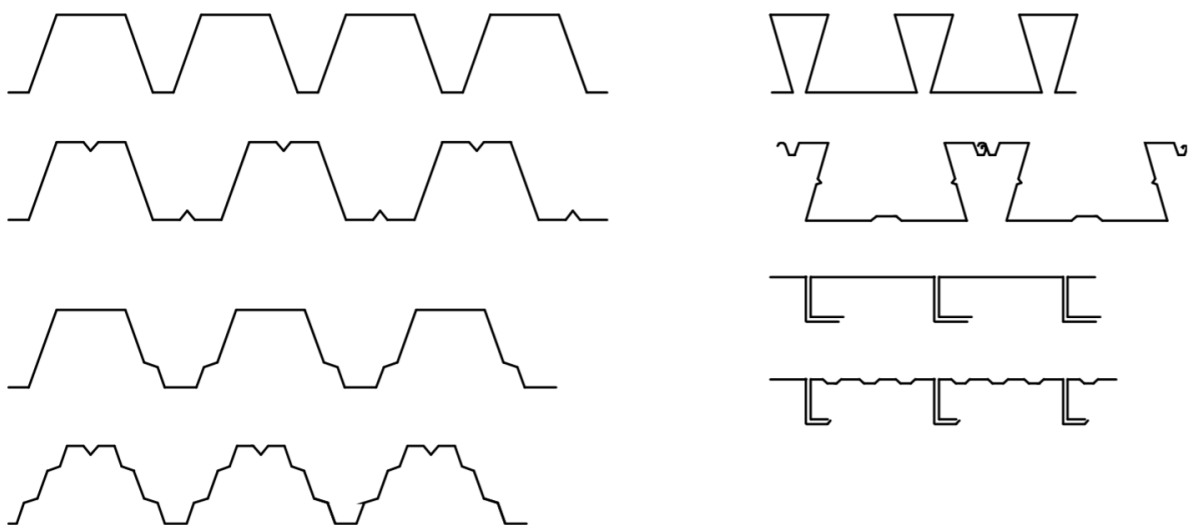
Figure 1.2 Profiled sheets and linear trays (Dubina et al., 2012).

In terms of stiffness and strength cold-formed steel members are efficient since they are made from thin steel which leads to light weight members with high strength (Dubina et al., 2012). However, their thin-walled nature makes cold-formed steel members susceptible to several cross-section instabilities such as local (L) and distortional (D) buckling as well as member instabilities such as lateral-torsional buckling (LTB) for laterally unrestrained flexural members (Martins et al., 2017b). Depending on length, loading arrangement, support conditions and cross-sectional geometry any of these buckling modes and interactions thereof may be critical (Van der Neut, 1969). In addition to their high strength to weight ratio, the ease of installation and transport, their enhanced performance, economy and flexibility in fabricating cross-sectional forms and sizes (Yu and Schafer, 2006) are additional advantages that have increased the popularity.

Nowadays, most of the cold-formed producers are able to customize any cross-section on demand and employ it in a specific application. Accordingly, finding optimal profiles or sizes for cold-formed steel members, which provides effective and economical solutions, is a topic of great interest (Leng et al., 2011). In structural engineering, cross-section optimisation means the minimisation of used materials by reducing the weight while fulfilling strength and serviceability constraints. Generally, cross-section optimization approaches can be categorized into two types, namely shape optimisation and size optimisation (Ye et al., 2016). The first is aiming to determine an optimal cross-sectional form with no initial constraints on its shape while the second is aiming to determine an optimal relative size for a defined profile. Significant research have been conducted on shape optimisation (Liu et al., 2004, Moharrami et al., 2014, Leng et al., 2014). In addition, size optimisation has also been studied by many

researchers for several conventional CF steel section geometries such as Z, hat and I-section (Adeli and Karim, 1997; Lee et al., 2005, Lee et al., 2006).

1.2 Aim and objectives

The aim of this thesis is to fill in current gaps in knowledge in the design and behaviour of cold-formed steel purlins subjected to bending and/or concentrated loads. Due to the susceptibility of sigma sections to web crippling and of Z-sections to local and/or distortional buckling, this project studies Z-sections subjected only to bending moments and Sigma sections subjected only to concentrated forces.

To achieve this aim the following objectives need to be met:

- Carry out experimental tests on cold-formed steel purlins to generate fundamental structural performance data.

- Develop and validate FE models against experimental results.

- Generate additional structural performance data that will allow the effect of key parameters such as aspect ratio, cross-section slenderness and cross-section geometry, on the strength to be determined.

- Based on the numerical results, optimise cross-section geometry of Z purlins to maximise the design resistance.

- Assess the accuracy of current codified design guidance based on the generated experimental and numerical results.

- Propose a novel design approach to improve strength predictions of sigma section and facilitate efficient design in line with the observed response.

1.3 Outline of the thesis

This thesis is organised in six chapters. Chapter 1 outlines a brief background of cold-formed steel and its applications in construction industry. Additionally, the aims and objectives of the research and the outline of the thesis are set out in this chapter.

Chapter 2 presents a literature review discussing the available research findings on the structural testing, numerical modelling, structural response and design of cold-formed steel purlins, with the focus lying on local, distortional buckling and web crippling behaviour of flexural members and the current design standards for cold-formed steel. In this chapter, the shortcomings of published research are highlighted, and gaps of knowledge that lead to this thesis project are identified. Furthermore, the experimental testing and numerical modelling procedures adopted in later chapters are informed by the literature review reported in Chapter 2.

In Chapter 3 an experimental investigation on simply supported purlins employing lipped Z- sections subjected to bending is reported in detail. The information about the test set up, specimen preparation, support details, loading procedure and results are provided in this chapter. Additionally, the test results are analysed, discussed and utilised to assess current design specifications, namely Eurocode 3 and the Direct Strength Method (DSM).

Chapter 4 builds upon the experimental results reported in the previous chapter by developing and validating a numerical model that accurately replicates the test results reported in Chapter 3. Chosen element type, initial geometric imperfection amplitudes as well as combination of local and distortional imperfections, employed materials properties and modelling of structural details of the numerical model are discussed. The model is validated against the test results. Extensive parametric studies are

conducted to determine the optimal lip size to flange width ration that maximises efficiency of the cross-section.

Chapter 5 reports experimental investigations on sigma sections subject to interior one flange loading. Six experimental tests are reported in detail and the obtained results are discussed.

Chapter 6 a numerical model is developed and validated against the test results reported in Chapter 5. Upon validation of the results, a comprehensive parametric study is carried out. The north American specifications NAS S100-16 (AISI, 2016) are assessed and design recommendations are proposed. Finally, the scope of a slenderness-based design approach for design against web crippling is extended to cover sigma sections.

Finally, Chapter 7 summarises the overall conclusions of the project and presents some recommendations for future work.

Chapter 2: Literature review

2.1 Cold-formed steel purlins

Purlins are among the most commonly used cold-formed steel members in construction. They are employed as secondary steelwork to support roof cladding, transfer loads and provide effective restraint to the primary steel members. Typical cross-section shapes adopted as purlins include C-sections, Z-sections and Sigma sections, which may employ lips and intermediate stiffeners of varying complexity to maximise the cross-section stiffness under the intended loading conditions. Under gravity loads, simply supported purlins can in most cases be assumed to be effectively restrained against lateral torsional buckling, since the attachment of cladding to the top flange usually provides sufficient lateral and torsional restrain to the compression flange of the purlin, hence eliminating lateral torsional buckling. However, under uplift conditions, the cladding provides only partial restrain against torsion as the tension flange is restrained and hence lateral torsional buckling tends to govern failure particularly for longer spans. Furthermore, the absence of double symmetry further complicates the structural behaviour of purlins and leads the development of complex stress fields (Vieira Jr et al., 2010).

Several researchers have studied the structural behaviour of cold-formed steel purlins experimentally and numerically with the aim of assessing current and developing new design procedures, to verify the structural response under different loading conditions or to develop novel cross-section geometries. Full scale tests on simply supported and continuous purlins employing C- and Z-sections under gravity loads have shown the effect of the location of the deck fasteners with respect to web axis on the response of C-sections (Willis and Wallace, 1990), with increasing distance of the fastener axis from the purlin web leading to improved structural response. The importance of the

spacing of the fasteners on the resulting failure mode and the corresponding failure load was demonstrated experimentally for C- and Z-sections tested in the 4-point bending configuration (Yu and Schafer, 2003). It was concluded that effective attachment of a metal deck to the purlins via closely spaced fasteners can suppress the distortional buckling failure mode and even increase the local buckling resistance. Design equations for the inelastic lateral torsional buckling strength of C and Z purlins under uplift were developed based on full-scale tests (LaBoube, 1984), whilst tests on the structural response of sigma purlins attached to a metal deck with a relatively large fixing spacing are reported in (Yang and Liu, 2012) under both gravity and uplift loading. In addition to the conventional C, Z and Sigma sections, more complex sigma sections incorporating longitudinal web stiffeners were studied experimentally and numerically (Nguyen et al., 2017a) and their improved efficiency over conventional Sigma sections as well the ability of the direct strength method (DSM), to accurately predict their response was demonstrated. The response of purlins subjected to combined axial force and biaxial bending has also been experimentally and numerically investigated and suitable design equations were proposed (Becque and Rasmussen, 2013).

2.1.1 Fabrication process

Cold-formed steel members are fabricated from steel strip or sheet, with thickness ranging from 0.3 to 6.4 mm (Yu et al., 2010), whilst within European design practice (CEN, 2006a), cold-formed steel members have a thickness ranging from 0.45 to 15 mm. Three different methods are available to manufacture cold-formed steel sections, namely press braking, folding and cold rolling. The most extensively used in constructions is the method of cold rolling, which consists of passing a strip of metal through pairs of opposing rolls to gradually form the desired profile as shown in Figure

2.1 Every pair of opposite rolls is called a stage, and contributes a specific amount of plastic deformation leading to the desired section geometry (Dubina et al., 2012). Cold-rolling can be utilised to create a variety of cold-formed sections, including square and rectangular sections, from a circular hollow section. A simple section requires few stages, while for more complex section, many stages are required. Typically, cold-rolled sections have relatively large corner radii at the intersection of their elements and because of the plastic deformation induced by the cold-rolling process, the material of the finished product usually has significantly larger yield strength and smaller ductility than the virgin material of the sheet from which the section is rolled, with maximum strength enhancements occurring in the corner regions of the cold-rolled sections.
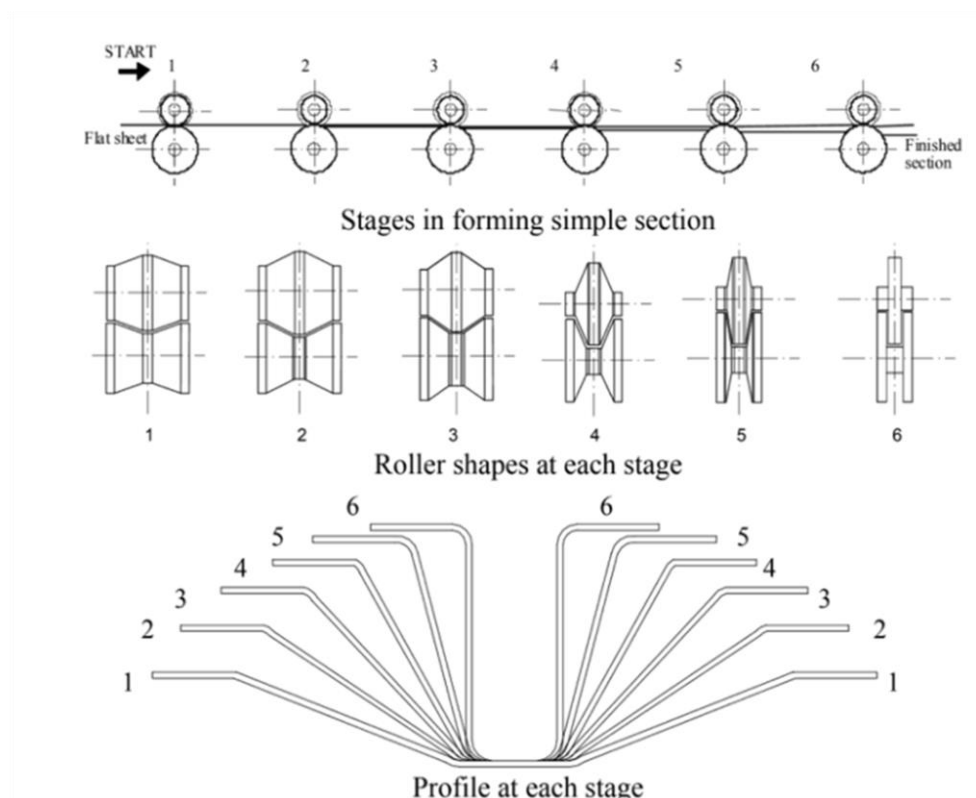
Figure 2.1 The manufacturing process of cold roll forming (Rhodes, 1991).

Press-braking is another method which can produce a diversity of cold-formed steel cross-sections by pressing a steel sheet between shaped dies in sequence, as shown in Figure 2.2, whilst folding essentially consists of a sheet of metal is folded several times until it reaches the required shape as shown in Figure 2.3. Folding is employed in a small range of applications because the method is restricted to sections of simple geometries and of short lengths (Dubina et al., 2012). Similarly, press-braking has also restrictions on sections lengths. Generally, cold roll forming is used when great quantities of a specific profile are in demand, while press braking is utilised if small quantities of various shapes are required (Dubina et al., 2012). It should also be mentioned that press-breaking results in significant corner strength enhancements that are usually confined within the corner region of the press-braked sections with the material away from the corner region not being significantly affected by press-braking.
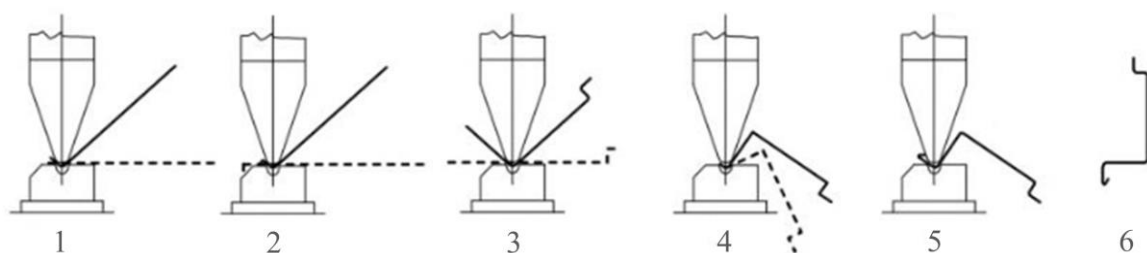
Figure 2.2 The process of press-braking (Dubina et al., 2012).
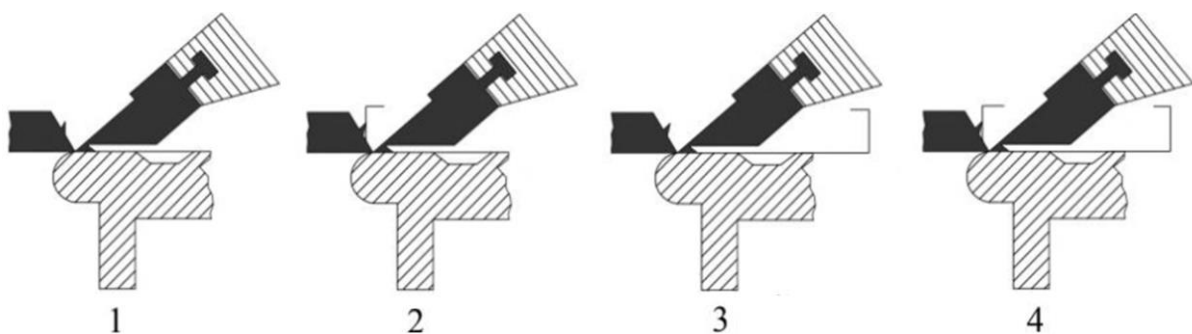
Figure 2.3 Folding process (Dubina et al., 2012).

2.1.2 Material properties

Material properties play a critical part in the behaviour of structural members, therefore, it is essential to be acquaint with the mechanical properties of steel strip and sheet prior to designing cold formed steel members (Yu et al., 2010). Generally, tensile tests are performed on material coupons extracted from the cold-formed components to determine the material response of cold-formed steel sections. Cold-formed steels usually display a rounded stress-strain response with an absence of a defined yield plateau due to cold forming process, while hot-rolled steels exhibit a well-defined yield plateau followed by strain-hardening as shown in Figure 2.4.

a   b
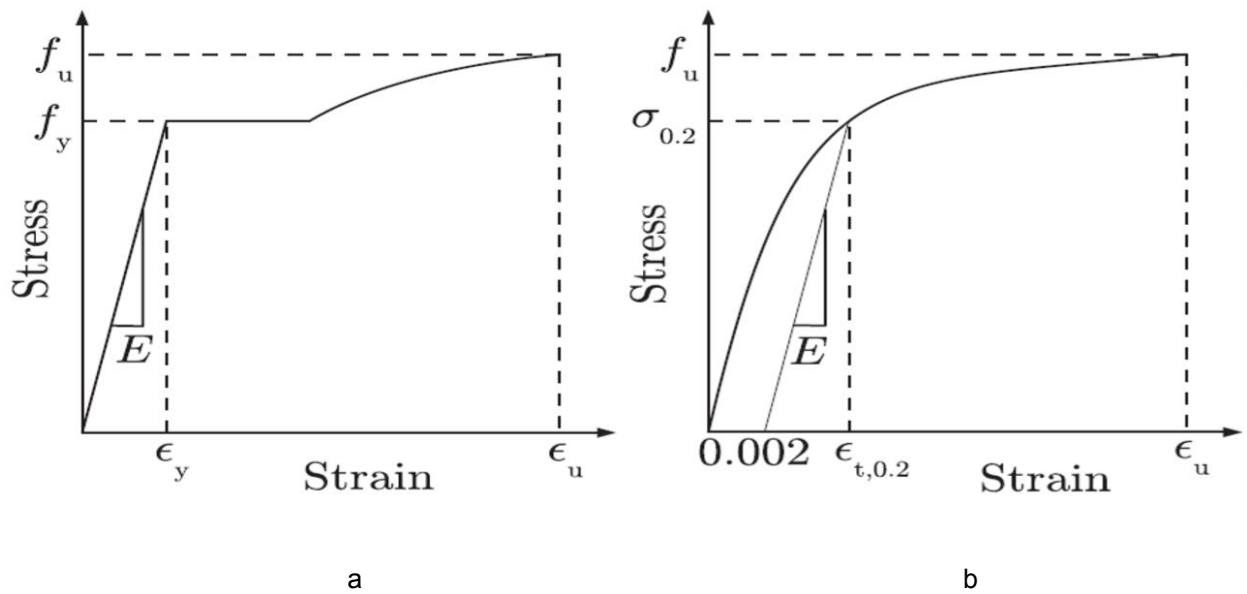
Figure 2.4 Stress strain response for a) hot-roll steels and b) cold-formed steels (Liew and Gardner, 2015).

An expression to describe the nonlinearity of stress-strain response of cold-formed steels has been proposed by Ramberg and Osgood (1943) and thereafter modified by Hill (1944) as given in Eqatuion 2.1:

$$\varepsilon = \frac{\sigma}{E} + 0.002 \, (\sigma/\sigma_{0.2})^n \tag{2.1}$$

where n is non-linear parameter, $n = \dfrac{ln(20)}{ln(\sigma_{0.2}/\sigma_{1.0})}$, E is the Young's modulus of the material and $\sigma_{0.2}$ is the proof stress corresponding to a 0.2 % plastic strain, which is conventionally adopted as a nominal yield stress for design. It should be noted that the expression of Ramberg-Osgood was initially proposed for aluminium alloys, however, it has been used for many metallic materials exhibiting a rounded material response including cold-formed steel. This expression approximates the material response reasonably well up to the nominal yield stress, but overestimates the stresses thereafter (Real et al., 2014).

Mirambell and Real (2000) introduced a two-stage Ramberg-Osgood model to approximate the material behaviour at higher stresses. Their proposal was to apply the original Ramberg-Osgood expression (Eq. 2.1) for stresses up to 0.2% proof stress and employ a similar expression with a different strain hardening exponent between 0.2% proof stress and ultimate stress (Eq. 2.2). The second stage of the material response employs two additional material parameters, namely the strain hardening exponent m and the strain at ultimate stress ε_u and has been formulated in such a way that at the transition point ($\sigma_{0.2}$) continuity of the curve and continuity of the slope of the curve is maintained. Three years later, Rasmussen (2003) based on a large amount of material response data proposed explicit predictive equations relating the additional material parameters to the three parameters of the original Ramberg-Osgood equation.

$$\varepsilon = \frac{(\sigma-\sigma_{0.2})}{E_{0.2}} + \varepsilon_u \left(\frac{\sigma-\sigma_{0.2}}{\sigma_u-\sigma_{0.2}}\right)^m + \varepsilon_{t0.2} \quad \text{For } \sigma > \sigma_{0.2} \qquad (2.2)$$

where $E_{0.2}$ is the tangent modulus at 0.2% proof stress, $E_{0.2} = \frac{E0}{1+0.002\mathrm{n}\frac{E0}{\sigma_{0.2}}}$, m is strain

hardening, $m = 1 + 3.5\frac{\sigma_{0.2}}{\sigma_u}$, σ_u is the ultimate stress, ε_u is ultimate strain $\varepsilon t_{0.2}$ is the

total strain at the 0.2% proof stress. Subsequently, Gardner and Nethercot (2004)

propose utilising the 1% proof stress instead of the ultimate stress in Equation 2.2

resulting in Equation 2.3, since the ultimate compressive strength is unable to be

obtained owing to the absence of necking phenomena.

$$\varepsilon = \frac{(\sigma - \sigma_{0.2})}{E_{0.2}} + \left(\varepsilon t_{1.0} - \varepsilon t_{0.2} - \frac{\sigma_{1.0} - \sigma_{0.2}}{E_{0.2}}\right) \times \left(\frac{\sigma - \sigma_{0.2}}{\sigma_{1.0} - \sigma_{0.2}}\right)^{\acute{\mathrm{n}}_{0.2,1.0}} + \varepsilon t_{0.2} \quad \text{For } \sigma > \sigma_{0.2} \qquad (2.3)$$

Where, $\varepsilon t_{1.0}$ is the total strain at the 1% proof stress and $\acute{\mathrm{n}}_{0.2,1.0}$ is a strain hardening

coefficient representing a curve that passes through $\sigma_{0.2}$ and $\sigma_{1.0}$. The two stage

Ramberg Osgood material model originally proposed by Ramberg and Osgood (1943),

given by Equation 2.1, and modified by Gardner and Nethercot (2004), as defined by

Equation 2.3, for the 1st and 2nd stage respectively, is adopted for the material

modelling of cold-formed sections in this thesis. More advanced material models

involving three (Quach et al., 2008) or more stages (Rossi et al., 2014) have also been

proposed for other nonlinear metallic materials but their scope of application is not

relevant for this project.

2.1.3 Corner strength enhancements

Due to the cold rolling process the yield stress and, to a lesser extent, the ultimate strength increase in the corner regions of cold-rolled sections, while they only increase in the corners when the press braking method is used (Rhodes, 1991). Consequently, the flat portion of the cross-section normally yields before the corner parts. Strain hardening and plastic deformation during the fabrication process is the cause of the observed yield strength increase, while the increase of ultimate strength, which is accompanied by a reduction in ductility, is attributed to strain aging (Dubina et al., 2012). Corner strength enhancement of cold formed carbon steel was first investigated by Karren (1967) who proposed a semi-empirical model, to determine the increase in the corner strength based on considerable amount of available test data as given by Equations 2.4.

$$\sigma_{0.2,c} = \frac{B_c}{(r_i/t)^\alpha} \sigma_{0.2,v} \tag{2.4a}$$

$$B_c = 3.96 \left(\frac{\sigma_{u,v}}{\sigma_{0.2,v}} \right) - 0.819 \left(\frac{\sigma_{u,v}}{\sigma_{0.2,v}} \right)^2 - 1.79 \tag{2.4b}$$

$$\alpha = 0.192 \left(\frac{\sigma_{u,v}}{\sigma_{0.2,v}} \right) - 0.068 \tag{2.4c}$$

This model, which was adopted in American Iron and Steel Institute (2007), indicates that two factors affect corner yield strength $\sigma_{0.2,c}$, which are the ratio of ultimate strength ($\sigma_{u,v}$) over yield strength ($\sigma_{0.2,v}$) of virgin steel and the ratio of the internal root radius (r_i) over virgin steel thickness (t). Thereafter, Abdel-Rahman and Sivakumaran (1997) conducted 41 tensile coupon tests on cold formed steel of channel sections to

evaluate Karren's model. Their results reveal that that strength enhancements also occur in regions close to the corners but are not as substantial compared to those observed in the corner regions themselves. They observed that the experimentally obtained corner over flat yield strength ratio $\left(\frac{\sigma_{0.2,c}}{\sigma_{0.2,v}}\right)$ on average ranged from 49 to 74% of those determined by Karren's model. Based on that, their proposal was to continue using Karren's model but with adding a modification factor (0.6) to Equation (2.4a). Similarly, a modification to Equations 2.4b and 2.4c has been proposed by Gardner et al (2010) based on 40 corner tests results which extracted from rectangular and square hollow sections made of stainless steel. The revised values of B_c and α, as given by Equations 2.5a and 2.5b, offer more accurate predictions of corner yield strength than those predict by Karren's model for cold formed box sections when applied to cold-formed stainless steel sections.

$$B_c = 2.9 \left(\frac{\sigma_{u,v}}{\sigma_{0.2,v}}\right) - 0.752 \left(\frac{\sigma_{u,v}}{\sigma_{0.2,v}}\right)^2 - 1.09 \qquad (2.5a)$$

$$\alpha = 0.23 \left(\frac{\sigma_{u,v}}{\sigma_{0.2,v}}\right) - 0.041 \qquad (2.5b)$$

With regard to the yield strength of full section, American Iron and Steel Institute (AISI, 2016) provides an expression, which was originally proposed by Karren and Winter (1967), to determine the average yield strength $(\sigma_{0.2,a})$ for the entire section as given by Equation 2.6.

$$\sigma_{0.2,a} = C\sigma_{0.2,c} + (1 - C)\sigma_{0.2,f} \qquad (2.6)$$

where:

C is the ratio of corner area to total cross-sectional area.

$\sigma_{0.2,f}$ is yield strength of flat region.

EN 1993-1-3 (2006) provides a different expression, given by Equation 2.7, to determine $(\sigma_{0.2,a})$.

$$\sigma_{0.2,a} = \sigma_{0.2,v} + (\sigma_u - \sigma_{0.2,v})\frac{kNt^2}{A_g} \qquad (2.7)$$

where:

k is a numerical coefficient that depends on the type of forming, k=7 for roll forming and k=5 for other methods of forming

N is the number of $90°$ bends in the cross-section with an internal radius r_i ≤5t

A_g is the gross cross-sectional area

t is the design core thickness of the steel material before cold forming.

These expressions are intended to simplify the design of non-slender (i.e. class 3 or better) of cold-formed cross-sections by replacing the different nominal yield strengths observed in the corner and flat material regions with a single average value. The use of a full-section yield strength leads to a better approximation of observed structural behaviour and more favourable strength predictions for non-slender sections, however, given that the vast majority of cold-formed steel members is class 4, the scope of application is limited to very few cases.

2.1.4 Residual stresses

The fabrication of cold formed steel also introduces residual stresses which are the self-equilibrating stresses that exist in structural members in the absence of loading and are due to the fabrication procedure. In general, residual stresses are present in both hot-rolled and cold-formed sections, due to the differential rate of cooling and subsequent strength and stiffness increase in the various parts of a hot-rolled section and due to plastic deformation in a cold-formed respectively. Furthermore, residual stress might be present in the steel sheet used for the production of cold-formed sections due to the coiling, uncoiling and levelling process before applying the cold forming process. In the remainder, only residual stresses in cold-formed sections will be discussed.

Residual stresses may lead to premature yielding and because of that the stiffness decreases and likely the load carrying capacity deteriorates (Gardner and Cruise, 2009). A destructive method in laboratory is usually used to measure the residual stresses in cold formed steel. The sectioning method was utilised by Batista and Rodrigues (1992) to determine the longitudinal residual stresses distributions in channel sections manufactured by both cold roll forming and press-braking. They observed that residual stresses in press braking sections were smaller than those in roll forming sections. This shows that residual stresses magnitude is affected by the quantity of cold work. The longitudinal residual stresses in cold formed channel section were also measured by Weng and Pekoz (1990). Their findings indicate that magnitudes of residual stresses in the corner region were high compared to those in the flat portions. Moreover, the compressive residual stresses observed on the internal surface of the sections, whereas tensile residual stresses found on the outside

surface. Similar findings were reported in (Abdel-Rahman and Sivakumaran, 1997, Ma et al., 2015, Chen and Young, 2019).

Commonly residual stresses are considered to be a combination of two types, namely membrane residual stresses and bending residual stresses as shown in Figure 2.5 (Weng and Pekoz, 1990). Membrane residual stresses, which can be compressive or tensile, are distributed evenly throughout the whole section thickness. On the contrary, bending residual stresses, which have more significant impact on cold formed steel sections compared to the membrane ones, vary through the section thickness (Weng and Pekoz, 1990). The occurrence of membrane residual stresses is more common in cold-rolled members than press braked members and the effect of them is only high in the corner region of the sections.
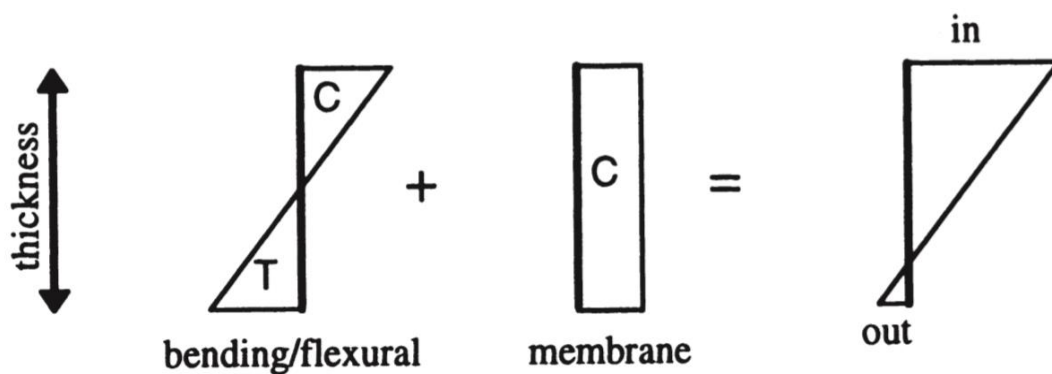
Figure 2.5 The bending and membrane components of residual stresses (Schafer and Peköz, 1998).

The bending residual stresses lead to an earlier loss of stiffness under applied load hence promoting buckling, whilst the corner strength enhancements increase the cross-sectional strength as the press-braked corners possess higher strength than the flat material of the section. Since the material coupons curved upon their extraction

from the section due to the release of bending residual stresses, the effect of the residual stresses is reflected in the obtained material properties, as the residual stresses are reintroduced as the coupons were straightened during the initial stages of tensile testing (Gardner and Cruise, 2009). Given that strength enhancements and residual stresses are caused by the same process, neither the strength enhancements of the corner regions nor the residual stresses have been explicitly modelled in this thesis.

2.2 Buckling of flexural members

The thin-walled nature of cold-formed steel purlins makes them prone to several types of instabilities, including local, distortional and lateral-torsional buckling and interactions thereof, which in most cases prevent cold-formed sections from reaching their elastic moment resistance. Each of these buckling modes is discussed hereafter.

2.2.1 Local buckling

Local buckling is defined as a buckling mode which involves flexural deformations and rotations but no translation of the nodal lines (junctions between elements) (Schafer and Ádány, 2005) as shown in Figure 2.6. The length over which local buckling occurs (i.e. half-wavelength) is relatively short, normally less than the largest cross-sectional dimension (Macdonald et al., 2008). Local buckling always occurs at the cross-sectional level and includes all constituent plated elements comprising a cross-section that are partly or fully in compression, since they are interconnected (Roberts and Jhita, 1983). However, some of international design standards and design methods do not account for the element interaction when considering local buckling of cross-

sections and assume that a cross-section behaves as its most slender element, thus ignoring the beneficial effect of stockier element supporting the more slender ones.
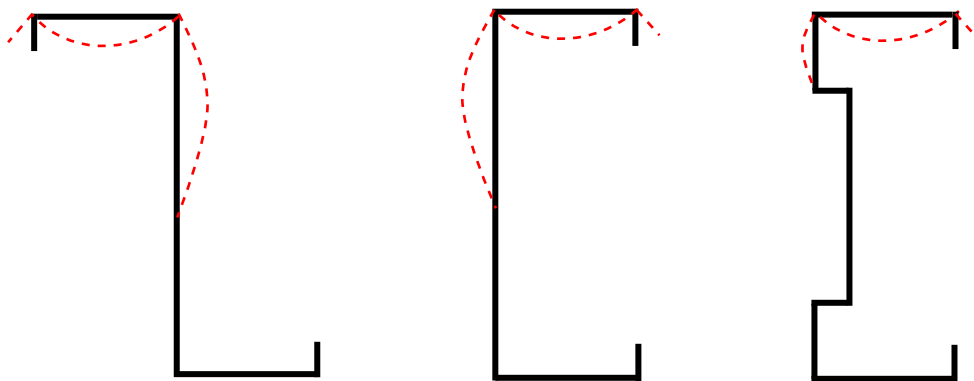
Figure 2.6 Local buckling for different cross-section.

Based on small deflection theory, Bryan (1890) developed a differential equation to determine the critical buckling stress of a plate. An expression for determining the elastic critical local buckling of a rectangular plate undergoing bending, shear and compression can be derived by solving Bryans' equation as given in Equation 2.8.

$$\sigma_{,cr} = k_f \cdot \frac{\pi^2 E}{12(1-v^2)(b/t)^2} \qquad (2.8)$$

Where:

k_f is the local buckling factor.

v is Poisson's ratio.

t is a plate thickness.

b is the width of plate.

The value of k_f depends on stress distribution and the boundary conditions, as well as the aspect ratio of the plate a/h (where a and h are the length and the depth of plate respectively). A comprehensive research has been carried out to determine the value of k_f. Gerard and Becker (1957) studied the relationship between the local buckling factor k_f and the aspect ratio under a given loading and boundary conditions and found that the value of k_f tends to be approximately constant for simply supported plates with increasing aspect ratios increases as shown in Figure 2.7. Timoshenko et al. (1961) proposed various k_f values for a long rectangular plate undergoing three types of stresses namely, shear, bending and compression stresses, and various boundary of conditions (free edge, simply supported and fixed) as reported in Table 2.1. Hancock (1978) utilised the finite strip Method (FSM) to provide k_f values for I- beams. Similarly, Seif and Schafer (2010) adopted a FSM-based software to derive empirical equation for k_f as a function of section geometry and loading condition.
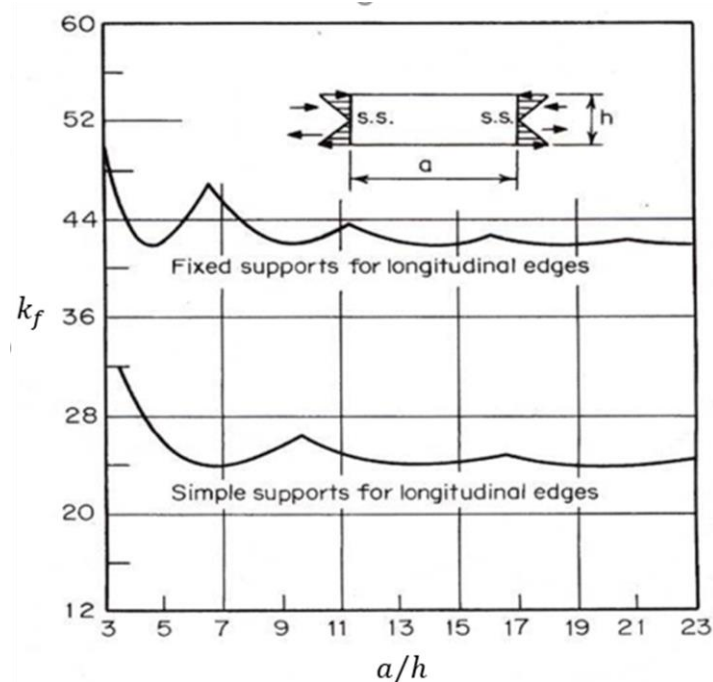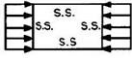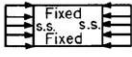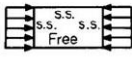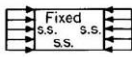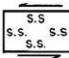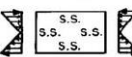
Figure 2.7 local buckling factor vs aspect ratio (Gerard and Becker, 1957).

Table 2.1 Local buckling factor for a long rectangular plate (Timoshenko and Gere 1961).

Case	Boundary condition	Type of stress	Value of k for long plate
(a)	s.s. / s.s. s.s / s.s	Compression	4.0
(b)	Fixed / s.s. s.s / Fixed	Compression	6.97
(c)	s.s. / s.s. s.s / Free	Compression	0.425
(d)	Fixed / s.s. s.s / Free	Compression	1.277
(e)	Fixed / s.s. s.s / s.s.	Compression	5.42
(f)	s.s / s.s. s.s / s.s.	Shear	5.34
(g)	Fixed / Fixed Fixed / Fixed	Shear	8.98
(h)	s.s. / s.s. s.s. / s.s.	Bending	23.9
(i)	Fixed / Fixed Fixed / Fixed	Bending	41.8

The occurrence of local buckling leads to stiffness loss (Bulson, 1970) but this does not mean that a member will collapse immediately or no longer able to carry more load. In fact, the member can bear additional loads after the initial local buckling stress reached as a consequence of redistribution of stress and membrane action (Yu et al., 2010). Bulson, 1970 found that a square plate subjected to compression will continue carrying loads even with about 40% reduction of the initial elastic stiffness regardless of whether the plate element is stiffened or not as shown in Figure 2.8. This phenomenon is called post-buckling behaviour. Studying the post buckling behaviour theoretically is very complex and normally needs a computer analysis to accomplish an accurate solution (Hancock, 1998). In 1932, von Karman (Von Kármán, 1932) investigated the post-buckling strength of plates and introduced an effective width method (EWM) to handle this problem. Based on experimental results, the EWM was later modified by Winter (1947, 1968). Nowadays, this method is still unitised in many

design standards including EN 1993-1-3 (2006). EWM will be discussed in detail in section 2.4.1.1.
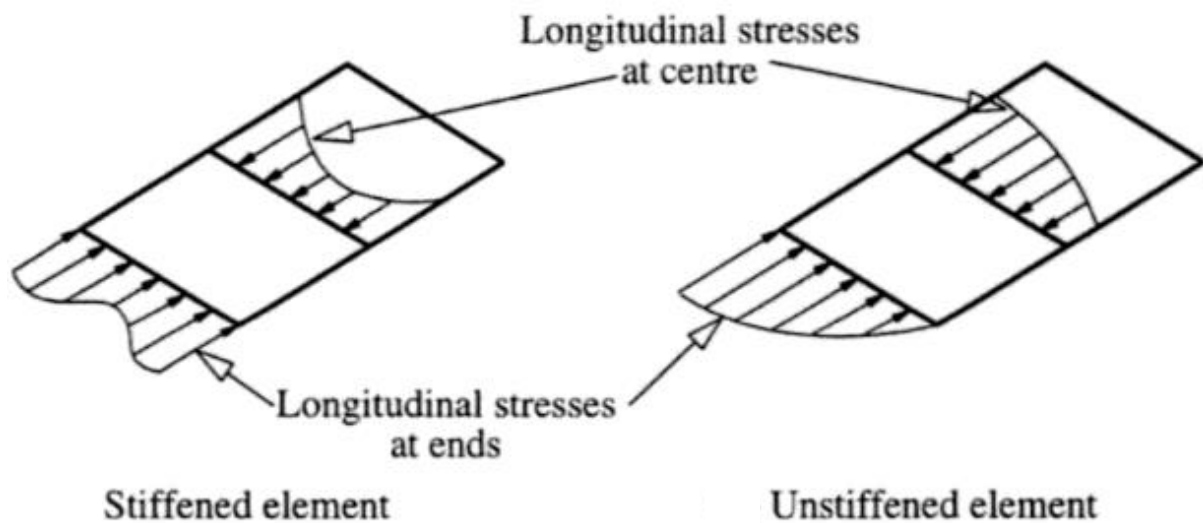
Figure 2.8 Post buckling behaviour of a square plate (Hancock, 1998).

2.2.2 Distortional buckling

A solution to enhance the behaviour of thin-walled member against local buckling is to incorporate edge and/or intermediate stiffeners into the cross-section, however, this leads to the occurrence of new buckling mode commonly termed "distortional buckling". Distortional buckling involves rotation and translation at the top flange-lip component of the member (Yu and Schafer, 2003) as shown in Figure 2.9. This phenomenon might be driven by web crippling as well (Yu and Schafer, 2003). Generally, the half-wavelength of distortional buckling is 3-6 times longer than that of the local buckling but shorter than that of lateral torsional buckling.
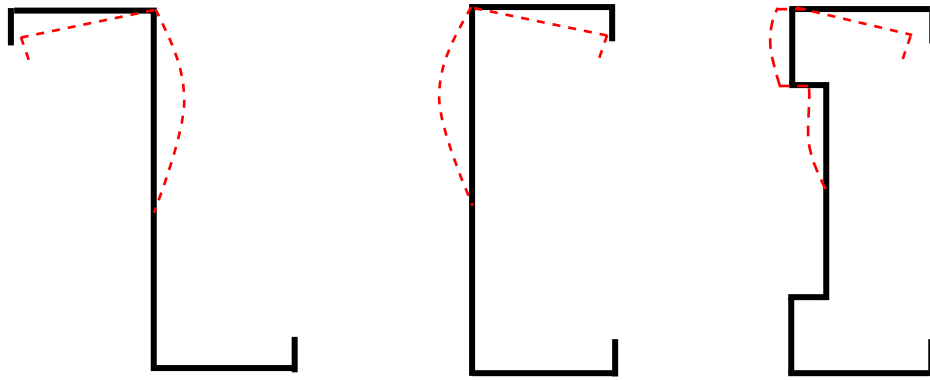
Figure 2.9 Distortional buckling for different cross-sections.

Between the 1940s and 1950s distortional buckling was first studied by several researches (Lundquist et al., 1943, Gallaher and Boughan, 1947, Van Der Maas, 1954), however, they found it very challenging to predict it analytically (Schafer, 2000). Dwight (1963) carried out experimental investigations on aluminium lipped channel sections and hat sections to study it. Later, Sharp (1966) proposed the first analytical method to approximate the distortional buckling, which he named at that time as "overall" buckling, and utilised Dwight's experiments for verifications. Desmond (1977), Desmond et al. (1981a) and Desmond et al. (1981b) studied the effect of edge and intermediate stiffeners on lipped channel columns and beams. They developed analytical equations by using effective width methods to predict the ultimate strengths of thin walled compression elements with edge and intermediate stiffeners. In their works, which established the basis for the AISI (1996) on edge stiffened elements, two different buckling modes have been reported namely local plate buckling and stiffener

buckling modes. The former refers to the distortional buckling mode. It has been found

that the critical stress for local buckling of a stiffened element is lower than that for

distortional buckling (Desmond, 1977), therefore, a single empirical solution has been

provided for the buckling coefficient of an edge stiffened element in local or distortional

buckling (Schafer, 2000). Accordingly, the treatment of distortional buckling was not

explicitly different from that of local buckling (Schafer, 2000). Thomasson (1978)

conducted tests on lipped channel sections and observed distortional buckling which

he named "local-torsional" buckling. He offered a solution to prevent distortional

buckling which is connecting one lip to another with tightly spaced braces (Schafer,

2000).

Hancock (1978) was the first who coined the term "distortional buckling" to distinguish

it from lateral-torsional and local buckling. Thereafter, Lau and Hancock (1987)

proposed an analytical model to determine the elastic distortional buckling stress of

channel column as shown in Figure 2.10a. The flexural-torsional buckling of a simple

flange is the basis of their model, in which the flange acts as an isolated column and

the effect of web is represented by applying the rotational spring stiffness k_Φ and

translational spring stiffness k_x at the web-flange junction. Since the effect of

translational spring stiffness on distortional buckling stress was found to be minimal,

Lau and Hancock (1987) suggested it could be neglected ($k_x = 0$). After a decade,

Hancock (1997) modified the previous model (Figure 2.10a) to predict the distortional

buckling stress of flexural members subjected to a constant bending moment. The revised model is shown in Figure 2.10b, in which rotational spring stiffness can be determined by considering the tension end of the web to be fixed. Both models were adopted in Australia standards (AS/NZS, 2005).

(a)   (b)
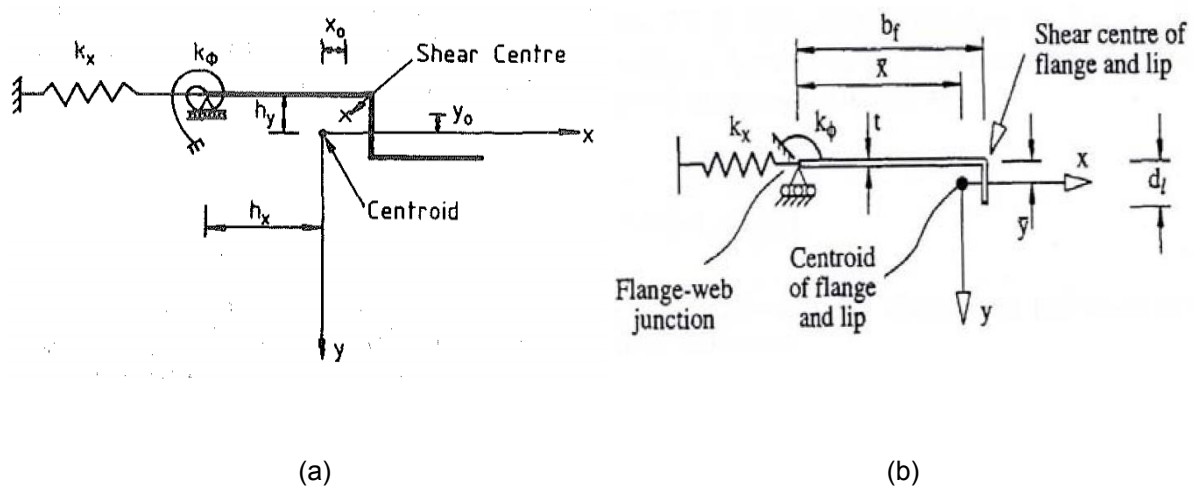
Figure 2.10 Analytical model for determining distortional buckling in (a) compression (Lau and Hancock, 1987) and (b) Bending (Hancock, 1997).

The Hancock's model was further examined and developed by Schafer and Peköz (1999) to introduce a new method for calculating the effective width of the web. The model of Schafer and Peköz (1999) was subsequently adopted by North American specifications for cold-formed steel (AISI, 2007).

Based on flexural buckling of stiffeners, an alternative analytical model for determining elastic distortional buckling of cold formed steel element with edge or intermediate stiffeners was provided by EN1993-1-3 (CEN, 2006a) as shown in Figure 2.11. In this

model the edge stiffener or intermediate stiffener is assumed to act as a compression element with continuous partial restraint, with a spring stiffness k which relies on boundary conditions and rotational stiffness of the adjacent elements. The spring stiffness should be obtained by applying a unit load u per member length at the centroid of the stiffener, as given by Equation 2.9. where δ is the deflection of the stiffener caused by the unit load. The model is described in detail in section 2.4.1.1

$$K = u/\delta \qquad (2.9)$$
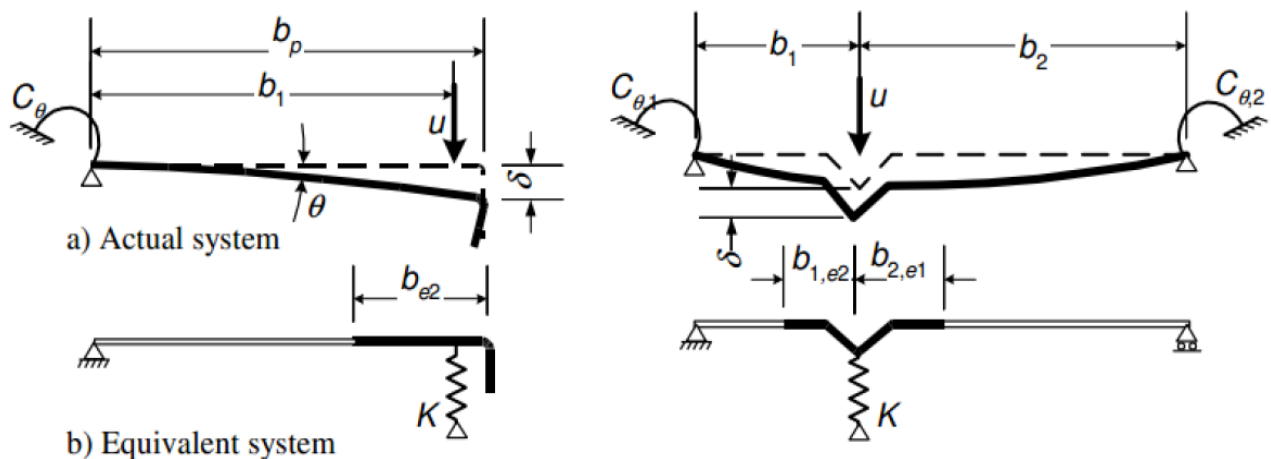
Figure 2.11 Determining distortional buckling according to EN1993-1-3 (CEN, 2006a).

2.2.3 lateral-torsional buckling

Lateral-torsional buckling is defined as the occurrence of translation and rotation of the whole section without distortion as shown in Figure 2.12 (Yu and Schafer, 2006). Generally, the half-wavelength of lateral-torsional buckling is the longest among the

three buckling modes (L, D and LTB), and is of the order of the length of the member. In the case of unrestrained beams, particularly with mono-symmetric open cross-sections (e.g. channel section) or point-symmetric open cross-sections (e.g. Zed section with equally flanges) which have a low torsional stiffness, lateral-torsional buckling may occur and impact the beam capacity (Dubina et al., 2012). However, as mentioned earlier in section 2.1 the possibility of lateral torsional buckling in a roof system, particularly under gravity load, is reduced and usually the purlins are considered to be fully restrained against lateral torsional buckling. Since LTB is not a failure mode relevant to this project, it will not be further discussed.
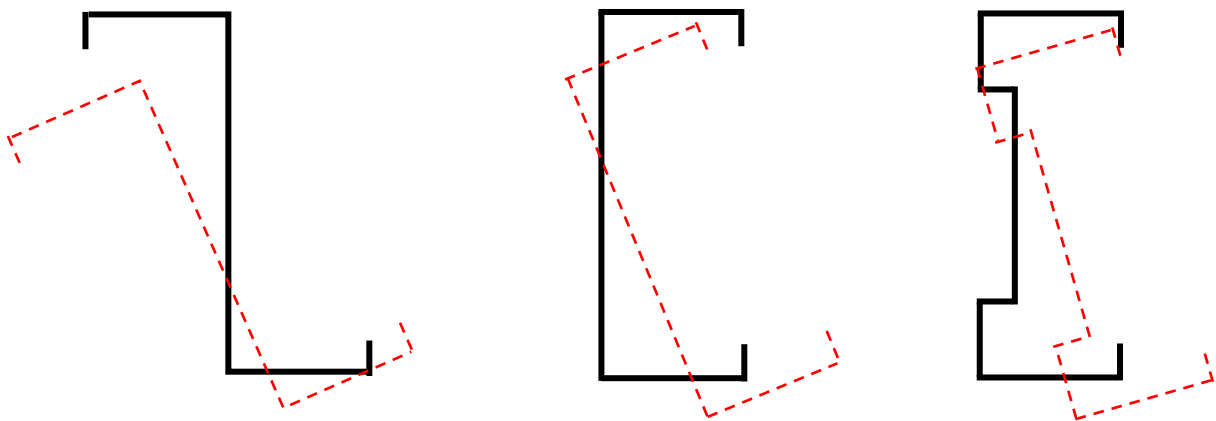
Figure 2.12 Lateral-torsional buckling for different cross-sections.

2.2.4 Buckling mode interaction

Cold-formed steel beams may fail in one of the buckling modes discussed before or any combination of these buckling could be critical depending on length, loading and geometry of the member (Martins et al., 2017b). The influence of mode interaction was studied by van der Neut in 1969, whose research became a point of reference for

studies on mode interaction (Becque, 2014). More researches have been conducted on the interaction between the local and overall buckling than that on the other coupled of interactions (e.g., L-D interaction) (Martins et al., 2017a). Therefore, most design standards consider only the interaction between overall and local buckling modes (Schafer, 2008).

The influence of local and distortional buckling interaction was first experimentally investigated by Kwon and Hancock (1992) on cold-formed lipped channel sections, with and without intermediate stiffeners in the web. They stated that all specimens failed owing to interaction between local and distortional buckling except three with intermediate stiffeners, which failed only due to distortional buckling and concluded that the simultaneous occurrence of local and distortional buckling did not unfavourably impact the member strength. About a decade later, Schafer (2002) concluded that the L-D interaction appears to be insignificant for columns, thus it was suggested to be ignored for design. However, Yang and Hancock (2004) preformed a compression test on high strength cold-formed steel channel and discovered a significant impact of the interaction between local and distortional buckling modes on the ultimate strength of the member. Thereafter, a significant amount of research has been undertaken to study the Local-Distortional interactive behaviour experimentally and numerically, mostly in columns.

Owing to the development of finite element method, studying the interaction modes has intensively increased in last two decades (Dubina and Ungureanu, 2013). Numerically, Dinis and Camotim (2010) studied the post-buckling behaviour of lipped channel beams undergoing uniform bending about their major axis and influenced by L-D interaction. In their study, two different cross-section geometries were chosen (i) to ensure that critical buckling moments for local and distortional buckling are equal,

hence maximising the effect of L-D interactions; and (ii) to ensure that local instability is triggered by either the web or the compression flange. Moreover, different initial imperfections magnitudes were considered to assess their effect on post-buckling behaviour of the selected beams. The results of Dinis and Camotim reveal that the pure local initial imperfections lead to the lowest post-buckling strength for beams the failure of which is triggered by their flanges, while when failure is triggered by the web the pure distortional initial imperfections are detrimental ones. Furthermore, the post-buckling behaviour of flange and web triggered beams are different qualitatively and quantitatively.

Haidarali and Nethercot (2011) developed two numerical models that simulate the response of laterally restrained cold-formed steel lipped Z-sections beams subjected to four-point bending to analyse the behaviour arising from the interaction of local and distortional buckling. Their two models, termed "complete" and "simplified" were verified against the tests conducted by Yu and Schafer (2006). Both models show a good agreement with the experimental results, however, employing the simplified modal would considerably reduce the computational time. The authors concluded that the models are capable of simulating cold formed steel beams affected by L-D interaction. Therefore, the simplified model was subsequently unitised to study the effect of the ratio of lip size to flange width and the inclination angle of the edge stiffener on z-section beam under four-point bending (Haidarali and Nethercot, 2012). It was found that the lip-flange interaction has a significant impact on the post-buckling strength and failure mode, and the inclination angel would not substantially affect the post-buckling strength if not exceeding 20°.

Anbarasu (2016) reported another numerical investigation on lipped channel beams under the uniform bending moment about the major axis. He stated that all beams analysed exhibited L-D interaction failure mode and the current DSM is unsafe for beams affected by L-D interaction, therefore, he introduced a new DSM strength curve for the treatment of L-D interactive failures. However, his proposed curve offers overly conservative and largely scattered predictions (Chen et al., 2020). Similarly, Martins et al. (2017a) conducted numerical investigations on three different cold-formed steel cross-sections namely, lipped channel section, zed-section and hat section, with two different support conditions and undergoing uniform bending. The current DSM design curves were once more found to be inadequate in predicting the ultimate strength for beam failed due to L-D interaction. Therefore, Martins et al. (2017a) proposed a modification to the current DSM to handle this coupling behaviour (L-D).

No experimental investigations with the aim of studying the effect of L-D interaction on cold-formed steel beams subjected bending were reported until 2019, when Ye et al. (2019) first reported tests on lipped channel beams affect by L-D interaction. Six back-to-back beams built up cold-formed steel lipped channel sections were subjected to four-point bending and laterally restrained at the load points. The occurrence of L-D interaction was observed in all tested beams. The experimental results were utilised to assess the accuracy of EN 1993-1-3 (CEN, 2006a), the current DSM (AISI, 2016) and the two modified DSM previously proposed by (Anbarasu, 2016, Martins et al., 2017a). The predictions of EN 1993-1-3 (CEN, 2006a) and the current DSM (AISI, 2016) were found to be in close agreement with test results, however, surprisingly, both modified DSM (Anbarasu, 2016, Martins et al., 2017a) were overly conservative. Opposite outcomes have been reported very recently (Chen et al., 2020) based on 20

tests on lipped channel beams subjected to four-point bending. Chen et al. (2020) stated that all beams failed by L-D interaction as planned and the modified DSM proposed by (Martins et al., 2017a) is more efficient and reliable than the current DSM (AISI, 2016), which appears to be unsafe since it provides overestimated strength predictions for beam failing by L-D interaction.

To date the effect of the interaction of local and distortional buckling has not been addressed in (AS/NZS, 2005; AISI, 2016), although various modifications to the current DSM have been proposed to address it, as dissused earlier. Hence, it can be concluded that further experimental and numerical investigations are still needed to better understand the L-D interactive buckling and to improve current design standards.

2.3 Web crippling

Purlins are primarily loaded by uniformly distributed loads; hence their geometry is optimized to resist local and distortional buckling, with little regard given to failure modes such as web crippling, which can occur in the presence of concentrated loads. However, due to their high strength-to-weight ratio, additional applications of cold-formed steel members have been pursued by cold-formed steel section manufacturers, thus necessitating the study of the response of highly optimised sections under loads they have not been optimised to resist.

A typical example of highly optimised cold-formed steel section geometry is the family of sigma section purlins which employs folding lines along their webs. The non-straight

geometry of their web is beneficial in terms of reducing the slenderness of the web plated element, however, it increases their susceptibility to web crippling in case the purlins are subjected to concentrated transverse loads and consequently, it reduces their overall moment resistance. Therefore, the structural behaviour of sigma sections when subjected to web crippling warrants further research to enable these sections to be used in applications involving concentrated point loads.

Web crippling is defined as the occurrence of localised failure at the points of concentrated load or supports where the stresses are localised as shown in Figure 2.13. Studying the various cross-sectional instabilities of cold-formed steel members theoretically is very complex as many factors are involved, such as the initial geometric imperfections of the plated elements, load eccentricities, effect of curved corner regions, material yielding (Yu et al., 2010). Therefore, the first web crippling investigations were mainly experimental.
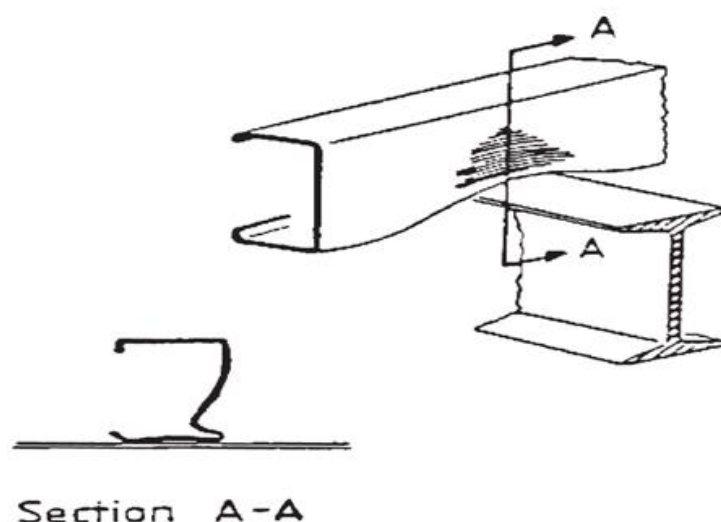
Figure 2.13 Web crippling (Rhodes and Nash, 1998).

The first article found in the literature was conducted in 1946 by (Winter and Pian, 1946) who experimentally investigated cold-formed steel I-beams and proposed four different loading conditions to study the effect of web crippling. These loading conditions are the end-one-flange (EOF), the interior-one-flange (IOF), the end-two-flange (ETF), and the interior two-flange (ITF) as illustrated in Figure 2.14. Based on their experimental work, empirical equations for web crippling design were recommended and adopted in the earlier version of the American standard AISI (American and Steel, 1969).

Following Winter and Pian (1946) investigation, many researches between the 1950s and 1990s conducted tests on different cross-sections such as Z-sections (Bhakta et al., 1992, Cain et al., 1995, Beshara and Schuster, 2000, Zetlin and Winter, 1952), channel sections (Hetrakul and Yu, 1978, Langan et al., 1994, Gerges and Schuster, 1998, Beshara and Schuster, 2000, Young and Hancock, 2001) I-sections (Hetrakul and Yu, 1978, Bhakta et al., 1992, Cain et al., 1995), Hat sections (Zetlin and Winter, 1952, Wing, 1981, Bhakta et al., 1992, Wu et al., 1997) and multi web sections (sheeting profiles) (Baehre, 1975, Wing, 1981, Yu, 1981, Studnicka, 1990, Bhakta et al., 1992, Wu et al., 1997). All these test results were gathered in (Beshara and Schuster, 2000) where fully empiric design provisions were derived for all four load cases and adopted in a more recent version of the AISI. To date, the current version of the AISI, which is the NAS S100-16 (AISI, 2016), still employs the four loading conditions proposed by Winter and Pian (1946). In Europe, the part of Eurocode dealing with cold-formed steel, the EN 1993-1-3 (CEN, 2006a), has adopted an equivalent system based on categories where category one corresponds to the EOF, ETF and ITF loading conditions and category two corresponds to the IOF loading

condition. Other design standards for cold-formed steel such as the New Zealand AS/NZS 4600:2018 (AS/NZS, 2005) are based on the same empiric principle. Although the design of rectangular and square hollow sections is not included in the above standards and codes, experimental research was also carried out before the 2000s (Zhao and Hancock, 1992, Zhao and Hancock, 1995).
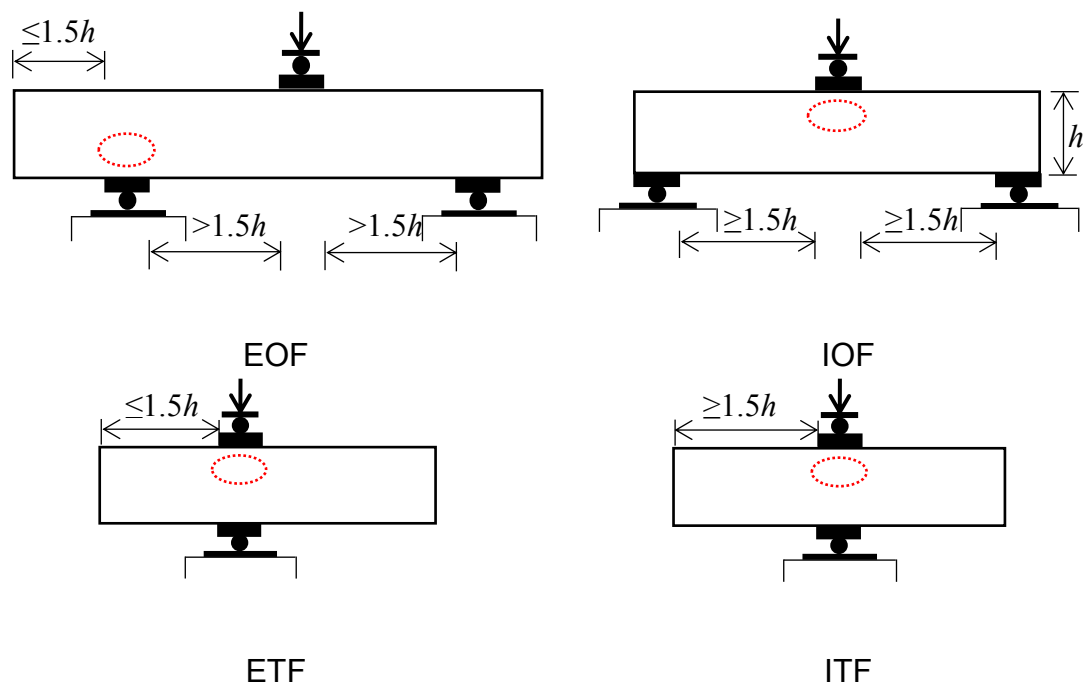
Figure 2.14 Web crippling loading conditions (a) EOF, (b) IOF, (c) ETF, (d) ITF.

Owing to the complex and physical nonlinearities associated with web crippling problems, it was not until the mid 1980s when the first numerical studies were reported by Santaputra et al. (1986) and (Sharp, 1989). Yet, web crippling simulations required long computational times that could result in unfeasible simulations (Sivakumaran, 1989, Bakker and Stark, 1994). This was overcome with the advancements in computing and numerical modelling software in the late 1990s and early 2000s making therefore possible to conduct the first parametric studies successfully (Hofmeyer et

al., 1999, Hofmeyer, 2005a, Ren et al., 2006, Kaitila, 2007). Since then, several research studies on cold-formed steel sections subjected to web crippling have been published with the aim to improve and extend the applicability of the empiric equations given in the above mentioned design standards with a focus on channel sections (Macdonald et al., 2011, Gunalan and Mahendran, 2015, Chen et al., 2015, Sundararajah et al., 2016, Janarthanan et al., 2019a, Janarthanan et al., 2019b), channel sections with perforations (Uzzaman et al., 2012b, Uzzaman et al., 2012a, Uzzaman et al., 2013, Yousefi et al., 2017b) as well as proprietary beams (Bock et al., 2019) and SupaCee sections (Sundararajah et al., 2018). With new emerging alloys available in construction and more advance methods of analysis, web crippling studies also exist on cold-formed high strength steel tubes (Li and Young, 2018), stainless steel (Gardner et al., 2006, Zhou and Young, 2007a, Zhou and Young, 2007b, Bock et al., 2015, Li and Young, 2017a, Yousefi et al., 2017a) as well as aluminium alloys (Zhou and Young, 2008, Young and Zhou, 2008, Alsanat et al., 2019) among others.

Although material and geometrical nonlinearities make predictive design equations based on first principles hard to obtain, efforts were made to derive analytical models for the treatment of web crippling (Bähr, 1978, Reinsch, 1983, Bakker and Stark, 1994, Vaessen, 1995, Young and Hancock, 2001, Hofmeyer et al., 2001, Hofmeyer et al., 2002, Hofmeyer, 2005b, Zhou and Young, 2006). These studies were based on traditional yield line mechanisms that combined with experimental observations were used to define web crippling collapse mechanisms and post buckling behaviour upon which to derive analytical equations. Web crippling mechanisms including the rolling mechanism, the yield arc mechanism and the yield eye mechanism for instance were identified for hat sections (Bakker and Stark, 1994) and subsequently used for multiple

web profiles (i.e. sheeting profiles) (Hofmeyer et al., 2001). Since late 2000s and beginning of 2010s the current trend in web crippling research is to shift from recalibrating empiric equations with test and numerical data to semi-empirical design approaches that combine numerical modelling and analytical methods (Hofmeyer and Bakker, 2008, Bakker et al., 2008). There is also research underway to develop finite strip analysis for web crippling to ultimately predict the web crippling strength as a function of the cross-sectional slenderness primarily for channel sections (Hancock and Pham, 2015, Natário et al., 2016, Nguyen et al., 2017c, Nguyen et al., 2017b).

Departing from empirical design approaches, a new slenderness-based design approach was proposed by Duarte and Silvestre (2013) for the web crippling design of channel sections. The underpinning concept of this approach is that, as with other buckling modes, web crippling resistance decreases with increasing slenderness, hence a buckling reduction factor χ can be explicitly determined as a function of section slenderness $\bar{\lambda}$, which is defined by Equation (2.10), where $R_{w,pl}$ is the plastic resistance load and $R_{w,cr}$ is the elastic critical buckling load. In this approach, the buckling reduction factor χ is determined by applying Equation (2.11), where R_w is the web crippling resistance. Equation (2.11) can be expressed as a function of the slenderness and two dimensionless coefficients A and B. It was shown in (Duarte and Silvestre, 2013) that the semi-empiric slenderness-based design method provides reasonable predictions for the web crippling resistance, however, the proposed equations are limited to a small range of web slendernesses, corner radii and geometries. Subsequently, Bock and Real (2014) adapted the slenderness-based design method to predict the web crippling resistance of cold-formed stainless steel hat sections and. In both articles, it was proved that a slenderness-based approach is

possible for web crippling design whilst achieving more accurate and reliable predictions than existing design standards.

$$\bar{\lambda} = \sqrt{\frac{R_{w,pl}}{R_{w,cr}}}$$

(2.10)

$$\chi = \frac{R_w}{R_{w,pl}} = \frac{A}{\bar{\lambda}^B}$$

(2.11)

2.4 Design standards and methods

2.4.1 Design Methods for flexural members failing in local and distortional buckling.

There are many design methods utilized for design cold-formed steel member but two of them are widely used and adopted in design standards. The more traditional design approach is the effective width method (EWM), whilst the more recent approach, is the direct strength method (DSM). Both these methods are assessed in Chapters 4 and 5, hence their original, theoretical underpinning, advantages and disadvantages as well as their exact formulation are further discussed herein.

The reduced effectiveness of slender cold-formed steel elements due to local buckling is traditionally accounted for using the effective width concept, originally developed by Von Kármán (1932) as later modified by Winter (1947). The effective width concept relies on the observation that upon local buckling of a slender plate, the compressive stresses are redistributed towards the supported parts of the plate with the central less

stiff parts attracting significantly lower stresses. Hence, parts of the constituent plate elements of a cross-section that have been classified as slender are assumed ineffective and only the effective parts are considered in the determination of the cross-sectional capacity.

This approach is adopted by all international design standards such as North American specifications for cold-formed steel (AISI, 2016) Australian design standards (AS/NZS, 2005) and Eurocode 3 (CEN, 2006a, CEN, 2006b). Although conceptually simple, the application of the effective width method necessitates the determination of effective cross-section properties, which is cumbersome particularly when it needs to be applied iteratively. Treating the cross-section as an assembly of constituent elements without accounting for their interaction has been shown to lead to inaccurate and inconsistent strength predictions for restrained Z and C sections in bending (Schafer and Trestain, 2002), as well as for more traditional cross-section shapes like RHS and I-sections in compression (Theofanous and Gardner, 2012). Furthermore, as discussed earlier, the adoption of edge stiffeners to improve resistance against local buckling (Desmond et al., 1981a) has led to the emergence of distortional buckling in cross-sections subjected to compression (Hancock, 1985) or bending (Yu and Schafer, 2006), an instability mode beyond the scope of the original effective width method. However, later EWM was extended to account for distortional buckling by Lau and Hancock (1987), Hancock (1997), Schafer and Peköz (1999) and (CEN, 2006a).

Given the increasing complexity of the geometry of modern cold-formed steel sections, the application of the effective width method, originally developed for cross-sections

of simple geometry, becomes awkward and its accuracy questionable. Schafer and Pekoz (1998) developed the Direct Strength Method (DSM) as an alternative design approach suitable for cross-sections of complex geometry and inherently able to deal with instability modes and their interactions at cross-sectional and member level.

The DSM is based on empirical equations relating member strength to its yield stress and its elastic critical buckling stress corresponding to all relevant buckling modes shapes. Key to the application of the DSM is the determination of the elastic critical buckling stress for all relevant buckling mode shapes, which is usually accomplished via the use of software such as the CUFSM (Li and Schafer, 2010). Since its original inception and its adoption by American (AISI, 2016) and Australian design standards (AS/NZS, 2005), the DSM has been further researched extended by several researchers to cover members subjected to bending and shear (Pham and Hancock, 2009), the effect of perforations (Moen and Schafer, 2006, Moen and Schafer, 2011) and the design of beam-columns (Schafer, 2019).
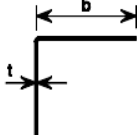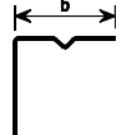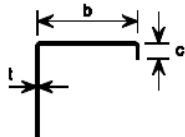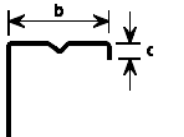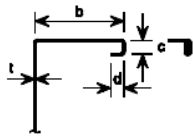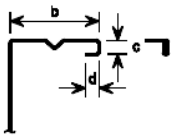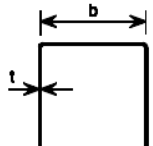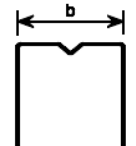
Both methods have been extensively used and have been calibrated on the basis of a large pool of experimental data. The EWM, although conceptually simple, is applied iteratively for members in bending and is therefore cumbersome to apply in practice. Furthermore, the lengthy calculations of the effective section properties are not warranted by its accuracy, which in cases of complex cross-section shapes is inferior to that of the DSM. On the other hand, the DSM is easy and fast to apply regardless of the cross-section shape and yields accurate strength predictions. A drawback of the DSM relates to its inability to account for the shift in neutral axis, which occurs when

non-doubly symmetric sections are subjected to compression and hence its failure to account for the associated second-order moments.

2.4.1.1 EWM (CEN, 2006a, CEN, 2006b)

The provisions for design given in (CEN, 2006a, CEN, 2006b) should be applied only to cross-sections that meet the following limits given in Table 2.2.

Table 2.2 Maximum width to thickness ratio (CEN, 2006b).

Element of cross-section		Maximum value
		$b/t \leq 50$
		$b/t \leq 60$ $c/t \leq 50$
		$b/t \leq 90$ $c/t \leq 60$ $d/t \leq 50$
		$b/t \leq 500$
		$45° \leq \phi \leq 90°$ $h/t \leq 500 \sin\phi$

a) For plane elements without edge stiffeners

The effective width of unstiffened element can be determined as following:

The effective width of compression elements b_{eff} is determined using Equation 2.12 and 2.13.

$$b_{eff} = \rho b \qquad (2.12)$$

$$\rho = \begin{cases} \text{a) for internal comperssion elements} \begin{cases} 1 & \overline{\lambda_p} \le 0.673 \\ \dfrac{\overline{\lambda_p}-0.0553(3+\omega)}{\overline{\lambda_p}^2} & \overline{\lambda_p} > 0.673 \end{cases} \\[4em] \text{b) for outstand comperssion elements} \begin{cases} 1 & \overline{\lambda_p} \le 0.748 \\ \dfrac{\overline{\lambda_p}-0.188}{\overline{\lambda_p}^2} & \overline{\lambda_p} > 0.748 \end{cases} \end{cases} \qquad (2.13)$$

Where ρ is the reduction factor, ω is the stress ratio, which can be determined from Table 2.3 for internal compression elements and Table 2.4 for outstand compression elements, $\overline{\lambda_p}$ is plate slenderness, $\overline{\lambda_p} = \dfrac{c/t}{28.4\varepsilon\sqrt{k_\sigma}}$, k_σ is the buckling factor corresponding to applied stress distribution and element support conditions, c/t is the width to thickness ratio and $\varepsilon = \sqrt{\dfrac{235}{f_y}}$ is a material parameter accounting for yield strength.

A refine using iteration might be applied to the effective section properties, where ψ is based on the effective cross-section of previous iterations.

Table 2.3 internal compression element (CEN, 2006b).
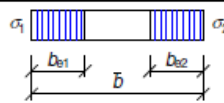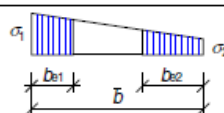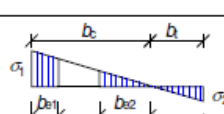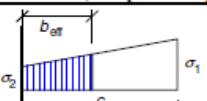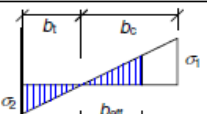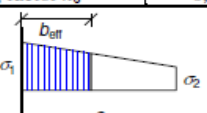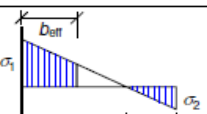
Stress distribution (compression positive)	Effective^p width b_{eff}
σ_1 [diagram b_{e1}, b_{e2}, $\bar{b}$] σ_2	$\underline{\psi = 1:}$ $b_{eff} = \rho\ \bar{b}$ $b_{e1} = 0{,}5\ b_{eff}$ $b_{e2} = 0{,}5\ b_{eff}$
σ_1 [diagram b_{e1}, b_{e2}, $\bar{b}$] σ_2	$\underline{1 > \psi \geq 0:}$ $b_{eff} = \rho\ \bar{b}$ $b_{e1} = \dfrac{2}{5-\psi} b_{eff}$ $b_{e2} = b_{eff} - b_{e1}$
[diagram b_c, b_t, σ_1, b_{e1}, b_{e2}, $\bar{b}$] σ_2	$\underline{\psi < 0:}$ $b_{eff} = \rho\ b_c = \rho\ \bar{b} / (1-\psi)$ $b_{e1} = 0{,}4\ b_{eff}$ $b_{e2} = 0{,}6\ b_{eff}$

$\psi = \sigma_2/\sigma_1$	1	$1 > \psi > 0$	0	$0 > \psi > -1$	-1	$-1 > \psi > -3$
Buckling factor k_σ	4,0	8,2 / (1,05 + ψ)	7,81	7,81 - 6,29ψ + 9,78ψ^2	23,9	5,98 (1 - ψ)^2

Table 2.4 outstand compression element (CEN, 2006b).

Stress distribution (compression positive)	Effective^p width b_{eff}
[diagram b_{eff}, σ_2, σ_1, c]	$\underline{1 > \psi \geq 0:}$ $b_{eff} = \rho\ c$
[diagram b_t, b_c, σ_1, σ_2, b_{eff}]	$\underline{\psi < 0:}$ $b_{eff} = \rho\ b_c = \rho\ c / (1-\psi)$

$\psi = \sigma_2/\sigma_1$	1	0	-1	$1 \geq \psi \geq -3$
Buckling factor k_σ	0,43	0,57	0,85	0,57 - 0,21ψ + 0,07ψ^2

Stress distribution (compression positive)	Effective^p width b_{eff}
[diagram b_{eff}, σ_1, σ_2, c]	$\underline{1 > \psi \geq 0:}$ $b_{eff} = \rho\ c$
[diagram b_{eff}, σ_1, σ_2, b_c, b_t]	$\underline{\psi < 0:}$ $b_{eff} = \rho\ b_c = \rho\ c / (1-\psi)$

$\psi = \sigma_2/\sigma_1$	1	$1 > \psi > 0$	0	$0 > \psi > -1$	-1
Buckling factor k_σ	0,43	0,578 / (ψ + 0,34)	1,70	1,7 - 5ψ + 17,1ψ^2	23,8

b) For plane elements with edge stiffeners

Three steps should be taken as follows:

1. An initial effective cross-section for the edge stiffener should be determined by utilising the effective widths calculated with assumptions that the stiffener provide full restraint and flange is doubly supported as shown in Figure 2.15. The effective width of flange can be determined form Equations 2.12 and 2.13a, while the lip can be determined by applying Equations 2.13b 2.14 and 2.15.

$$c_{eff} = \rho c \qquad\qquad (2.14)$$

$$k_\sigma = \begin{cases} 0.5 & c/b \le 0.35 \\ 0.5 + 0.83\sqrt[3]{(c/b - 0.35)^2} & 0.35 < c/b \le 0.6 \end{cases} \qquad (2.15)$$
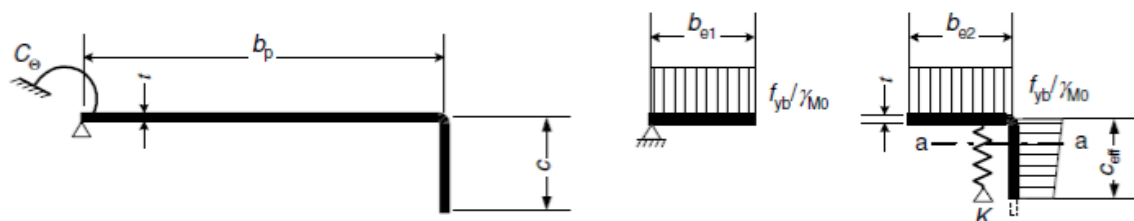
Figure 2.15 Determine the initial effective cross-section for stiffener (CEN, 2006a).

2. The reduction factor should be determined using the initial effective cross-section in order to account for distortional buckling as shown in Figure 2.16. The reduction factor can be calculated from Equation 2.16.

$$\chi_d = \begin{cases} 1 & \bar{\lambda}_d \leq 0.65 \\ 1.47 - 0.732\bar{\lambda}_d & 0.65 < \bar{\lambda}_d < 1.38 \\ \chi_d = \dfrac{0.66}{\bar{\lambda}_d} & \bar{\lambda}_d \geq 1.38 \end{cases} \qquad (2.16)$$

where $\bar{\lambda}_d = \sqrt{\dfrac{f_y}{\sigma_{cr,s}}}$, $\sigma_{cr,s}$ = the elastic critical stress of the stiffener.
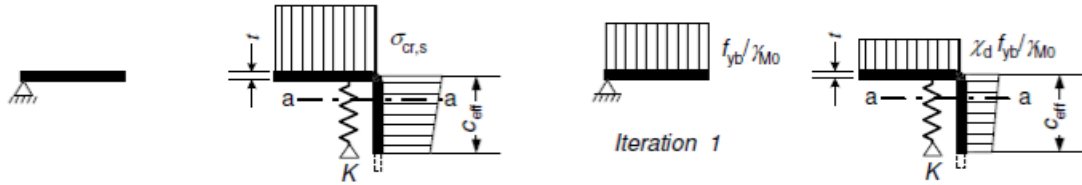
Figure 2.16 Determine the reduction factor for distortional buckling (CEN, 2006a).

3. Refine the reduction factor by repeating step 1 with the reduced strength $\left(\dfrac{\chi_d f_y}{\gamma_{M0}}\right)$. It should be noted that step 3 is optional.

Finally, a reduced stiffener cross-section is applied by considering a reduced thickness t_{red} if $\overline{\lambda_d} > 0.65$. At the end of this lengthy and iterative procedure including a and b an effective cross-section emerges the effective section modulus corresponding to a linear stress distribution W_{eff} of which is determined, and the moment resistance is obtained according to Equation 2.17:

$$M = \frac{W_{eff} f_y}{\gamma_{M0}} \qquad (2.17)$$

where W_{eff} is the effective section modulus, f_y is the material yield strength and γ_{M0} is the partial factor for cross-section resistance equal to 1.

2.4.1.2 DSM (AISI, 2016)

The prediction of DSM for local (M_{DSl}) and distortional buckling (M_{DSd}) of beams are given by the following equations:

For local Buckling

$$M_{DSl} = M_{ne} \qquad \text{If} \qquad \lambda_l \leq 0.776 \qquad (2.18a)$$

$$M_{DSl} = \left[1 - 0.15 \left(\frac{M_{crl}}{M_{ne}} \right)^{0.4} \right] \left(\frac{M_{crl}}{M_{ne}} \right)^{0.4} M_{ne} \qquad (2.18b)$$

$$\lambda_l = \sqrt{M_{ne}/M_{crl}} \qquad (2.18c)$$

For distortional buckling

$$M_{DSd} = M_y \qquad \text{If} \qquad \lambda_d \leq 0.673 \qquad (2.19a)$$

$$M_{DSd} = \left[1 - 0.22 \left(\frac{M_{crd}}{M_y} \right)^{0.5} \right] \left(\frac{M_{crd}}{M_y} \right)^{0.5} M_y \qquad (2.19b)$$

$$\lambda_d = \sqrt{M_y/M_{crd}} \qquad (2.19c)$$

where M_{ne} is the elastic critical buckling moments corresponding to lateral-torsional buckling, M_y is moment at first yield = $W_y f_y$; W_y = elastic section modulus, λ_d and λ_l are non-dimensional slenderness values for distortional and local buckling respectively. If the beams are assumed to be laterally restrained $M_{ne} = M_y$. The minimum value of M_y, M_{DSl} and M_{DSd} is the flexural strength of the section (M$_{DSM}$).

2.4.2 Current design standards for web crippling

The web crippling design rules provided in the current specifications such as the North American specifications for cold-formed steel (AISI, 2016) and Eurocode 3 Part 1-3 (CEN, 2006a) are summarized in this section.

2.4.2.1 North American specifications (AISI, 2016)

The north American specifications NAS S100-16 (AISI, 2016) specifies the unified empirical equation given in Equation 2.20 to determine web crippling capacity of different cross-sections for all four loading conditions. In Equation 2.20 h_w is the flat web height, θ is the angle between web and bearing surface, N is the bearing length, r is the internal radius and C, C_r, C_N and C_w are dimensionless coefficients related to the cross-section shape, internal radius, bearing length and web slenderness, respectively. NAS S100-16 (AISI, 2016) provides the values of dimensionless coefficients for only five different cross-sections namely, C-sections, Z-sections, hat sections, multi web sections and built up I-section (back-back C-sections). According

to NAS S100-16 (AISI, 2016), the applicability limits of Equation 2.20 are: $h_w/t \leq 200, N/t \leq 210, N/h_w \leq 2$ and $\theta = 90°$.

$$R_w = Ct^2 f_y sin\theta \left(1 - C_r\sqrt{\frac{r}{t}}\right)\left(1 + C_N\sqrt{\frac{N}{t}}\right)\left(1 - C_w\sqrt{\frac{h_w}{t}}\right) \qquad (2.20)$$

2.4.2.2 Eurocode 3 Part 1-3 (CEN, 2006a)

Unlike the north American specifications (AISI, 2016), Eurocode 3 Part 1-3 (CEN, 2006a) provides different equations for every loading condition.

For cross-sections with a single unstiffened web, the web crippling resistance can be determined as specified below and shown in Figure 2.17, if the cross-section meets three criteria, which are: $h_w/t \leq 200$, $r/t \leq 6$ and $45° \leq \theta \leq 90°$.

| (a) (EOF) | (b) (IOF) | (c) (ETF) | (d) (ITF) |
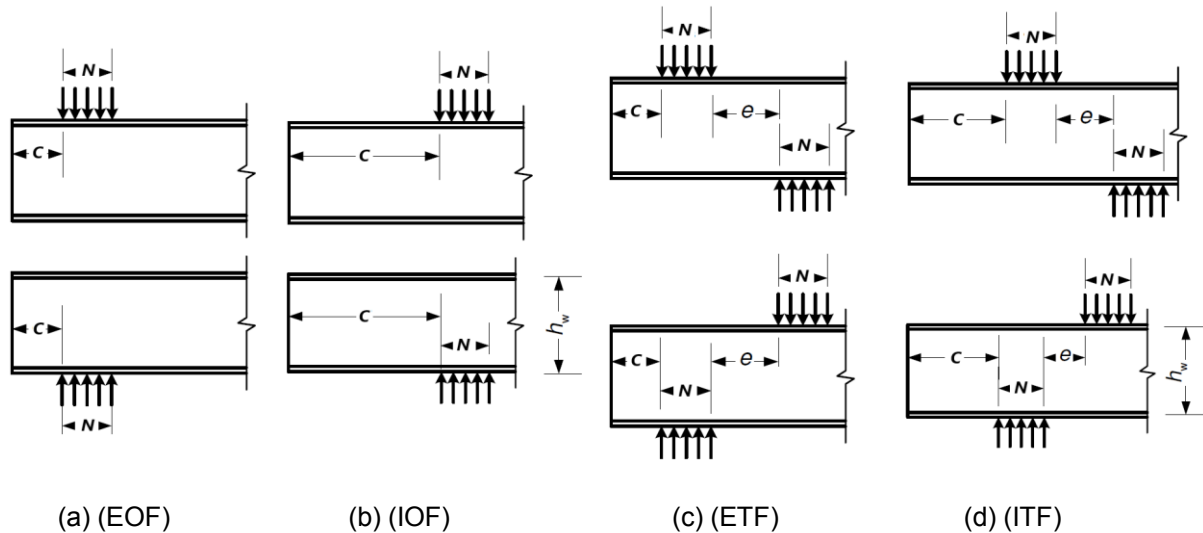
Figure 2.17 Four loading conditions (CEN, 2006a).

(a) End one flange ($c \leq 1.5\, h_w$)

For cross-section with stiffened flange

$$R_w = \frac{k_1 k_2 k_3 \left[9.04 - \frac{h_w/t}{60}\right]\left[1 + 0.01\frac{N}{t}\right]t^2 f_y}{\gamma_{M1}} \quad (2.21a)$$

For cross-section without stiffened flange
If $N/t \leq 60$:

$$R_w = \frac{k_1 k_2 k_3 \left[5.92 - \frac{h_w/t}{132}\right]\left[1 + 0.01\frac{N}{t}\right]t^2 f_y}{\gamma_{M1}} \quad (2.21b)$$

If $N/t > 60$:

$$R_w = \frac{k_1 k_2 k_3 \left[5.92 - \frac{h_w/t}{132}\right]\left[0.71 + 0.015\frac{N}{t}\right]t^2 f_y}{\gamma_{M1}} \quad (2.21c)$$

(b) Interior one flange ($c > 1.5\, h_w$)

If $N/t \leq 60$:

$$R_w = \frac{k_3 k_4 k_5 \left[14.7 - \frac{h_w/t}{49.5}\right]\left[1 + 0.007\frac{N}{t}\right]t^2 f_y}{\gamma_{M1}} \quad (2.22a)$$

If $N/t > 60$:

$$R_w = \frac{k_3 k_4 k_5 \left[14.7 - \frac{h_w/t}{49.5}\right]\left[0.75 + 0.011\frac{N}{t}\right]t^2 f_y}{\gamma_{M1}} \quad (2.22b)$$

(c) End two flanges ($c \leq 1.5\, h_w$)

$$R_w = \frac{k_1 k_2 k_3 \left[6.66 - \frac{h_w/t}{64}\right]\left[1 + 0.01\frac{N}{t}\right]t^2 f_y}{\gamma_{M1}} \quad (2.23)$$

(d) Interior two flanges ($c > 1.5\, h_w$)

$$R_w = \frac{k_3 k_4 k_5 \left[21 - \frac{h_w/t}{16.3}\right]\left[1 + 0.0013\frac{N}{t}\right]t^2 f_y}{\gamma_{M1}} \quad (2.24)$$

The coefficients k_1 to k_5 should be determined as follows:

$k_1 = 1.33 - 0.33k$

$k_2 = 1.15 - 0.15 \, r/t \ \text{ but } (0.5 \leq k_2 \leq 1)$

$k_3 = 0.7 - 0.3 \, (\theta/90)^2$

$k_4 = 1.22 - 0.22k$

$k_2 = 1.06 - 0.06 \, r/t \ \text{ but } (k_2 \leq 1)$

where $k = f_y/228$

For cross-sections with stiffened webs, the web crippling resistance can be determined by multiplying the equivalent value for a similar unstiffened web, obtained from previous Equations 2.21-2.24 as appropriate, by the factor $k_{a,s}$. However, the longitudinal web stiffeners should satisfy two conditions (i) $2 < \frac{e_{max}}{t} < 12$, (ii) web stiffeners should be "folded in such a way that the two folds in the web are on opposite sides of the system line of the web joining the points of intersection of the midline of the web with the midlines of the flanges" (CEN, 2006a) as shown in Figure 2.18. The factor $k_{a,s}$ is given by Equation 2.25.

$$k_{a,s} = 1.45 - 0.05 \, e_{max}/t \quad \text{but} \quad k_{a,s} \leq 0.95 + 35000 t^2 e_{min}/(b_d{}^2 s_p) \qquad \text{(2.25)}$$
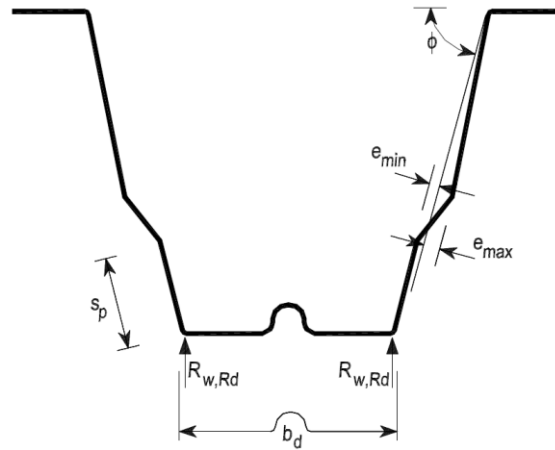
Figure 2.18 Stiffened web (CEN, 2006a).

where b_d is the width of loaded flange, S_p is inclined height of the plane web element closet to the loaded flange, and e_{max} and e_{min} are the larger and smaller eccentricity of the folds relative to system web line respectively.

The main differences between the design methods given in the two standards are:

(i) The Eurocode 3 approach can be applied to any cross-section that meets its criteria, whilst the NAS S100-16 approach can be applied only to five cross-section types mentioned earlier.

(ii) The Eurocode 3 approach is applicable to any cross-section with longitudinal web stiffeners that comply with its conditions, whilst the NAS S100-16 approach is not applicable to a cross-section with longitudinal web stiffeners.

(iii) The NAS S100-16 approach provides specifications for the five cross-sections with fastened and unfastened flange to the supports, whilst in the Eurocode 3 approach, no guidance is provided regarding flange conditions and the support.

2.5 Gap of knowledge

Based on the surveyed literature two main gaps in knowledge have been identified, which inform the research reported in Chapters 3-6. As stated in the literature, the lip (edge stiffener) has a significant impact on the flexural strength and observed failure modes. However, most purlin manufacturers provide standardised cross-sections, with significant variations in available section depth, thickness and flange width, but little if any variations in the lip size. To determine the optimal lip size to flange width ratio for various cross-section geometries of Z-sections, a series of tests on simply supported laterally restrained cold-formed steel lipped Z-sections purlins subjected to sagging moment was conducted and is reported in Chapter 3. As reported in Chapter 4, an advanced numerical model was developed and validated against the obtained test results, which allows parametric studies to be performed so that the effect of the lip size to flange width ratio on moment resistance can be further studied. Despite the considerable existing research on web crippling, no experimental or numerical data on the web crippling strength of cold-formed steel sigma sections subjected to concentrated transverse loads exist. Furthermore, there is no design standards provide design rules for the web crippling strength of sigma sections. Therefore, the first experimental and numerical investigation on cold-formed sigma sections subjected to interior one flange (IOF) loading is conducted as part of this project. Based on both experimental and numerical results a slenderness-based approach for web crippling design of sigma sections subjected to IOF loading is developed, as discussed in Chapter 5 and 6.

Chapter 3: Experimental tests on cold-formed steel Z sections in bending

3.1 Introduction

This chapter reports 8 experimental tests on simply supported purlins with lipped Z-sections under gravity loads. Despite several tests have been reported on sections of similar geometry have been reported, in most cases the adopted experimental configuration did not employ test details such as those used in practical applications but employed conventional 3- or 4-point bending arrangements (Ye et al., 2018). Although useful for determining the moment resistance, failure to account for the actual loading and support conditions in practice may results in unrealistic structural response. Furthermore, the development of a reliable FE model, like the one reported in Chapter 4, necessitates validation against experimental tests; in most cases published tests do not report experimental results in sufficient detail to allow such a model to be developed. Therefore, it was decided that experimental tests employing realistic load and support conditions had to be conducted as part of this project. The adopted test details are representative of the support conditions typically employed in practice with each specimen comprising two purlins connected to each other at regular intervals with angle struts used in lieu of anti-sag bars and profiled steel sheeting attached to the purlins' top flanges via self-drilling screws. The expected failure modes are distortional or local buckling or the interaction of both since the profiled sheeting would prevent the occurrence of lateral torsional buckling. The moment resistance predictions of Eurocode 3 and the Direct Strength Method (DSM) will be compared against the experimentally obtained moment resistances. The experimental results are utilized in chapter 4 where a numerical study on the optimization of the lip size to flange width ratio of Z sections is reported.

3.2 Experimental programme

A series of 8 tests was conducted on Z-section purlins to determine their flexural response. The employed test configuration was designed to simulate the behaviour of simply supported purlins under uniformly distributed loads (UDL) and avoid lateral torsional buckling. The aim of the tests was to obtain fundamental structural performance data to be used for the development and validation of a FE model capable of replicating numerically the experimentally observed structural response as reported in the following chapter.

3.2.1 Material properties

Tensile coupon tests on material coupons extracted from the mid-width of the flanges of cold-formed sections cut from the same member length as the tested specimens were conducted by the manufacturer. Three nominally identical coupons were extracted from each section. Some of the specimens displayed a well-defined yield plateau followed by strain-hardening similar to hot-rolled steels, whilst others exhibited a more rounded material response and an absence of a yield plateau, as shown in Figure3.1 where two typical stress-strain responses are depicted. This marked difference in material response of cold-formed steel has been previously observed by other researchers (Yu and Schafer, 2003) and increases the uncertainty regarding the appropriate material model to be used in parametric studies. No corner material properties have been obtained and their effect has not been explicitly considered given the small area of the corner regions and the high slenderness of the tested sections, which failed at loads below their elastic moment resistance. Table 3.1 reports the obtained material properties averaged out for each tested nominal thickness, where t

is the measured coupon thickness, E is the Young's modulus, f_y is the yield stress or 0.2% proof stress for coupons not exhibiting a yield plateau, $f_{1.0}$ is the proof stress at 1% plastic strain, f_u is the ultimate tensile stress and ε_f is the strain at fracture. It can be observed that specimens displaying a yield plateau had a higher ductility (i.e. ε_f) compared to the specimens that exhibited a rounded material response. It should be noted that the material yield strength determined from the tests is on average 3.6 % higher than the nominal one, which is 450 N/mm^2.
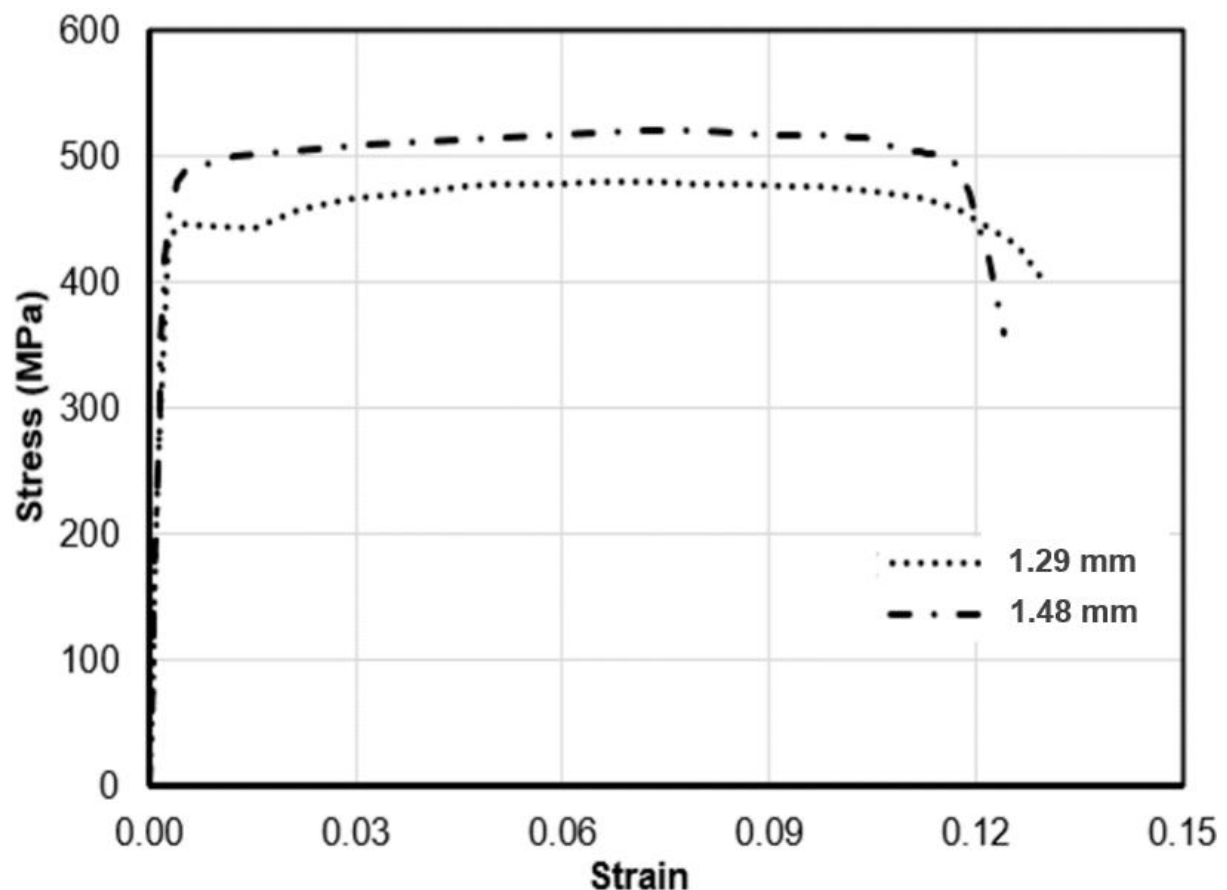
Figure 3.1 Typical stress-strain response of material coupons.

Table 3.1 Material properties from tensile coupon tests.

t (mm)	E (N/mm^2)	f$_y$ (N/mm^2)	f$_{1.0}$ (N/mm^2)	f$_u$ (N/mm^2)	ε$_f$ (%)	Material response
1.29	193000	447	470	480	14.7	Yield plateau
1.48	212000	482	484	521	14.5	rounded
1.76	205000	476	481	522	14.0	rounded
1.96	199000	457	460	532	25.0	yield plateau
2.47	206000	461	470	517	24.0	yield plateau

3.2.2 Specimen geometry

The geometry of the tested sections is representative of the Z-sections commonly used as secondary steelwork supporting roof sheeting in construction. The nominal outer depth h of the sections varies from 175 mm to 300 mm and the nominal thickness t varies from 1.30 mm to 3.00 mm thus encompassing a wide range of non-dimensional distortional and local slenderness. Prior to testing, measurements of the outer flange width b, outer overall depth h, lip depth d and thickness t were taken with a vernier caliper at each specimens' ends and mid-section. The measured section geometry for each section is reported in Table 3.2, where the average value of measurements of the internal root radius r$_i$ at the flange-web and flange-lip junctions respectively are also reported. It should be noted that average results for top and bottom flange and top and bottom lip are reported since no significant differences in the measured geometry of the top and bottom flange were observed. The section designation starts with the letter Z indicating a Z-section, followed by the nominal section depth and nominal section thickness. All symbols are defined in Figure 3.2. All section dimensions were within 3% percent of their nominal values except Z24630, the flange and lip lengths of which were measured to be 6% larger than the respective nominal values.
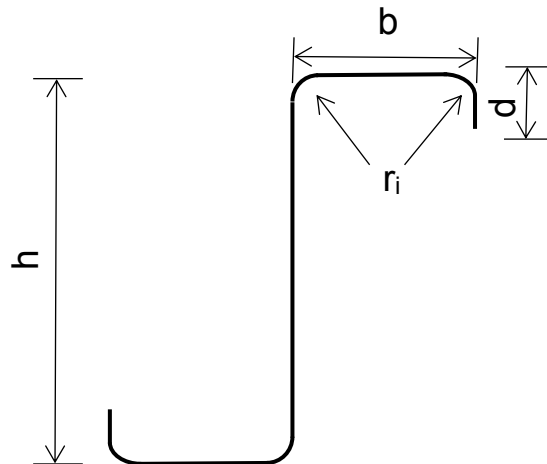
Figure 3.2 Cross-section geometry and symbols.

Table 3.2 Measured geometric dimensions of tested specimens.

Section	h (mm)	b (mm)	d (mm)	t (mm)	ri (mm)
Z14613	145.41	61.37	18.61	1.28	4.31
Z14620	145.68	63.35	17.34	1.96	4.07
Z17613	176.75	61.71	19.51	1.29	3.84
Z17625	176.13	63.7	20.95	2.47	4.05
Z20620	200.00	66.4	19.64	1.95	4.44
Z24615	239.75	65.3	20.47	1.48	3.80
Z24620	243.83	66.35	19.5	2.00	4.00
Z30718	300.25	75.1	16.95	1.76	4.05

3.2.3 Fabrication and setup

Each specimen consisted of two purlins connected at their top flange by profiled sheeting with the top flanges facing outwards and the bottom flanges facing inwards. The purlins comprising each specimen were attached to each other via angle struts

employed in practical applications as anti-sag bars, which were bolted through the specimen webs at 600 mm intervals prior to fixing the sheeting. The distance between the centrelines of the webs of the paired purlins was 250 mm for all specimens, whilst the overall width of the sheeting was 400 mm. In addition to facilitating load application, the sheeting also serves as a means to provide lateral and torsional support to the purlins hence reducing susceptibility to lateral torsional buckling under downward loading. The role of the anti-sag bars in the tests was to provide a connection between the two sections of each specimen at the points of load application and support, hence facilitating a torsional restrain and stabilising the specimen laterally. It should be noted that the connection details are identical to the ones used in practical applications.

Figure 3.3 shows a detail of an angle strut employed as anti-sag bar. It should also be mentioned that several purlins were visibly distorted prior to the assembly of the specimens. However, once fastened with the sheeting and the angle struts the global and distortional imperfections of the individual sections reduced significantly. It was observed that the twisting imperfections of the smaller sections were practically eliminated, and the resulting specimens appeared almost perfectly straight, whilst for the larger and stiffer sections, some of the initial twist remained. Given the large scatter typically exhibited by initial geometric imperfections and the effect of the assembly process on the imperfection patterns and magnitudes it was decided not to measure initial geometric imperfections in the experimental part of the project.

The sheeting was fixed with one self-drilling screw to the middle of the top flange of each purlin every 400 mm. The chosen spacing of 400 mm corresponds to one screw every second trough of the sheeting and lies at the high end of spacing employed in structural applications. An extra pair of fixings was adopted at the end sections over

the support, whilst two consecutive pieces of sheeting were screwed to one another at their overlapping crowns. Angle cleats are commonly used to support the purlins on the rafters and provide strengthening against web crippling. Four M12 bolts were used to attach the vertical leg of an angle cleat to the external part of the web of each of the purlins whilst the horizontal leg of the angle was bolted down on a thick plate resembling the flange of a rafter, as shown in Figure 3.4 where details of the attachment of the sheeting to the purlins can also be observed. In order to allow free rotation of the purlins at the supports, the plates on which the angle cleats were bolted were placed on top of cylindrical rollers. Similarly, cylindrical rollers were used between the spreader beams and the loading plates.

Figure 3.3 Typical angle strut and connection of strut and purlins.

Figure 3.4 End detail over the support.

3.2.4 Loading and instrumentation

The specimens were tested as simply supported beams with a clear span between the supports of 3000 mm, thus resulting in span-to-depth ratios ranging from 10 to 20.5. An extra 150 mm overhang beyond each support was provided to allow for the ends to move in as the loads are applied; hence the total length of each purlin was 3300 mm. Each specimen was subjected to 4 equal loads applied using two hydraulic actuators and two spreader beams. Each actuator applied a load onto the centre of the spreader beams, which were simply supported at fifth points (600 mm intervals) on the specimens as shown in Figure 3.5, where the setup is depicted schematically. This loading arrangement was employed to reflect the loading condition of a purlin subjected to a uniformly distributed load and to allow significant bending moments to be applied in the presence of low concentrated forces thus ensuring that failure occurs within the constant moment region. The loading points coincided with the location of the angle struts and were hence deemed torsionally restrained, whilst the chosen spacing of 600 mm between loading points results in a constant moment region with a length equal to 20% of the member length which is within the limits set by EN 1993-1-3 (CEN, 2006a).
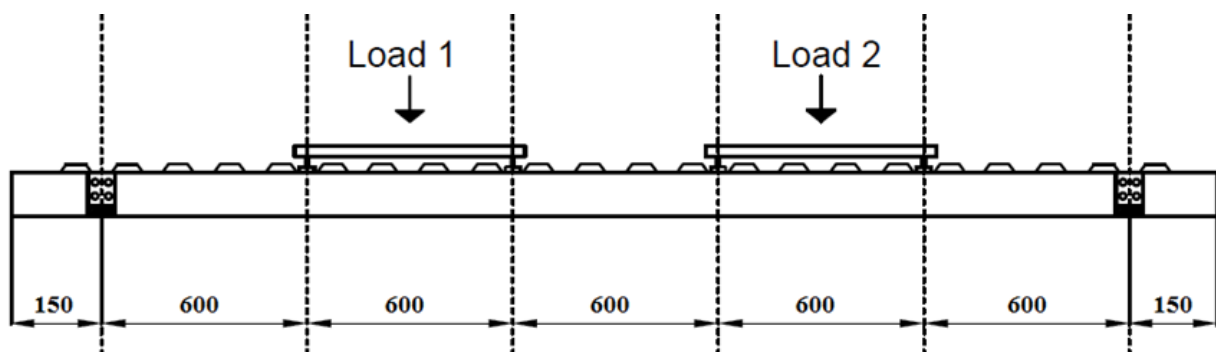
Figure 3.5 Overview of test setup (dimensions in mm).

Between the roller support of each spreader beam and the specimen a 20 mm thick and 80 mm wide plate used to facilitate a uniform distribution of stresses below the loading point and avoid local bearing failure. The hydraulic actuators were being lowered at a speed of 1.5 mm/min, thus replicating static loading conditions. In order to eliminate any effect of the loading speed, loading was paused for 2 minutes at 10 kN intervals in the beginning of the test and at 1 kN intervals close to the ultimate load. This is shown as distinct drops in the load-deflection curves in the following section where the results are reported. Three LVTDs under each purlin were used to monitor the vertical deflections at mid-span and adjacent load points. The LVDT readings were utilised to check whether the two purlins of each specimen exhibited identical load-deflection characteristics and the results are reported in the next section. Additional LVTDs were positioned on either side of the mid-span monitoring the horizontal deflections to determine whether any lateral torsional buckling was occurring during the testing. Moreover, the strain distribution and the resulting curvature of the tested sections were monitored and recorded at mid-span, where the maximum moment occurs. Two strain gauges were affixed on the web of each purlin of each specimen at a distance of 30 mm from the top and bottom flange respectively. Figure 3.6 depicts a specimen prior to the initiation of testing where the setup and employed instrumentation including the attached strain gauges and employed LVDTs can be clearly seen.

In past experimental and numerical studies (Haidarali and Nethercot, 2012, Pham and Hancock, 2009) the spacing of the screws attaching the sheeting to the purlins was shown to affect the failure load and failure mode of each specimen if several fixings are provided at closely spaced intervals. This effect is expected to be negligible for the

relatively large spacing adopted herein. Therefore, it is assumed that neither local nor distortional buckling of the tested sections is restrained by the attached sheeting and all specimens are free to develop both local and distortional buckling without the cladding providing any stiffness that is likely to suppress these buckling modes. This was verified by the observed failure modes which were not seen to be affected by the location of the fixings as will be discussed subsequently.

Figure 3.6 Experimental setup prior to testing and employed instrumentation.

3.3 Results and discussion

3.3.1 Moment resistance and failure modes

Table 3.3 reports key experimental results including the ultimate moment M_u and the observed failure mode. The ultimate moment is determined based on the recorded maximum applied loads, assuming that they are equally distributed between the paired purlins. The elastic moment resistance M_{el}, as determined with measured geometric and material properties, the M_u/M_{el} ratio and the elastic critical buckling moments corresponding to local and distortional buckling, $M_{cr,l}$ and $M_{cr,d}$ respectively, as

determined with the aid of the CUFSM software (Li and Schafer, 2010), are also reported to facilitate the discussion of the results in section 3.4. The letters "L" and "D" and "WC" refer to local buckling, distortional buckling and web crippling respectively and correspond to the observed failure modes at or shortly after the attainment of the failure load. In most cases failure occurred at moments below the elastic moment resistance of the cross-section, with only one section reaching or exceeding its elastic moment resistance. For all tests reported herein failure occurred in the constant moment region, whilst, where web crippling is indicated as a failure mode, this relates to the observed localised plastic deformation at the loading point which occurred after the maximum load was attained and is not believed to have triggered failure.

Table 3.3 Key experimental results and observed failure modes.

Section	M_u (kNm)	Elastic stiffness (N/m)	M_{el} (kNm)	M_u/M_{el}	$M_{cr,l}$ (kNm)	$M_{cr,d}$ (kNm)	Observed failure mode
Z14613	5.94	963251	7.15	0.83	6.3	6.19	D/L interaction
Z14620	11.54	1564029	11.63	0.99	23.21	14.46	D
Z17613	7.03	1694456	9.59	0.73	6.53	7.50	D/L interaction
Z17625	19.77	2363137	18.59	1.06	48.74	32.44	Yielding followed by D/L interaction
Z20620	15.62	3046389	18.55	0.84	23.22	19.73	D followed by WC
Z24615	11.55	3067543	18.76	0.62	9.78	13.16	D/L interaction
Z24620	20.33	4359471	25.27	0.80	22.96	23.20	D
Z30718	19.13	5788736	31.96	0.60	14.76	16.8	D followed by WC

Figures 3.7 - 3.14 show the failure modes of the tested specimens as captured at, or shortly after the attainment of the failure load. During testing, specimens Z14620 and Z24620 displayed pronounced deformations consistent with distortional buckling in the

opening mode within the constant bending moment region (Figures 3.8 and 3.13) as the load was approaching and shortly after the attainment of the ultimate load. Specimens Z14613, Z17613, Z17625 and Z24615 exhibited a similar response, with the difference being that the distortional buckling mode interacted with local buckling of the compressed lip of the sections, as evidenced in Figures 3.7, 3.9, 3.10 and 3.12, whereupon failure occurred. Specimens Z20620 and Z30718 failed by distortional buckling weakly interacting with local buckling of the flange, closely followed by web crippling close to the loading points. It should be noted that the web crippling deformations (i.e. localization of failure under one of the central loading platens as shown in Figures 3.11 and 3.14) occurred after the ultimate load was attained; hence it is believed that web crippling did not affect the moment resistance. Furthermore, specimen Z17625 experienced distortional buckling and localised buckling of the lip after the attainment of its elastic moment resistance.

Overall, the observed failure modes accord well with the elastic critical buckling moments reported in Table 3.3. As expected, due to the strongly stable post buckling response associated with local buckling compared to distortional buckling, in cases where the $M_{cr,l}$ is significantly larger than $M_{cr,d}$ as is the case for Z14620, distortional buckling is the observed failure mode without any evidence of local buckling. In cases where the elastic critical buckling moments for local and distortional buckling are closer to each other and when the critical local buckling moment is smaller than the critical distortional buckling moment ($M_{cr,l} < M_{cr,d}$), distortional buckling of the compressed flange occurs followed by localisation of plastic deformations in the compressed lip, whereupon a marked drop in strength occurs.

Figure 3.7 Failure mode of Z14613 - interaction of distortional buckling with local buckling of the lip at mid-span.
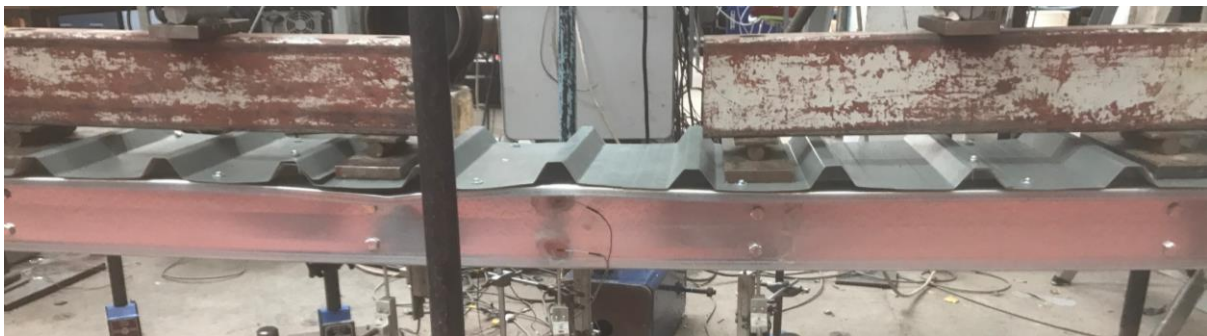
Figure 3.8 Failure mode of Z14620 - distortional buckling.
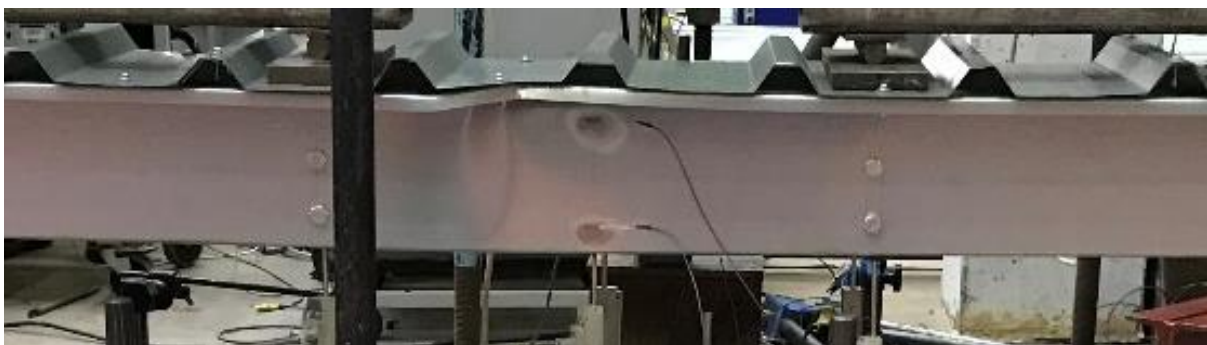
Figure 3.9 Failure mode of Z17613- distortional buckling and interaction with local buckling of lip.

Figure 3.10 Failure mode of Z17625 - distortional buckling and interaction with local buckling of lip following material yielding.

Figure 3.11 Failure mode of Z20620 - distortional buckling and web crippling after the peak load.
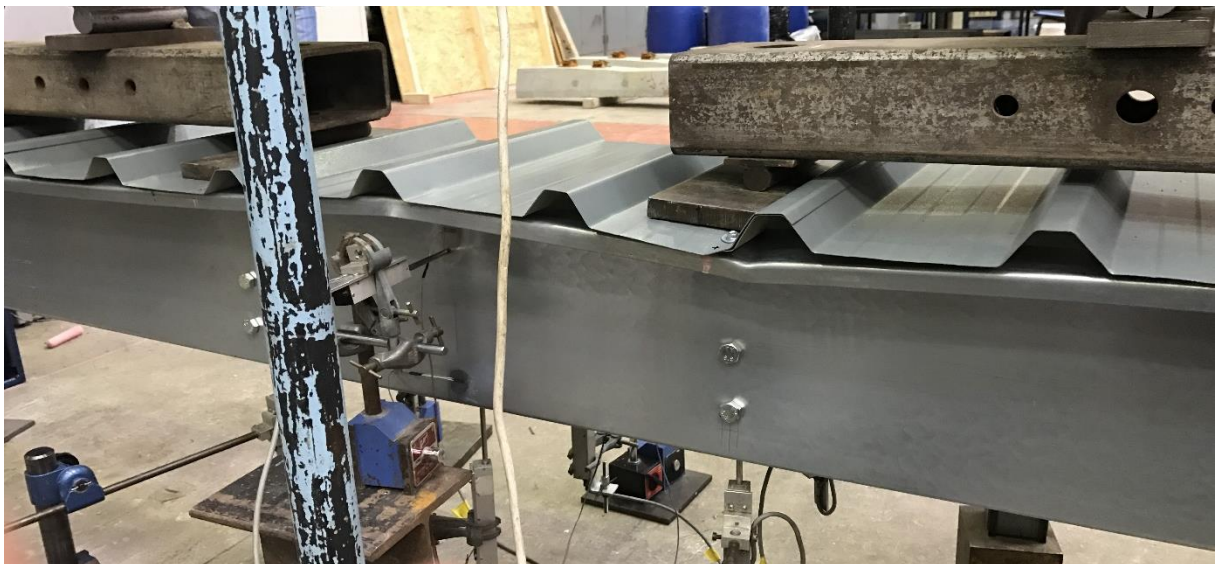
Figure 3.12 Failure mode of Z24615 - distortional buckling and interaction with local buckling of lip.

Figure 3.13 Failure mode of Z24620 - distortional buckling.
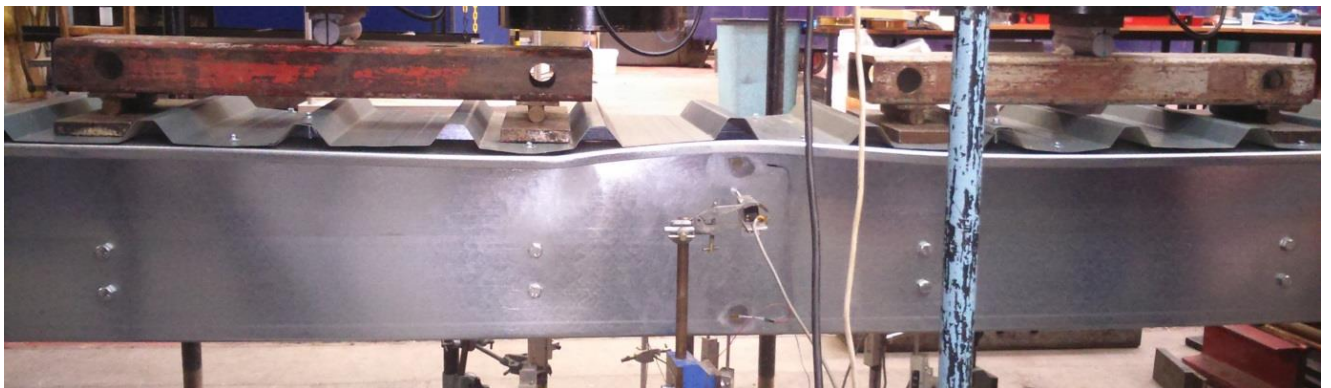
Figure 3.14 Failure mode of Z30718 - distortional buckling and localization of failure at left loading point (i.e. web crippling) after the peak load.

3.3.2 Load – deformation response

The total applied load and mid-span deflections of the twin purlins comprising each specimen have been utilized to obtain the overall load-deformation response. Figures 3.15 a) and b) depict the load-deformation response of specimens Z17613 and Z17625 respectively. Both twin purlins comprising each specimen can be seen to

behave very similarly in the initial part of the loading, as their respective curves are almost identical to one another up to failure, whereupon the response diverges. It can be clearly seen that the more slender section Z17613 exhibits an almost perfectly linear response with minimal loss of stiffness prior to failure, which occurs due to interaction between local and distortional buckling. The stockier section Z17625, which fails at a load 6% higher than the load corresponding to its elastic moment resistance, displays a gradual loss of stiffness, as the partial plasticisation of the cross-section causes the curve to exhibit a small plateau when approaching the ultimate load. Both specimens Z14613 and Z14620 behave in a similar way to Z17613 as shown in Figure 3.16.
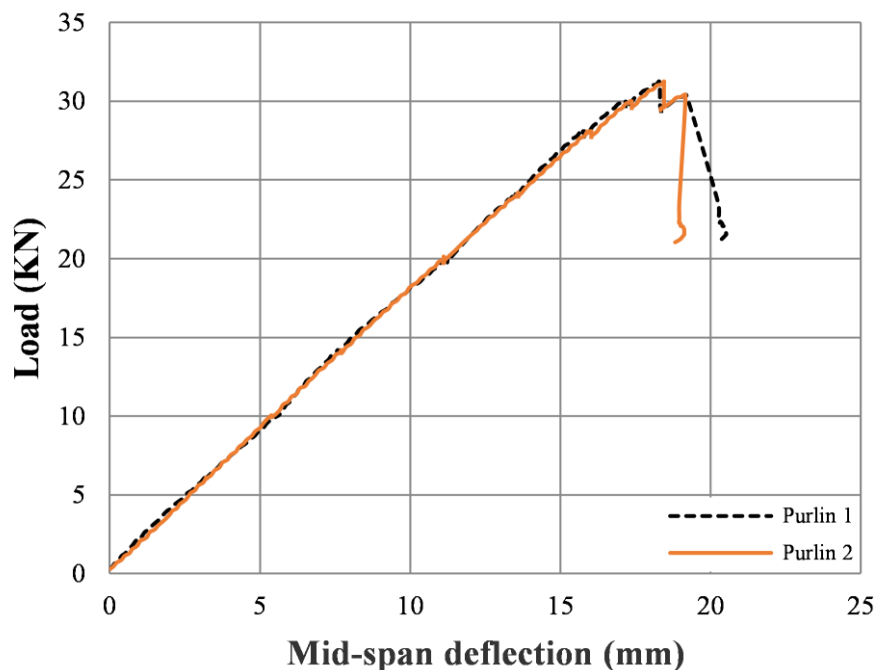
a) Z17613
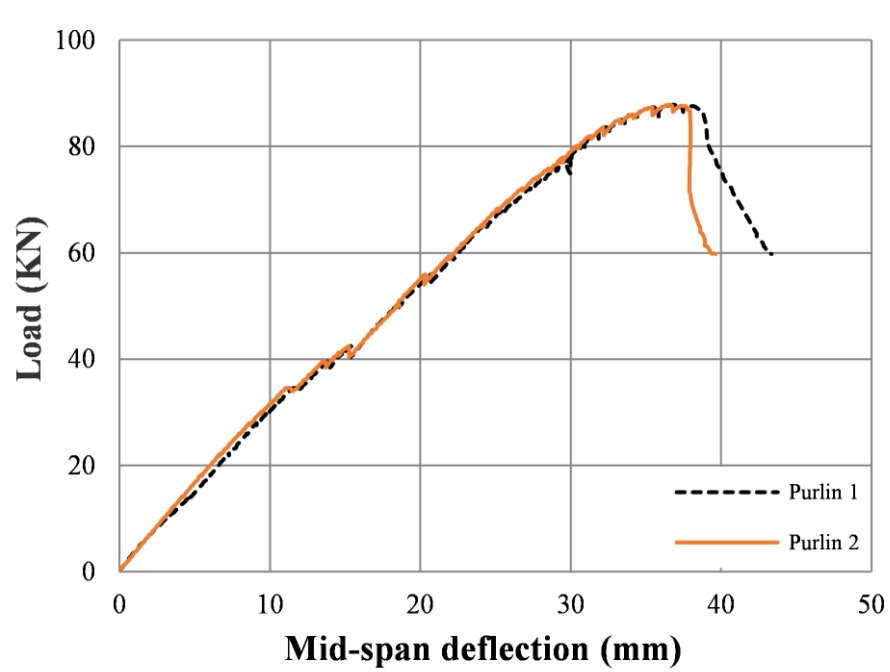
b) Z17625

Figure 3.15 Load - mid-span deflection response of specimens Z17613 and Z17625.
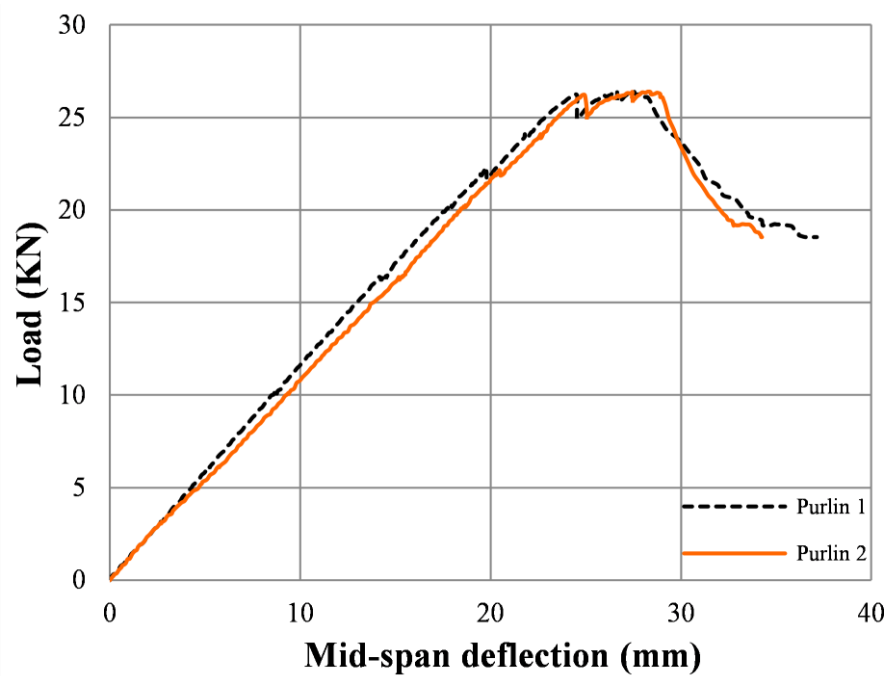
a) Z14613
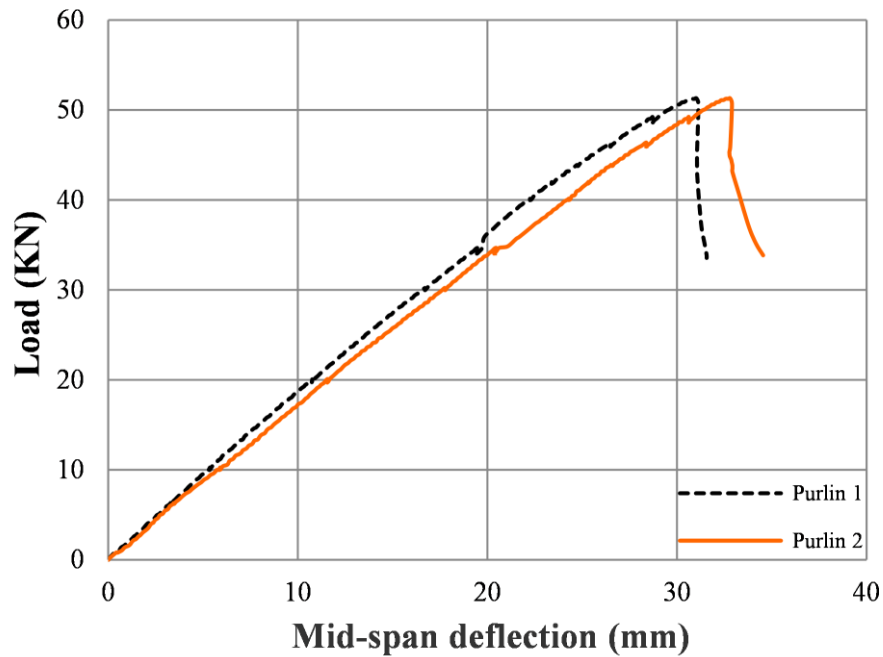
b) Z14620

Figure 3.16 Load - mid-span deflection response of specimens Z14613 and Z14620.

Figures 3.17 a) and b) show the load-deformation response of specimens Z24615 and Z24620 respectively. Specimen Z24615, which failed due to interaction between distortional and local buckling, displays a very similar response to that of purlin Z17613, with the twin purlins of the specimen demonstrating identical load-deflection response until the ultimate load is reached. Specimen Z24620, the failure of which involved distortional buckling shows a diverging response between the two purlins, arguably due to the pronounced initial twist imperfection of the purlins which was not eliminated when the specimen was assembled as was the case for the smaller and thinner sections.
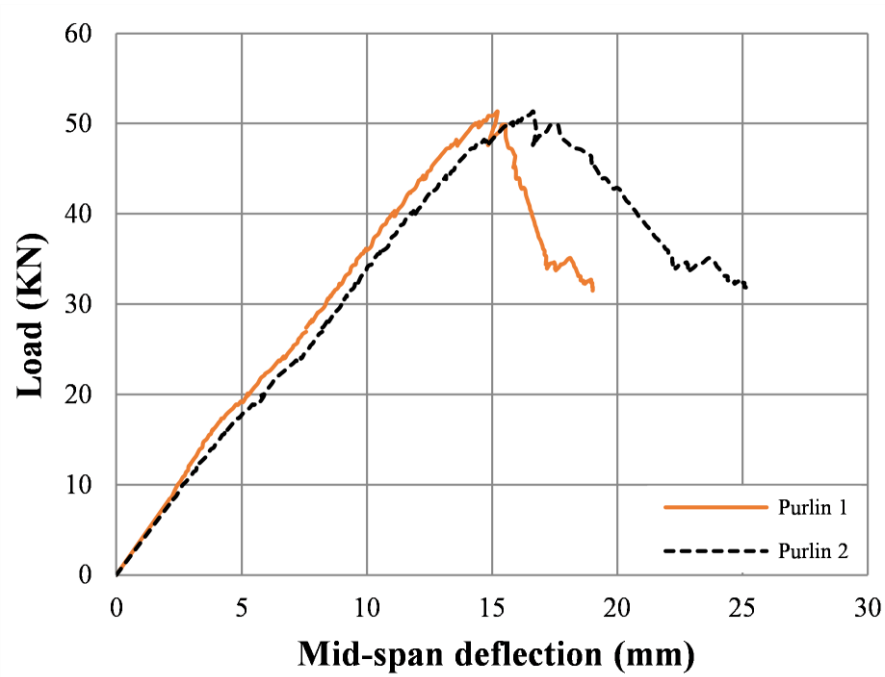
a) Z24615
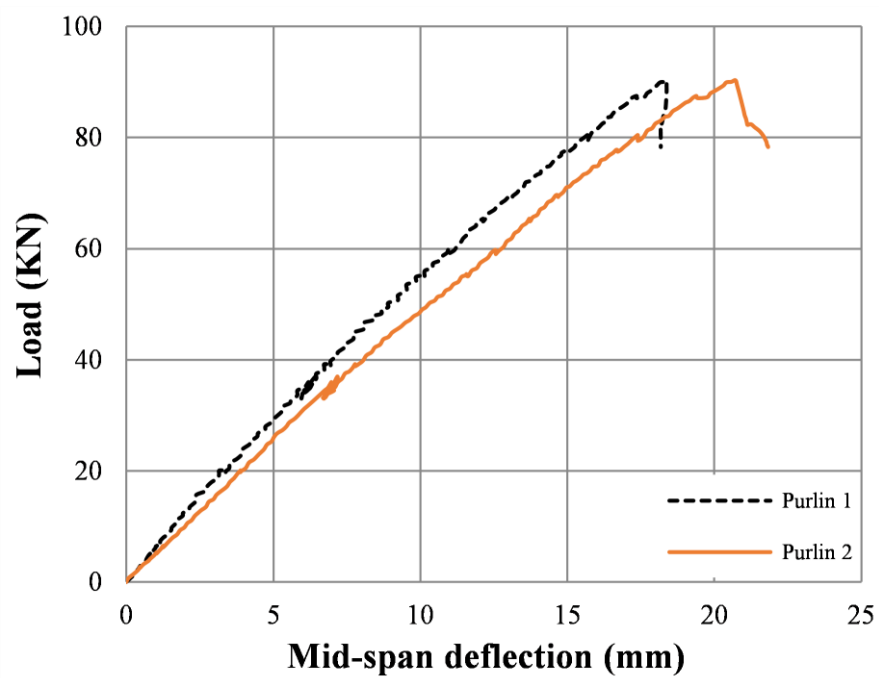
b) Z24620

Figure 3.17 Load - mid-span deflection response of specimens Z24615 and Z24620.

Figures 3.18 a) and b) depict the load-deformation response of specimens Z20620 and Z30718 respectively. Despite both specimens failed due to distortional buckling and followed by web crippling after the ultimate load was achieved, they show different load-deformation responses. Specimen Z20620 displays identical response for both purlins, whilst the twin purlins comprising Z30718 are seen to exhibit different stiffness in terms of the recorded load-vertical deflection response at the onset of loading. This is attributed to the pronounced initial twist imperfection of the purlins, which vanished with under increasing load.
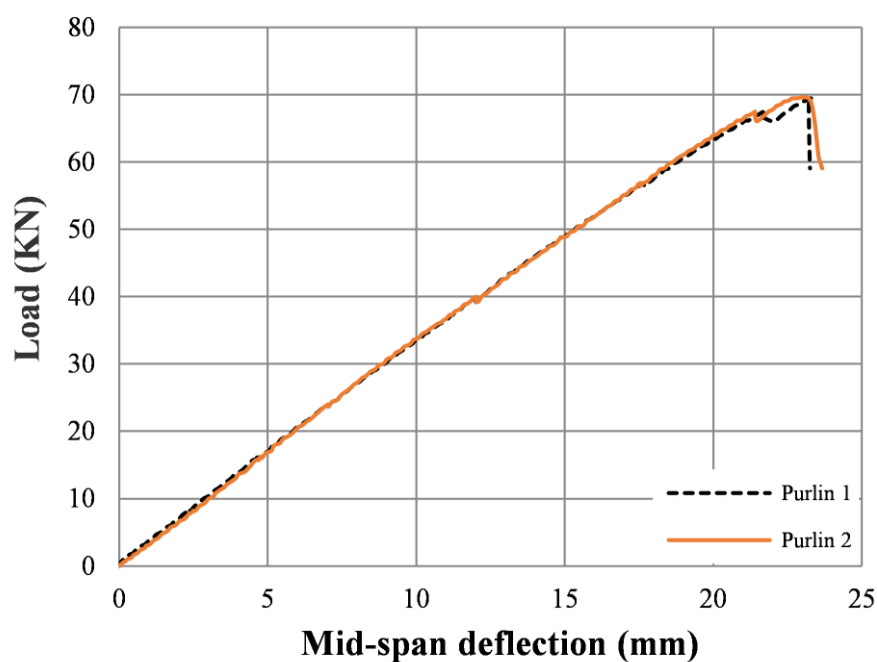
a) Z20620
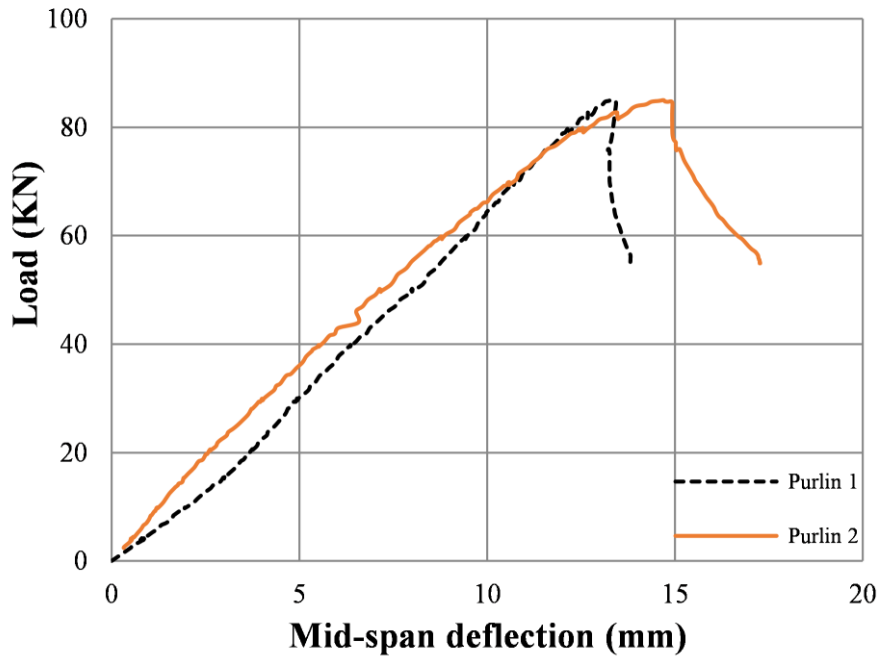
b) Z30718

Figure 3.18 Load - mid-span deflection response of specimens Z20620 and Z30718.

Examining the evolution of strains with increasing load offers significant insight on the structural response of the tested specimens. In Figure 3.19 the recorded strains on the web of each purlin are plotted against the applied moment at mid-span for specimen Z17613. To facilitate the discussion, the elastic critical buckling moments for local and distortional buckling $M_{cr,l}$ and $M_{cr,d}$, reported in Table 3.3, are also depicted as a horizontal dotted line and a horizontal solid line respectively. As expected, for both purlins, the strain gauges attached 30 mm below the top flange, denoted as "top", yield negative strain readings, whilst the strain gauges denoted as "bottom", which were affixed on the web at 30 mm above the bottom flange give positive readings. Due to the symmetric arrangement of the twin purlins of each specimen, the strain readings are almost identical for both purlins throughout the applied loading regime even beyond the attainment of the ultimate load. The obtained moment-strain response is

initially linear for both the "top" and "bottom" strain gauges with the respective readings of the "top" strain gauges being a mirror image of those of the "bottom" strain gauges. The recorded tensile strains remain linear and elastic (i.e. significantly lower than the yield strain) throughout the loading, whilst a sharp departure from linearity occurs for the compressive strains at about 6.5 kNm, whereupon the compressive strains increase significantly with only a small increase in the applied moment. It should be noted that although the elastic critical buckling moment for local buckling is smaller than that for distortional buckling, the observed failure mode and hence the cross-sectional instability that triggered the sudden increase in compressive strains is believed to be distortional buckling and not local buckling, since only distortional buckling deformations were observed prior to the attainment of the ultimate load.
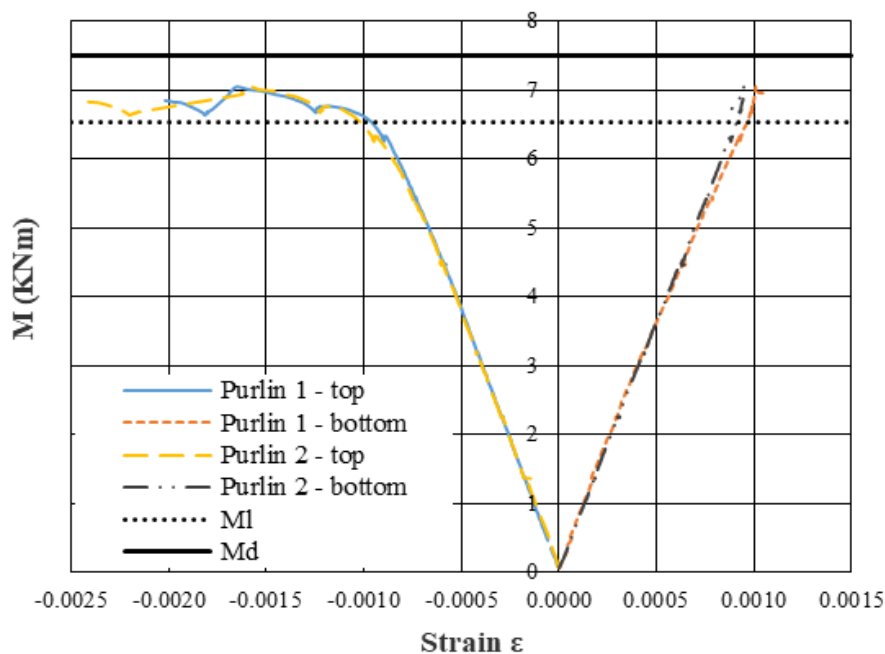
Figure 3.19 Moment-strain response of specimen Z17613.

Figure 3.20 depicts the evolution of strains with increasing load for specimen Z17625, which is the stockiest among tested cross-sections and the only one that exceeded its elastic moment resistance, denoted with a horizontal solid line in Figure 3.19. Contrary to the observations made for Z17613, both compressive and tensile stresses exhibit an almost identical behaviour prior to the attainment of the ultimate load, thus verifying that the cross-section remained fully effective until failure. Based on the material properties of Z17625 reported in Table 3.1, the yield strain was determined equal to 0.0022. Assuming a linear strain distribution throughout the section web, the theoretical strain values at the location of the strain gauges when the elastic moment resistance is reached (i.e. when the strain at the extreme fibre is 0.0022) have been determined equal to 0.0015 and are depicted in Figure 3.20 as dotted vertical lines. The theoretical strain values are in perfect agreement with the recorded compressive strains at the "top" strain gauge location and are very close to the values recorded by the "bottom" strain gauges, thus confirming material yielding occurred when M_{el} was reached and that the section exhibited inelastic bending capacity (Shifferaw and Schafer, 2012). Hence, the distortional buckling of the compressed flanges and the localised buckling of the lip that were observed during the test occurred after the attainment of the elastic moment resistance and were triggered by material yielding and the resulting loss of stiffness.
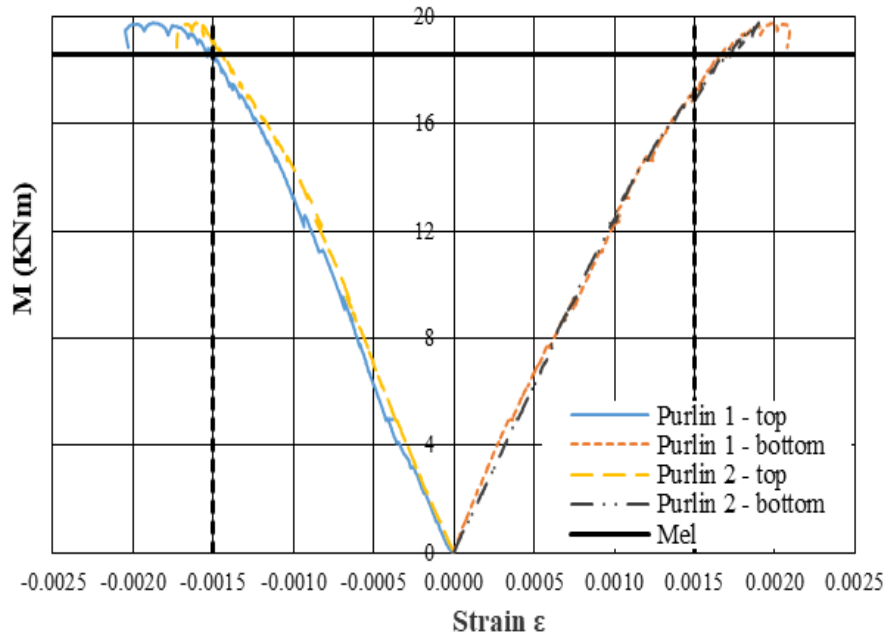
Figure 3.20 Moment-strain response of specimens Z17625.

Finally, the recorded strains are also utilised to determine the curvature of each purlin of the tested specimens. In Figure 3.21, the moment at midspan M, normalized by the elastic moment resistance M_{el}, is plotted against the curvature k, normalised by the curvature corresponding to the elastic moment resistance $k_{el}=M_{el}/EI$, for sections Z17613 and Z17625. The curvature is obtained by dividing the difference in the recorded strain values by the distance between the strain gauges. For specimen Z17613, both purlins exhibit an identical response which remains perfectly linear until the applied moment reaches 65% of the elastic moment resistance, whereafter distortional buckling occurs and the failure moment is reached. For specimen Z17625 yielding causes a gradual loss of stiffness beginning at approximately 80% of the elastic moment resistance, as shown in Figure 3.20 b). These observations are in accordance with the previous discussion on the moment-strain behaviour shown in Figures 3.19 and 3.20. Similar observations were made for the remaining specimens.
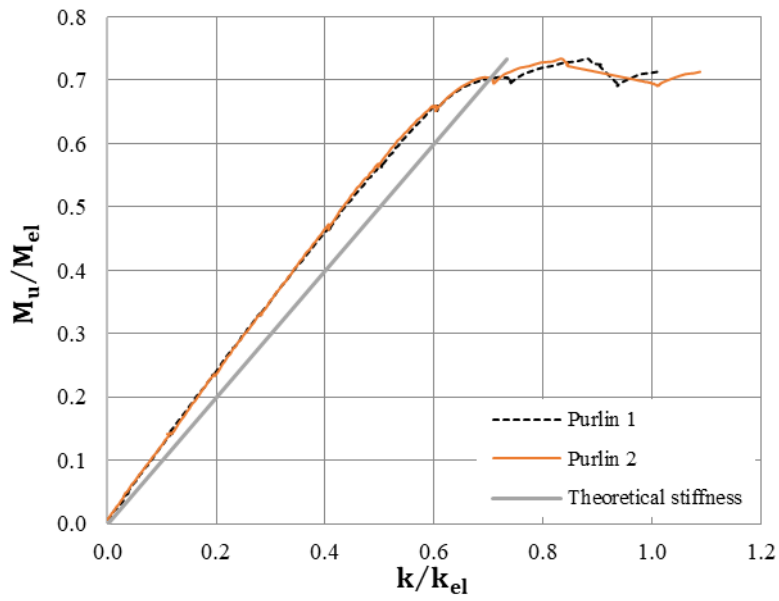
a) Z17613
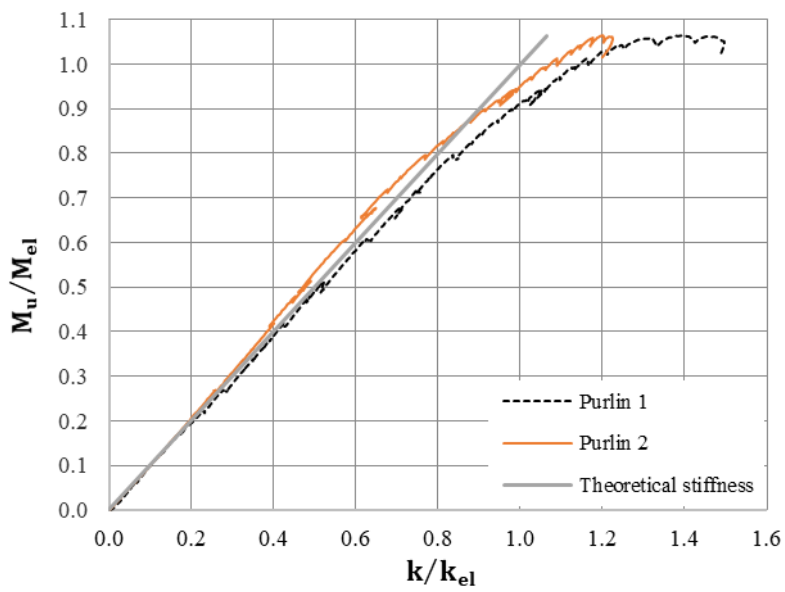
b) Z17625

Figure 3.21 Moment - curvature response of Z17613 and Z17625.

It should be noted that the above discussion was based on the results obtained for the

single test conducted for each nominal cross-section size considered. Experimental

variation in structural testing is to be expected and hence the behaviour of a single specimen may not be representative. To ensure the reliability of the obtained experimental results, the analytically determined stiffness has been compared to the experimentally obtained one and the agreement was observed to be perfect thus verifying the validity of the experimental setup as shown in Figure 3.12. Deviation from the linear response occurs with the occurrence of buckling, yielding or interactions thereof. The tested material coupons were seen to give very consistent results in terms of Young's modulus and yield strength (or nominal yield strength), hence the scatter of the material response can be said to be minimal and the reported material properties are deemed representative. The main source of potential experimental scatter is the occurrence of local and/or distortional buckling, the occurrence of which strongly depends on the geometric imperfections present in the specimens, which tend to vary significantly among nominally identical structural components. The effect of initial geometric imperfections on the structural response of purlins is studied in detail numerically in the following chapter.

3.4 Assessment of design codes

In this section the experimentally obtained moment resistances Mu are compared against the design predictions of two international structural design standards, namely Eurocode 3 (CEN, 2006a, CEN, 2006b) and the Direct Strength Method (DSM) (AISI, 2016).

As discussed in Chapter 2, the European design framework (CEN, 2006a, CEN, 2006b) for cold-formed steel sections is based on the concept of effective section, according to which the effect of cross-section instabilities on moment resistance is

accounted for by assuming that parts of the section are ineffective due to local and/or distortional buckling. The cross-section is treated initially as a collection of plated elements and the plate slenderness of the compressed elements is determined according to Equation 3.1:

$$\overline{\lambda_p} = \frac{c/t}{28.4\varepsilon\sqrt{k_\sigma}} \tag{3.1}$$

If $\overline{\lambda_p}$ is larger than the codified limits, an effective width factor ρ is determined according to the provisions of EN 1993-1-5 (CEN, 2006b) and parts of the compressed elements are assumed ineffective. Thereafter, the effect of distortional buckling is considered following the provisions of EN 1993-1-3 (CEN, 2006a), according to which the flange with the edge stiffener is treated as a compression element with continuous partial restraint the stiffness of which is defined according to the geometry of the cross-section.

It should be noted that the European guidance cannot be used to predict the expected failure mode, as the effects of local and distortional buckling are reflected simultaneously in the geometry of the effective section.

Contrary to the European design guidance that treats cross-sections as an assembly of their elements, the DSM treats cross-sections as a whole. The moment resistances to local buckling and distortional buckling, M_{nl} and M_{nd} respectively, are determined separately and the minimum of the two is the moment resistance M_{DSM}. Given that no lateral or torsional deformations of the purlins were observed during testing, restrained

bending about the geometrical axis parallel to the flanges of the sections was assumed in the determination of the elastic critical buckling moment using CUFSM, thus reflecting the effect of the employed sheeting and angle struts. Following this approach, the DSM predicts that all specimens would fail by distortional buckling (i.e. $M_{nl}>M_{nd}$), with the exception of specimen Z24615, for which local buckling is predicted. As discussed in Section 3.3.1, distortional buckling was observed for all specimens, hence the DSM correctly predicts the observed failure mode with the only exception being Z24615, for which M_{nl} is marginally smaller than M_{nd} (M_{nl}=12.79 kNm<M_{nd}=12.82 kNm).

Table 3.4 reports the design predictions for both methods based on measured geometry and material properties as well as predicted over experimental moment resistance ratios and the relevant non-dimensional slenderness values for distortional and local buckling λ_d and λ_l respectively. Furthermore, the moment resistance predictions of both design methods ($M_{pred.}$) are normalised by the experimental moment resistance (M_u) and plotted against non-dimensional slenderness values for distortional buckling λ_d in Figure 3.21. Overall, both design methods appear to offer reasonably accurate predictions for the tested sections with a mean predicted over experimental moment resistance of 0.87 and 0.95 for (CEN, 2006a, CEN, 2006b) and DSM (AISI, 2016) respectively and corresponding coefficients of variation of 7% and 9%. In both Table 3.4 and Figure 3.22 it can be seen that both design methods offer very similar predictions for stockier sections λ_d<1.04, whilst with increasing slenderness the DSM predicts higher bending resistances than the Eurocode 3, which on average are closer to the experimentally determined moment resistances.

Table 3.4 Assessment of design methods.

Section	M_u (kNm)	λ_d	λ_l	M_{EC3} (kNm)	M_{DSM} (kNm)	M_{EC3}/M_u	M_{DSM}/M_u
Z14613	5.94	1.07	1.07	4.51	5.29	0.76	0.89
Z14620	11.56	0.90	0.71	9.97	9.79	0.86	0.85
Z17613	7.04	1.13	1.21	5.63	6.83	0.80	0.97
Z17625	19.77	0.76	0.62	17.74	17.42	0.90	0.88
Z20620	15.62	0.97	0.89	14.40	14.79	0.92	0.95
Z24615	11.55	1.19	1.39	10.35	12.79	0.90	1.11
Z24620	20.33	1.04	1.05	18.41	19.11	0.91	0.94
Z30718	19.13	1.38	1.47	17.18	19.48	0.90	1.02
					Mean	0.87	0.95
					COV	0.07	0.09
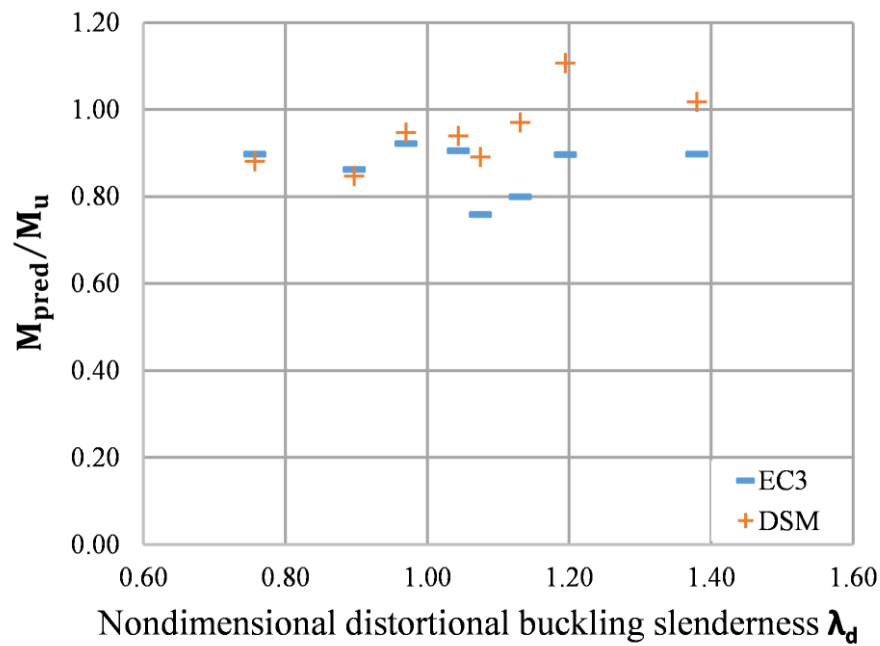
Figure 3.22 Comparison of Eurocode 3 (CEN, 2006a, CEN, 2006b) and DSM (AISI, 2016) moment resistance predictions against test results.

3.5 Summary

Eight experimental tests on twin purlins connected to each other with angle struts and cladding have been conducted and the key experimental results were reported in detail. It was observed that the structural response of the more slender (thinner) sections was linear until the attainment of the ultimate load, whereas for the stockier (thicker) sections gradual loss of stiffness due to yielding prior to failure was evident and the response became more curved close to the ultimate load. In general, the load–deflection curves of the twin purlins of the smaller sections (Z14613, Z14620, Z17613, Z17625, Z20620 and Z24615) were in close agreement with each other up to the ultimate load, thus revealing that the load and corresponding deformation was equally shared between the purlins comprising each specimen. However, for the larger and hence stiffer sections (Z24620, Z30718) some discrepancy was observed at the onset of loading. This is attributed to the fact that the struts and sheeting were sufficiently stiff to limit the pronounced twisting imperfections of the slender purlins, whilst this was not the case for the stiffer purlins as discussed in Section 3.3.2. For all specimens distortional buckling was the prevailing failure mode followed by local buckling of the lip for those sections having similar values of critical buckling stresses for local and distortional buckling. Finally, both the Eurocode 3 (CEN, 2006a, CEN, 2006b) and the DSM (AISI, 2016) were seen to offer conservative and consistent strength predictions, with the DSM predicting on average 8% higher strengths than the Eurocode 3 and correctly predicting the experimental failure mode as distortional buckling. The obtained experimental failure modes and load-deformation responses will be utilised in the following chapter (Chapter 4) to validate the developed numerical model, which will be utilized to optimize the lip size of lipped Z-sections.

Chapter 4: Numerical modelling and lip size to flange width ratio optimisation of cold-formed steel Z sections in bending

4.1 Introduction

This chapter reports a numerical study on the optimization of the lip size to flange width ratio of Z-sections under gravity loads. Numerical models of cold-formed steel Z purlins restrained by cladding and angle struts and subjected to sagging moment will be developed and validated against a total of 8 experimental results on Z-sections that failed in local or/and distortional buckling reported in Chapter 3. Models of varying levels of complexity will be generated and the key parameters affecting the structural response will be determined by means of a sensitivity analysis. The investigated parameters will include the magnitude, shape and combination of initial geometric imperfections pertinent to local and distortional buckling and the simplified or explicit modelling of test details such as struts and sheeting. After determining the appropriate modelling strategy that leads to the best balance between accuracy and computational cost, parametric studies will be conducted to investigate the effect of decreasing or increasing the lip size to flange width ratio on the sections' moment resistance and corresponding failure mode. Based on the parametric study results, the optimal lip size to flange width ratio which maximizes the moment to weight ratio for each section will be determined. Finally, all generated FE results are utilized to evaluate the accuracy of the moment resistance prediction of Eurocode 3 and the Direct Strength Method.

4.2 Numerical modelling

The finite element software ABAQUS (Simulia, 2014) was utilized to generate the numerical models that simulate the response of Z purlins subjected to sagging moment. In all numerical models, geometric imperfections and material non-linearity

were employed to obtain a realistic estimation of the flexural strength. It is noted that the failure modes considered in the FE simulations include local and distortional buckling only in accordance with the experimental results reported in chapter 3 against which the FE models were validated. All FE models have a clear span length of 3 meters, whilst four-point load were applied at fifth points of the beams to approximate a uniformly distributed load in accordance with the tests. Details on the modelling assumptions are given in the following sections.

4.2.1 Element type and discretization

The linear 4-nodded shell element S4R with reduced integration was used to discretise the modelled purlins as it was shown to perform well in similar studies (Schafer et al., 2010, Haidarali and Nethercot, 2011, Wang et al., 2016, Kyvelou et al., 2018). To obtain a good balance between accuracy and computational cost, a mesh convergence study was conducted on a typical purlin by running successive analyses with increasingly finer meshes and plotting the obtained strength against the number of elements.   In all models the assumptions reported in the following sections were employed and only the mesh size was varied, whilst keeping the aspect ratio of the elements close to unity. A mesh convergence study involving six different mesh sizes namely 30, 25, 20, 15, 12 and 10 mm was carried out. Figure 4.1 summarises the results of the mesh convergence study for a typical purlin where it can be clearly observed that decreasing the mesh has a marked influence of the obtained results until a mesh size of 12x12, whereafter the results do not change significantly. Therefore, a uniform mesh size of 12x12 is employed for the flat plated parts of all models, whilst 3 elements were used to discretise the curved corner regions and 3

elements were used over the flat lip depth. A typical meshed model with a mesh size of 12x12 is shown in Figure 4.2. The same discretization was employed in the parametric studies.
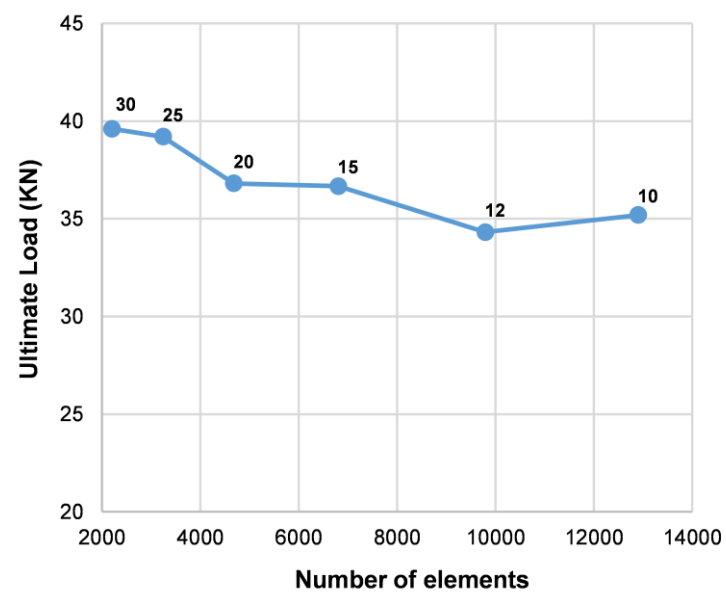
Figure 4.1 Mesh convergence study.
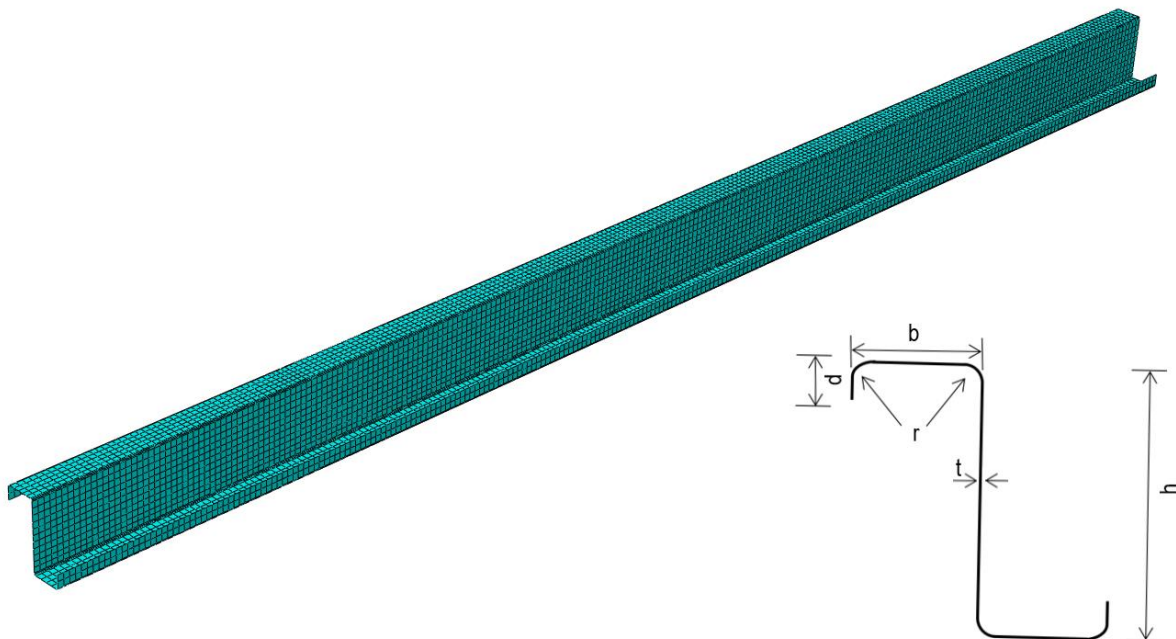
Figure 4.2 A typical mesh discretising a purlin and cross-section geometry.

4.2.2 Initial geometric imperfections

Geometric imperfections are defined as deviations of a member actual geometry from its nominal one. The magnitude and combination of initial geometric imperfections have a significant impact on section capacity and structural response; therefore, they need to be included carefully in the models. Since this study investigates the behaviour of laterally restrained purlins and given that all specimens failed by local or distortional buckling, only initial geometric imperfections pertinent to local and distortional buckling mode shapes were considered.

In the Chapter 3, based on the results of which the FE models are validated herein, no geometric imperfection measurements were reported. This was due to the tests having been performed on twin purlin specimens assembled from individual purlins connected to each other via angle struts and restrained at the top by profiled sheeting. The assembly process introduced additional geometric imperfections or eliminated preexisting ones in individual purlins as discussed in Chapter 3. Therefore, in this study, the initial geometric imperfections were treated as a modelling convenience to trigger buckling and failure in the desired mode, rather than as a physical reality (Schafer et al., 2010). To this end a linear eigenvalue buckling analysis was initially conducted and the buckling mode shapes corresponding to the lowest critical stress pertinent to local buckling (i.e. short halfwave length) and distortional buckling (long halfwave length) were utilized to perturb the initial geometry and trigger buckling. Figure 4.3 shows typical mode shapes for local and distortional buckling extracted from eigenvalue analysis.

(a)

(b)
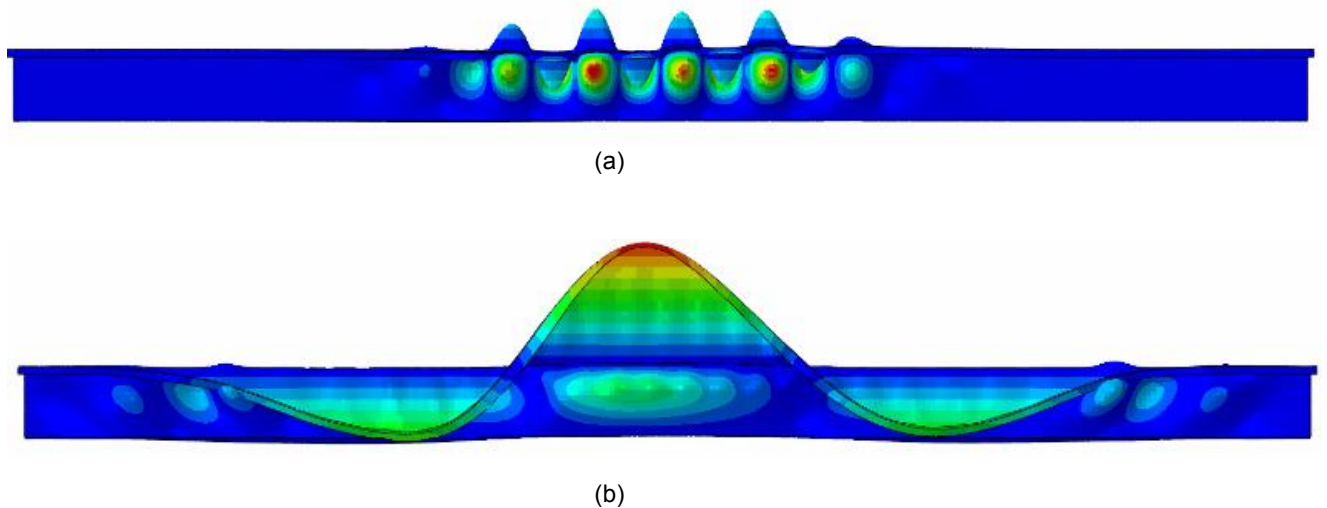
Figure 4.3 Typical buckling mode shapes for (a) local and (b) distortional buckling.

Three different values for the magnitudes of the imperfections corresponding to local and distortional buckling were considered as summarised in Table 4.1. The imperfection magnitude values stated as fractions of the section thickness for cases a and b were obtained from statistical data for lipped channel sections reported by Zeinoddini and Schafer (2012) and correspond to the 50% and 75% percentile of the cumulative distribution function of measured geometric imperfections for local and distortional buckling. Case c utilises a Dawson and Walker (1972) type of equation to estimate the magnitude of the geometric imperfection for distortional buckling, assuming that the magnitude depends on the cross-section slenderness, whilst for the local buckling imperfection amplitude, the value h/200 recommended in Annex C of EN 1993-1-5 (CEN, 2006b) has been adopted herein, where h is the overall depth of the section. The critical buckling stress for distortional buckling, which is required to determine the imperfection amplitude for the distortional buckling mode shape, was determined using the software CUFSM (Li and Schafer, 2010).

Table 4.1 Amplitudes considered for initial geometric imperfections.

	Local imperfection	Distortional imperfection
a	0.31 t	0.75 t
b	0.54 t	1.14 t
c	$(h/200)$	$0.3 * t * (\sigma_{0.2}/\sigma_{crd})^{0.5}$

The initial geometric imperfection f_0 applied to each model was simulated as a linear combination of the imperfections for local and distortional buckling in accordance with Equation 4.1, where α_i is the magnitude for each mode predicted by the 3 amplitudes considered from Table 4.1, C_i is a coefficient that controls the sign and portion of the amplitude and $\emptyset_i$ is the mode shape (Zeinoddini and Schafer, 2012).

$$f_0 = \sum_i \alpha_i C_i \emptyset_i \qquad i = \text{number of mode shape} \tag{4.1}$$

A thorough explanation of numerical imperfections modelling strategies can be found in (Zeinoddini and Schafer, 2012). As summarised in (Zeinoddini and Schafer, 2012), there are two classical approaches to determine C_i, namely the circle-SRSS (square root of the sum of squares) and the square-max. A graphical representation of these methods is shown in Figure 4.4, where C_L and C_d are the coefficients for imperfections corresponding to local and distortional buckling, respectively. In the square-max approach, the maximum magnitude for every mode with different signs is considered, while in the SRSS, the relationship between the amplitudes of the two mode shapes is defined by Equation 4.2.

$$\sqrt{C_L{}^2 + C_D{}^2} = 1 \qquad\qquad (4.2)$$

The numbered points in Figure 4.4 define various possible combinations of the two buckling mode shapes. These include combinations 1-4 according to the square-max method and combinations 5-8 following the SRSS method. It has to be noted that only cases 1, 2, 5, 6 are considered in this analysis because, as observed in the tests reported in Chapter 3, distortional buckling occurred only in the opening mode (i.e. outwards) hence considering cases with a negative sign (closing mode) would not accurately capture the observed failure modes. For each specimen, twelve analyses were carried out (i.e. 3 imperfection magnitudes and 4 combinations of imperfections) in order to obtain the magnitude and combination of imperfections that leads to the best agreement with the test experimental results. This is discussed later in the validation section of this study.
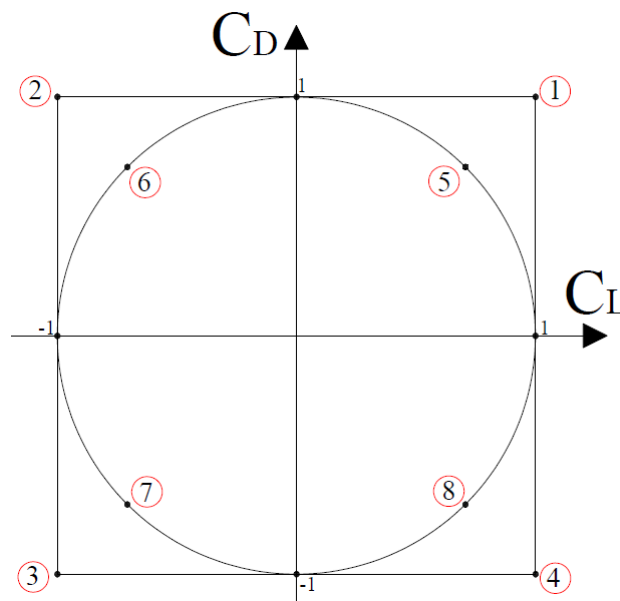
Figure 4.4 Square-max and circle-SRSS approaches.

4.2.3 Materials properties, residual stresses and corner strength enhancements

The experimental results from tensile coupon tests extracted from the flange of sections cut from the same member length as that used for the tested sections are reported in the Chapter 3. All sections had a nominal yield strength of 450 MPa, with the experimentally determined one being 466 MPa on average. Young's modulus was 200000 MPa on average with very small variations. Some of the material coupons exhibited gradual yielding, whilst most stress-strain curves displayed a well-defined yield plateau followed by strain-hardening. In the numerical analyses reported herein the experimentally derived material response was adopted for the validation of the models. The two stage Ramberg Osgood material model originally proposed in (Mirambell and Real, 2000) and modified in (Gardner and Nethercot, 2004) as given in Equations 4.3 and 4.4 for the 1st and 2nd stage, respectively, was used to simulate the nonlinear material behaviour.

$$\varepsilon = \frac{\sigma}{E} + 0.002 \, (\sigma/\sigma_{0.2})^n \qquad \text{For } \sigma \leq \sigma_{0.2} \qquad (4.3)$$

$$\varepsilon = \frac{(\sigma - \sigma_{0.2})}{E_{0.2}} + \left(\varepsilon t_{1.0} - \varepsilon t_{0.2} - \frac{\sigma_{1.0} - \sigma_{0.2}}{E_{0.2}} \right) \times \left(\frac{\sigma - \sigma_{0.2}}{\sigma_{1.0} - \sigma_{0.2}} \right)^{n_{0.2,1.0}} + \varepsilon t_{0.2} \quad \text{For } \sigma > \sigma_{0.2} \qquad (4.4)$$

In these equations, n is the non-linear parameter exponent of the classical Ramberg-Osgood model ranged between 17 and 20 for the material reported in Chapter 3, E is the Young's modulus, $\sigma_{0.2}$ is the proof stress corresponding to 0.2 % plastic strain, $\sigma_{1.0}$ is the proof stress corresponding to 1 % plastic strain, $E_{0.2}$ is the tangent modulus at

0.2% proof stress , $E_{0.2} = \dfrac{E}{1+0.002\text{n}\frac{E}{\sigma_{0.2}}}$, $\varepsilon t_{0.2}$ is the total strain at the 0.2% proof stress

$\varepsilon t_{0.2} = 0.002 + \sigma_{0.2}/E$, $\varepsilon t_{1.0}$ is the total strain at the 1% proof stress $\varepsilon t_{1.0} = 0.01 + \sigma_{1.0}/E$ and $n_{0.2,1.0}$ is a strain hardening coefficient for a curve that passes through $\sigma_{0.2}$ and $\sigma_{1.0}$. The value of $n_{0.2,1.0}$ ranges from 0.9 to 2 for the material reported in chapter 3.

As later observed, the effect of material modelling on the numerical results was not significant due to the high slenderness of the simulated sections.

The engineering stress-strain curves defined by Equations 4.3 and 4.4 namely σ_{nom} and ε_{nom} were converted into true stress σ_{true} and logarithmic plastic strain $\varepsilon_{pl,true}$ as required by ABAQUS according to Equations 4.5 and 4.6.

$$\sigma_{true} = \sigma_{nom}\left(1 + \varepsilon_{nom}\right) \tag{4.5}$$

$$\varepsilon_{pl,true} = \ln\left(1 + \varepsilon_{nom}\right) - \sigma_{nom}/E \tag{4.6}$$

As discussed in section 2.1.2, and, in line with (Schafer and Peköz, 1998, Dubina and Ungureanu, 2002, Yu and Schafer, 2007, Haidarali and Nethercot, 2011, Li et al., 2013), neither the strength enhancements of the corner regions nor the bending residual stresses have been explicitly modelled.

4.2.4 Modelling of structural details

Boundary conditions significantly affect the structural response of the FE models, hence they need to accurately reflect the actual support conditions employed in practice. The tests that are simulated herein, employed twin purlins connected to one another via angle struts as discussed in Chapter 3 and shown in Figure 4.5.
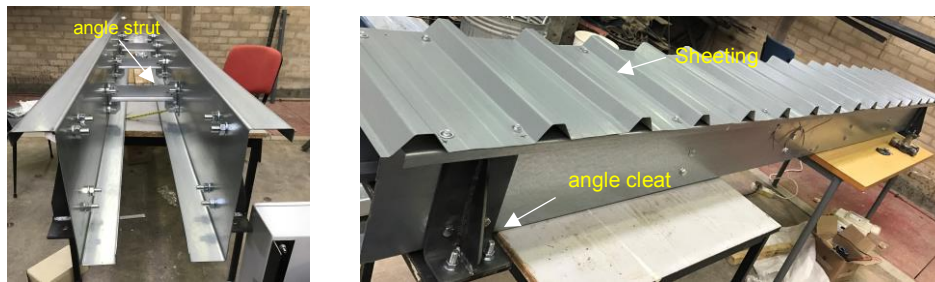
Figure 4.5 Detail of the angle struts (left) and sheeting and angle cleat (right).

Given the importance of the restrain provided by the sheeting and the angle struts to the purlins, their effect needs to be incorporated in the FE models. The most accurate but also computationally expensive approach is to explicitly model the sheeting and angle struts with shell elements and account for the contact between sheeting and purlins, whereas a computationally less expensive simplification would be to replace the sheeting and angle struts with relevant support conditions, i.e. restraining the purlin against out of plane deflections at the locations where it is connected to angle struts and sheeting. In between these two extremes are the options involving explicit modelling of only the sheeting or the angle struts with the effect of the other simulated as boundary conditions, as outlined in Table 4.2, where four modelling approaches of varying complexity are summarised and assessed with respect to their computational cost and complexity. The corresponding geometry of the FE models is shown in Figure 4.6. For all cases, to increase computational efficiency, the symmetry with respect to

boundary conditions, loading and observed failure mode was exploited and only one of the twin purlins was modelled with suitable boundary conditions simulating the effect of the presence of the twin purlin. In all models the loads were applied as equal point loads on the flange whilst the support reactions, were applied on the end sections which were constrained to remain rigid via kinematic coupling, thus reflecting the presence of the angle cleat shown in Figure 4.5.

Table 4.2 Modelling approaches considered.

Modelling strategy	Computational Cost	Complexity
Model a: effect of struts and cladding modelled as boundary conditions	Low	Low
Model b: struts and cladding explicitly modelled	High (necessitates modelling of contact, convergence issues)	High (necessitates modelling of contact)
Model c: struts modelled as boundary conditions, cladding modelled explicitly	High	High (necessitates modelling of contact)
Model d: struts explicitly modelled, cladding modelled as boundary condition	Low (additional degrees of freedom)	Moderate (strut details affect analysis-optimization not valid for other strut details)
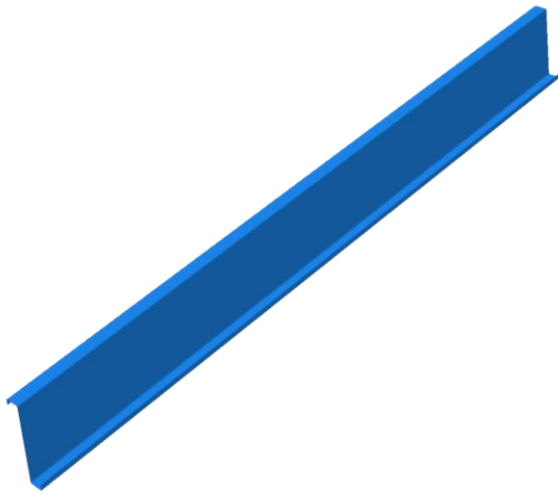
(i)
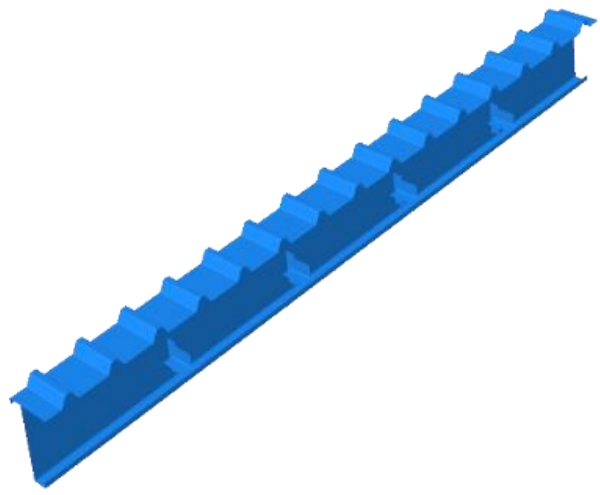
(ii)
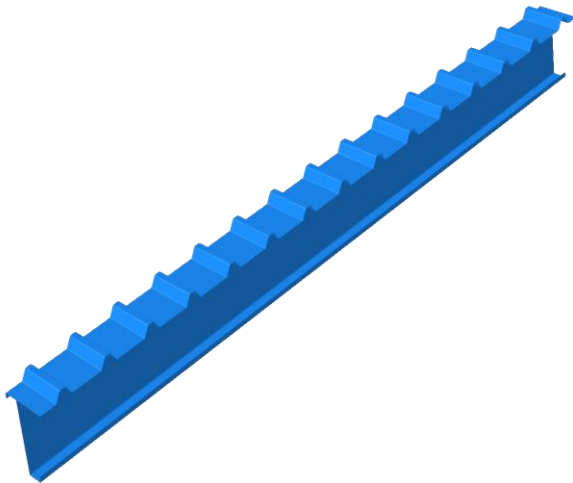
(iii)
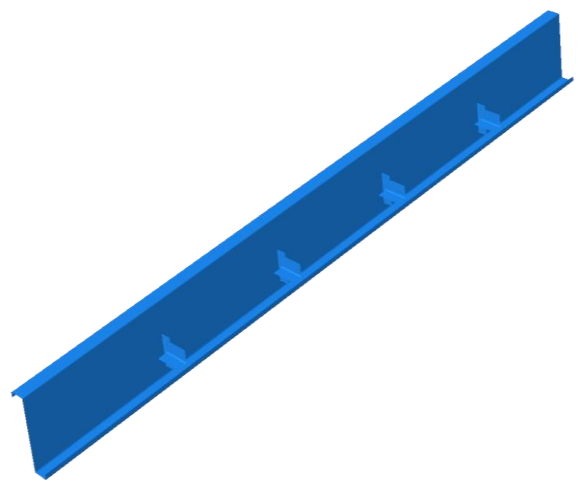
(iv)

Figure 4.6 Four different modelling strategies with varying complexity corresponding to Table 4.2.

The boundary conditions employed for the simplified model (model i) are shown in Figure 4.7, where the z-axis (DOF 3) corresponds to the longitudinal member axis, the y-axis (DOF 2) is parallel to the web and the x-axis (DOF 1) is parallel to the flange. For models (ii) and (iv), where the struts are explicitly modelled, tie constrains were used to model the connection of the struts to the purlin. To model the contact between the cladding (for model ii , iii) and the compression flange of the beam, general contact with hard behaviour in the normal direction and frictionless behaviour in the tangential direction was assumed. The differences between the four models outlined in Table 4.2 are discussed hereafter.
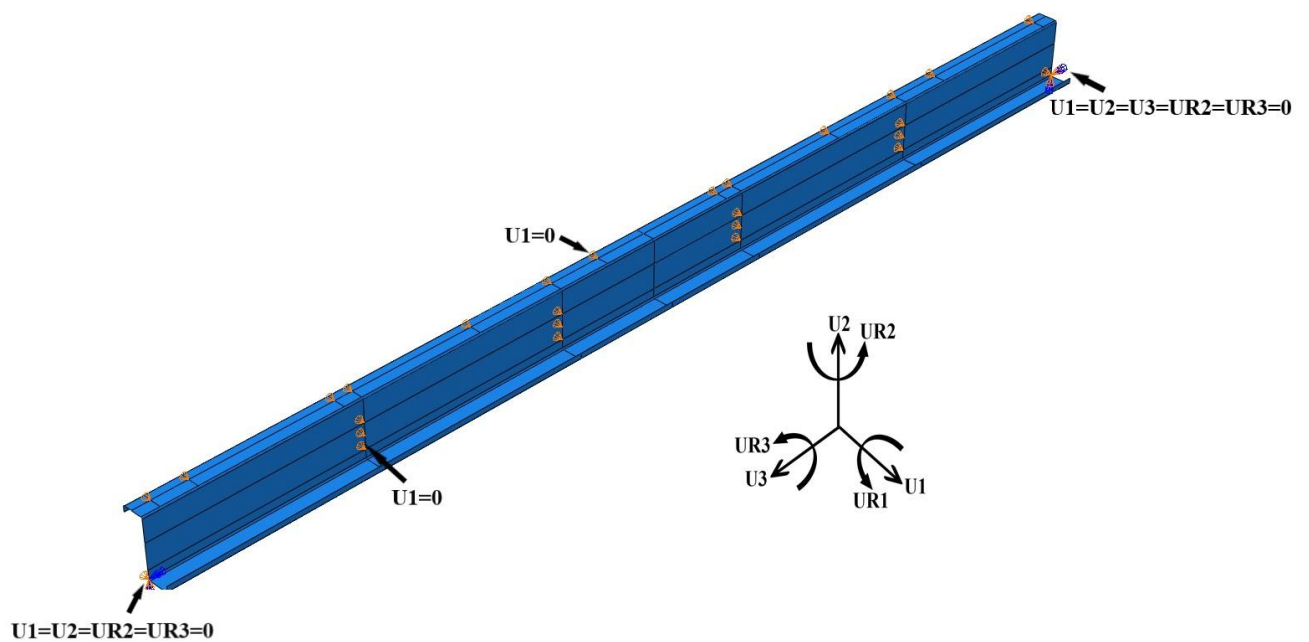
Figure 4.7 Boundary conditions.

4.3 Validation

The accuracy of the four modelling strategies employed to simulate the effect of struts and cladding on the structural response of the modelled purlins is assessed by comparing the resulting behaviour against obtained tests results. The difference between the four models is quantified in Table 4.3 in terms of moment resistance, where all 8 specimens have been modelled following the four modelling strategies discussed previously, whilst the effect of the adopted modelling strategy on the overall structural response is demonstrated in Figure 4.8 for purlin Z24620. In Table 4.3, where M_{FE} and M_T are the obtained maximum moment from numerical models and tests respectively, an excellent agreement with the experimental results is observed for all modelling strategies considered, with model (iii) displaying the best strength predictions on average and model (iv) the lowest scatter. However, the marginal improvement in accuracy when the struts and/or cladding are explicitly modelled is outweighed by the significant increase in computational cost. Furthermore, the focus of this study is the behaviour of the purlin sections rather than the effect of structural details, hence the simplified modelling approach (i) will be employed in the remainder of the study.

Table 4.3 Effect of modelling approach on the accuracy of the predictions.

Specimen	M_{FE} / M_T (i)	M_{FE} / M_T (ii)	M_{FE} / M_T (iii)	M_{FE} / M_T (iv)
Z14613	0.95	0.97	0.96	0.97
Z14620	1.02	0.99	0.94	1.02
Z17613	0.97	0.96	0.99	0.97
Z17625	1.01	1.01	0.98	1.01
Z20620	1.08	1.10	1.08	1.08
Z24615	1.14	1.09	1.04	1.07
Z24620	1.04	1.04	1.04	1.04
Z30718	0.94	1.02	1.00	1.02
Average	1.02	1.02	1.00	1.02
COV	0.06	0.05	0.05	0.04

(a) Z14613
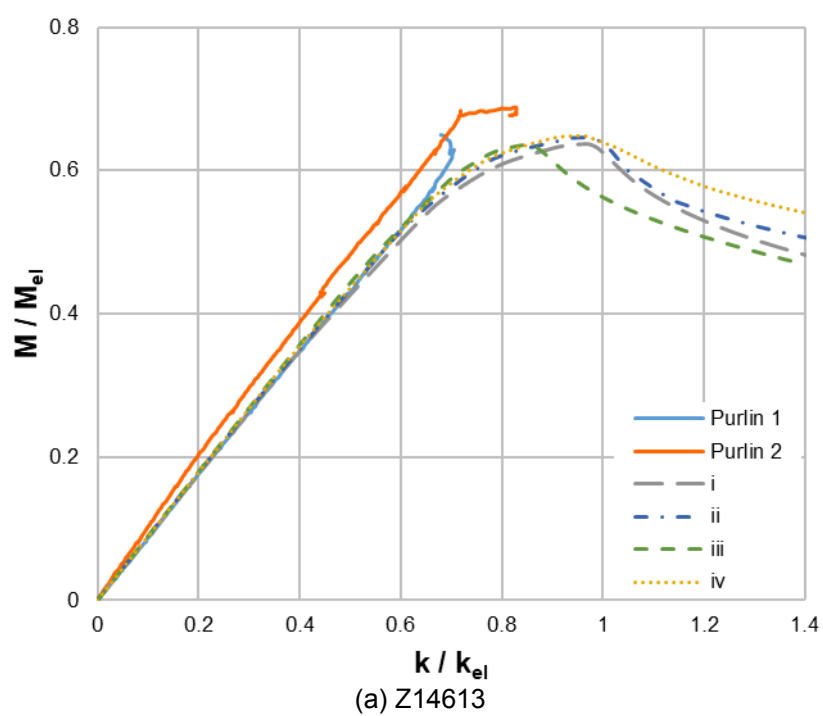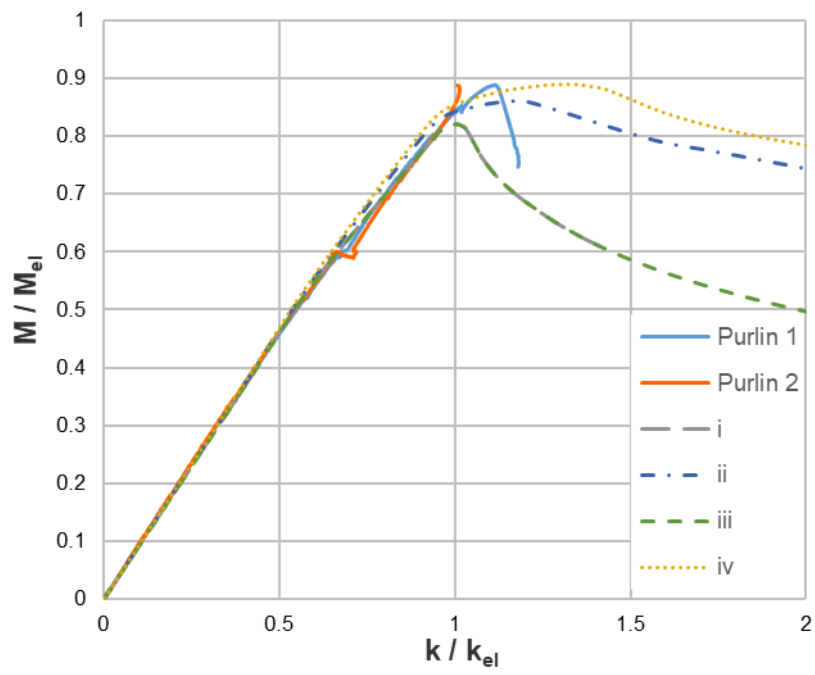
(b) Z14620
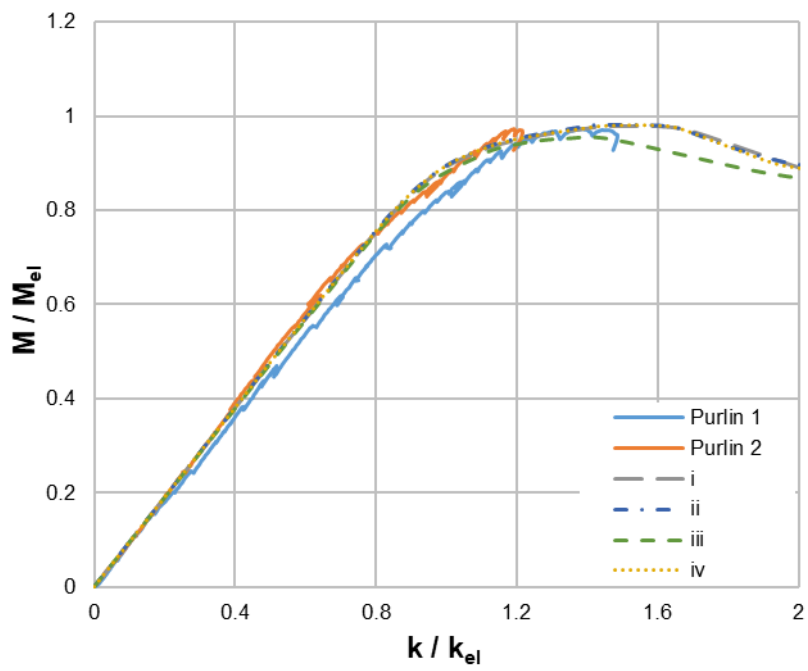
(c) Z17625
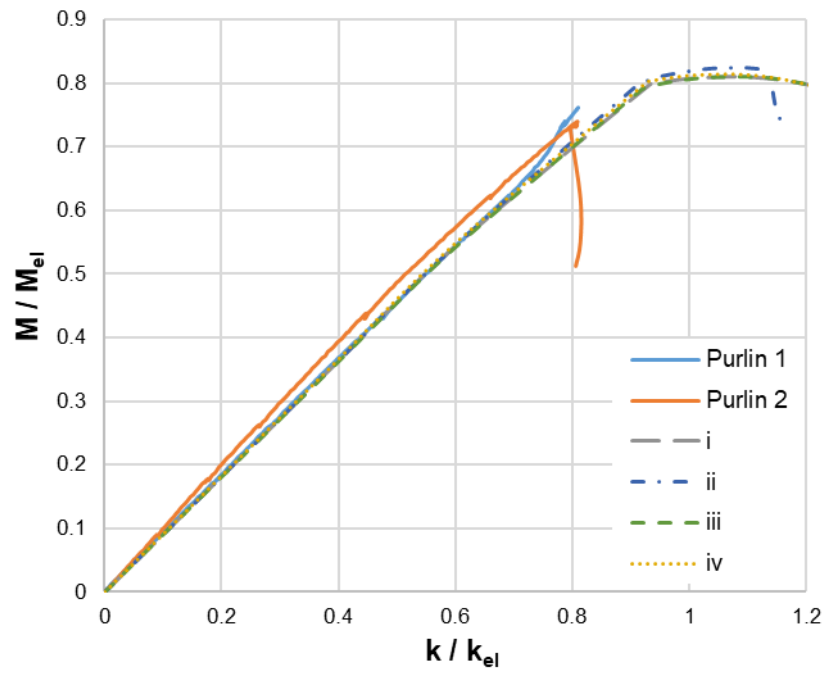
(d) Z20620
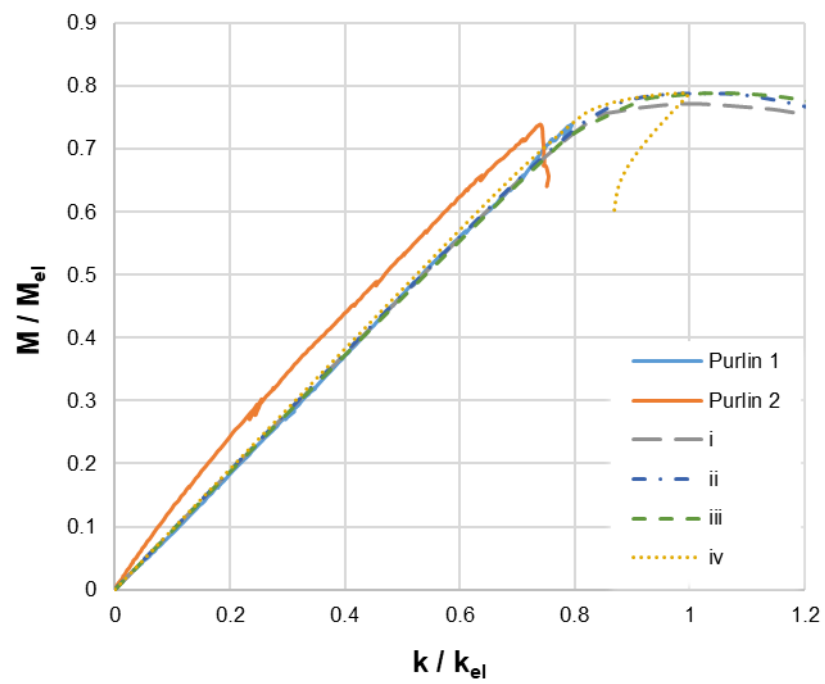
(e) Z24620
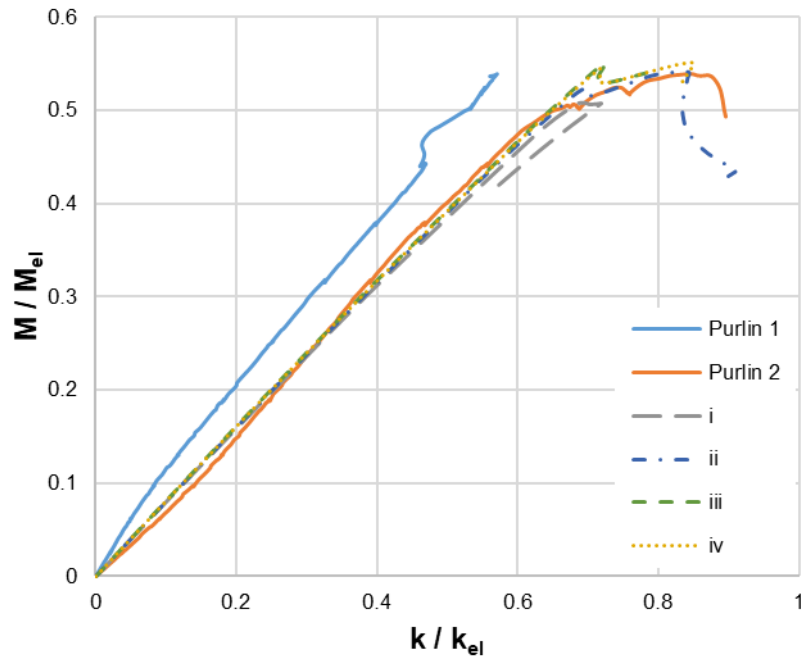
(f) Z30718

Figure 4.8 Effect of modelling approach on the moment-curvature response of purlins

To investigate the effect of the initial imperfections on the numerical flexural strength and select the most appropriate imperfection amplitudes and combinations of local and distortional buckling mode shapes, the numerically obtained results are compared against the experimental results for all combinations of initial geometric imperfections considered, as reported in Table 4.4. The numbers 1, 2, 5 and 6 in Table 4 correspond to the type of combination employed for the local and distortional buckling imperfections as shown in Figure 4.4, whereas the letter a , b and c correspond to the imperfection amplitudes reported in Table 4.1. All obtained results are based on the simplified modelling strategy (i). Overall, the FE results can accurately capture the experimentally observed failure modes, as shown in Figure 4.9, where the experimental and numerical failure modes of purlins Z14620, Z20620 and Z17625 are depicted. In all cases the observed failure modes, including distortional and local buckling are accurately predicted by the FE models.

Table 4.4 Effect of initial geometric imperfections on numerical flexural strength.

Case	1			2			5			6		
Section	M_{FE}/M_T a	M_{FE}/M_T b	M_{FE}/M_T c	M_{FE}/M_T a	M_{FE}/M_T b	M_{FE}/M_T c	M_{FE}/M_T a	M_{FE}/M_T b	M_{FE}/M_T c	M_{FE}/M_T a	M_{FE}/M_T b	M_{FE}/M_T c
Z14613	0.98	0.93	0.96	0.97	0.92	0.95	1.01	0.96	0.98	1.00	0.96	0.98
Z14620	1.01	1.00	1.02	1.01	1.00	1.02	1.01	1.01	1.02	1.01	1.01	1.02
Z17613	0.99	0.95	0.97	0.98	0.94	0.97	1.01	0.99	0.99	1.00	0.97	0.99
Z17625	0.98	0.97	1.01	0.98	0.97	1.01	0.99	0.98	1.01	0.99	0.98	1.01
Z20620	1.07	1.04	1.08	1.07	1.04	1.08	1.09	1.06	1.11	1.09	1.05	1.09
Z24615	1.12	1.10	1.14	1.13	1.11	1.07	1.14	1.11	1.15	1.15	1.13	1.09
Z24620	1.03	0.99	1.04	1.04	1.01	1.01	1.05	1.02	1.05	1.05	1.03	1.03
Z30718	1.01	1.00	0.95	1.03	1.02	0.94	0.95	1.01	0.94	1.04	1.03	0.96
Average	1.02	1.00	1.02	1.03	1.00	1.01	1.03	1.02	1.03	1.04	1.02	1.02
COV	0.049	0.053	0.064	0.054	0.060	0.050	0.058	0.049	0.066	0.053	0.054	0.046

For completeness, and to highlight the importance of incorporating initial geometric imperfections pertinent to both local and distortional buckling, the numerical over experimental flexural strength for the purlins considered is reported in Table 4.5, where the obtained results are based on employing only one buckling mode shape, pertinent to either local or distortional buckling. The utilized amplitudes are the ones reported in Table 4.1 as amplitudes (c). It can be clearly seen that employing only one buckling mode shape that considering a pure imperfection mode, whether local or distortional, will lead to higher predictions and increased scatter for the moment resistances and overall a worse agreement with the experimental results is obtained compared to using mode shapes representative of both local and distortional buckling.

Table 4.5. Effect of pure initial geometric imperfections on numerical flexural strength

Section	M_{FE}/M_T C_d	M_{FE}/M_T C_d (-)	M_{FE}/M_T C_L	M_{FE}/M_T C_L (-)
Z14613	1.12	1.15	0.95	0.96
Z14620	1.02	1.04	1.02	1.02
Z17613	1.04	1.03	0.98	0.98
Z17625	1.01	1.00	1.01	1.01
Z20620	1.12	1.18	1.12	1.13
Z24615	1.16	1.17	1.17	1.17
Z24620	1.08	1.09	1.07	1.07
Z30718	1.05	1.10	0.95	1.07
Average	1.08	1.10	1.04	1.06
COV	0.049	0.061	0.092	0.076

The imperfections (b) and (c) (see Table 4.1) following the combinations 1 and 2 provide a better agreement with the experimental results compared to combinations 5 and 6, which display a higher predicted moment resistance and increased scatter. Based on the obtained results, combination 2 of the initial geometric imperfections with

amplitudes (c) as shown in Table 4.1, is deemed suitable and is adopted hereafter in the parametric studies. The average ratio of numerical over experimental moment resistance for all 8 tests is 1.01 with a coefficient of variation (COV) of 0.05.
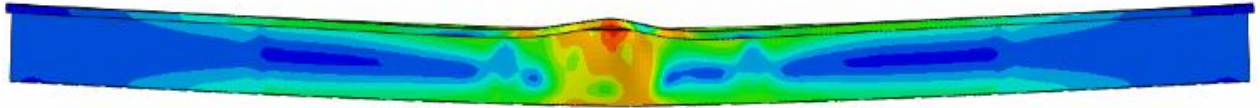
(a) Z14620
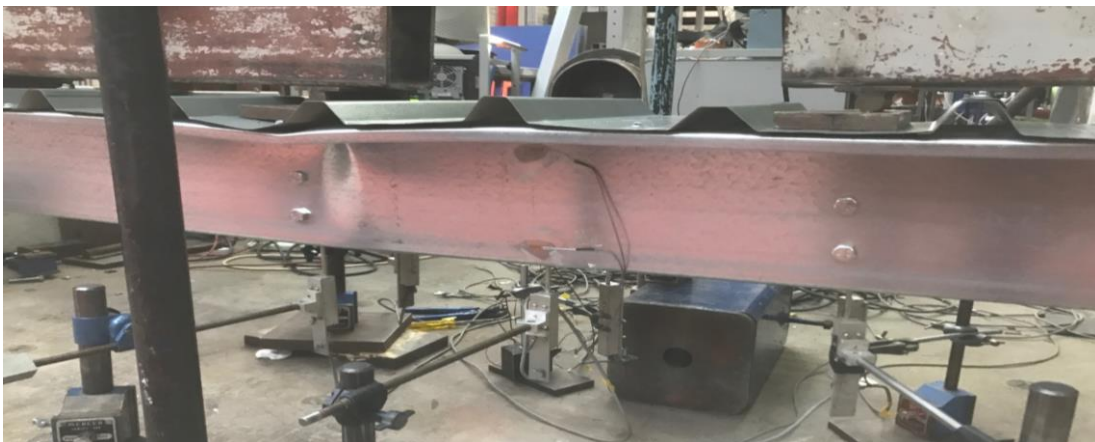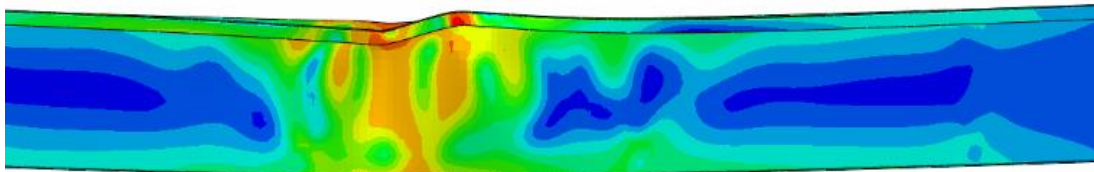
(b) Z20620
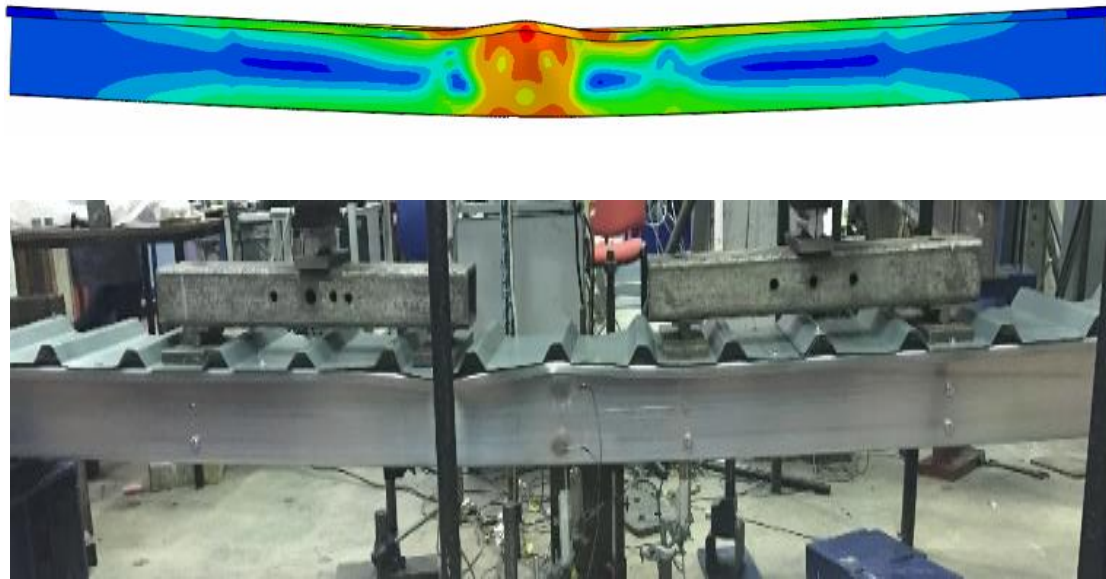
(c) Z17625

Figure 4.9 Experimental and numerical failure modes for typical purlins.

4.4 Parametric studies

Having determined the optimal modelling strategy to account for the effect of geometric imperfections and the effect of sheeting and struts at modest computational cost, parametric studies were carried out to study the effect of decreasing or increasing the lip size to flange width ratio on the sections' moment resistance, assess existing design standards and ultimately optimize the cross-section's lip depth.

The cross-section geometries considered in the parametric studies are reported in Table 4.6 and include seven nominal section depths ranging from 146 mm to 307 mm. Each of the seven section depths is hereafter referred to with the nominal depth in mm following the letter Z and includes a family of sections with similar midline dimensions but different thicknesses. A range of thicknesses was considered to cover a wide range of cross-section slendernesses, whilst the flange width ranging from 62.5 mm

to 75 mm was employed in line with (Albion Sections, 2019). Six lip depths namely 15 mm, 17.5 mm, 20 mm, 25 mm, 30 mm and 35 mm were taken into consideration. It should be noted that all section depths considered currently have a nominal lip size of 20 mm (Albion Sections , 2019). For some of the deeper sections further analysis with deeper lip sizes was conducted to assure that the most efficient cross-section is obtained. It should be noted that all the lip sizes employed in the numerical analysis are within the limits specified in EC3 (CEN, 2006a) for the allowable lip size over flange width ratio (i.e.$0.2 \leq d/b \leq 0.6$). Rounded corners with an internal radius of 4 mm were adopted for all sections in agreement with the average values measured in Chapter 3. The beam length for all sections was fixed at 3 m, thereby resulting in a span to depth ratio ranging from 10 to 21. In agreement with the experimental reported in Chapter 3, four-point loads were applied at a distance of 600 mm from one another and from the supports. Neither corner strength enhancements nor residuals tresses were explicitly considered in the parametric studies, whilst the initial imperfection amplitudes (c) of Table 4.1 combined according to combination 2 shown in Figure 4.4 was adopted as previously discussed.

On average the yield strength/nominal yield strength of the tested coupons was very close to the value of 450 MPa given in the mill certificates. Moreover, the Young's modulus value was on average 200000 MPa. As previously stated, two distinct types of material response were observed, an elastic plastic one and a rounded one displaying gradual yielding.

To account for the two distinct types of material behaviour obtained from material coupon testing reported in Chapter 3, two material models were considered, since some coupon test results displayed a yield plateau and others did not. The first material model employs an elastic perfectly plastic stress-strain relationship (EPP) with a yield strength equal to 450 MPa. The second material model considered was a two stage Ramberg-Osgood (R-O) material equation parameters of which are given in Table 4.6. For the rounded material response, the material parameters that provided the best fit to the experimental curve for the 1.76 mm thick coupon was scaled down so that the nominal yield strength is equal to 450 MPa. This material response was chosen because the 1.76 mm thick coupon lies in the middle of the range of thicknesses tested and is considered representative for all materials tested herein. For both material models, the Young's modulus was assumed equal to 200 GPa in line with the material coupon test results and the Poisson's ratio was taken equal to 0.3. The effect of the adopted material model on the obtained failure mode is shown in Figure 4.10, for two typical purlins, where the EPP material can be seen to lead to well defined plastic zones, whilst the effect of strain hardening of the R-O material leads to a more gradual yielding in regions with high stress concentrations.

For each material model assumed, 295 geometric configurations were modelled, hence the parametric study consists of 590 FE simulations. The obtained results are utilised hereafter to determine the optimal lip size to flange width ratio for each modelled Z-section and to assess the accuracy of Eurocode 3 (CEN, 2006a, CEN, 2006b) as well as the Direct strength method (DSM) (AISI, 2016).

Table 4.6 Summary of geometric configurations and material models used in parametric studies.

Section	h (mm)	b (mm)	t (mm)	d (mm)	Material		
Z146	145	62.5	1.3, 1.4, 1.5, 1.6, 1.8, 2	15, 17.5, 20, 25, 30, 35	$f_y = 450$ MPa	$E = 200$ GPa	$\sigma_{0.2} = 450$MPa, $\sigma_{1.0} = 455$MPa, $E = 200$ GPa, $n = 11$, $n_{0.2,1.0} = 1.5$
Z176	175	62.5	1.3, 1.4, 1.5, 1.6, 1.8, 2, 2.3, 2.5				
Z206	200	65	1.3,1.4, 1.5,1.6, 1.8, 2, 2.3, 2.5				
Z226	225	65	1.4, 1.5, 1.6, 1.8, 2, 2.3, 2.5				
Z246	245	65	1.5, 1.6, 1.8, 2, 2.3, 2.5, 3				
Z266	265	65	1.6, 1.8, 2, 2.3, 2.5, 3				
Z307	300	75	1.8, 2, 2.3, 2.5, 3				

(a)

(b)

Z24623

(a)

(b)

Z30720
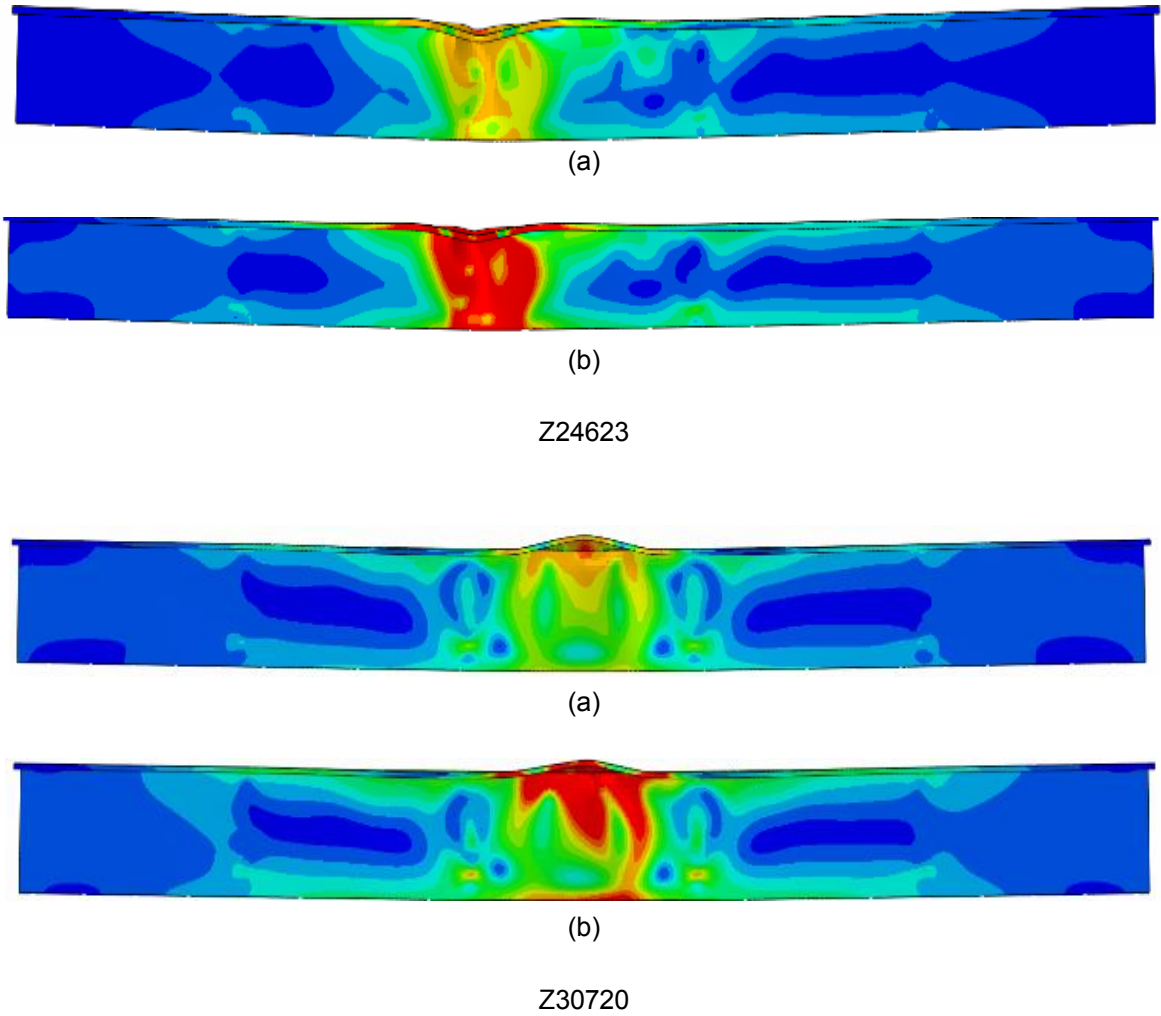
Figure 4.10 Comparison between the failure modes of (a) R-O material and (b) EPP material.

4.5 Results and discussion

For all sections considered in the parametric study, the moment resistance M_{FE} was extracted and normalised by the weight of the modelled section per meter length W to quantify the effect of increasing the lip size to flange width ratio on both strength and weight and obtain the optimal lip size to flange width ratio that maximises the strength-to-weight ratio for each section depth considered. It is noted that the current lip size for all section depths considered herein is 20 mm (Albion Sections, 2019).

With regard to failure mode, it was observed that when increasing the lip size, the distortional buckling strength increases considerably more than the local buckling strength of the cross-section, hence the failure mode shifts from distortional to local buckling. Furthermore, the lip itself may undergo local buckling for large lip sizes, whereafter distortional buckling occurs imminently.

For each group of cross-sections with the same depth, the M_{FE}/W ratio is plotted against the lip size to flange width ratio (d/b) and presented in Figure 4.11. Hence Figure 4.11 includes 14 graphs, 1 for each nominal section depth considered and each of the 2 material properties assumed (i.e. EPP and R-O). The lip size to flange width ratio for which a peak of the M_{FE}/W ratio occurs corresponds to the optimal lip size to flange width ratio for the studied sections. As expected, all models assuming an elastic perfectly plastic (EPP) material response reach higher moment resistances compared to identical sections with a rounded material response, as they maintain their stiffness until the yield strength is reached, whilst employing a Ramberg-Osgood (R-O) type of response leads to loss of stiffness at lower stresses and hence cross-sectional instabilities occur earlier. In all cases considered herein the difference in terms of moment resistance between EPP and R-O is less than between 1% and 3% for the

geometrically identical sections with the higher end of the range corresponding to less slender sections. For the shallowest of the sections considered (i.e. Z146), increased efficiency can be achieved by increasing the lip size to flange width ratio, since no maximum can be observed in Figure 4.11(a) and (b). In all other cases, as shown in Figure 4.11 a clearly defined maximum can be observed for the thinner and most of the thickest sections, which corresponds to either the current lip size of 20 mm or to larger lip sizes. In general, the optimal lip size to flange width ratio increases with increasing section thickness as can be clearly seen in Figure 4.11 where the maximum of the M_{FE}/W ratio shifts to the right for thicker sections of the same depth. Hence increased efficiency can be achieved, if the lip size for the same nominal section depth is changed according to the section thickness, however this would be outside current practice and potentially highly impractical.

For most of sections, smaller lip size to flange width ratios (i.e. d/b ≤ 0.28) lead to less efficient cross-sections as their mean M_{FE}/W ratios can be up to 8% lower than that exhibited by the current lip size to flange width ratio where lip size equal to 20 mm. For Z176 sections, the current lip size to flange width ratio (d/b = 0.32) is recommended as either increasing or decreasing d/b ratio reduces the efficiency of the cross-section. Also on this basis, the recommended d/b ratio for Z206 and Z226 sections is 0.38. Furthermore, d/b ratio of 0.38, 0.46 and 0.54 were found to provide the cross-sections Z246 and Z266 with very similar levels of efficiency being 0.46 the optimal and therefore the recommended one. The optimal lip size to flange width ratio for Z307 appear to be 0.47 since increasing the d/b ratio beyond 0.47 mm has no benefit with the exception of Z30730 where d/b ratio of 0.6 shows highest efficiency. Building on the ease of manufacture, however, a single d/b ratio of 0.47 is recommended for all the Z307 range.

(a)

(b)

(c)

(d)

(e)

(f)

(g)

(h)

(i)

(j)

(k)

(l)

Z307 (R-O)

(m)

Z307 (EPP)
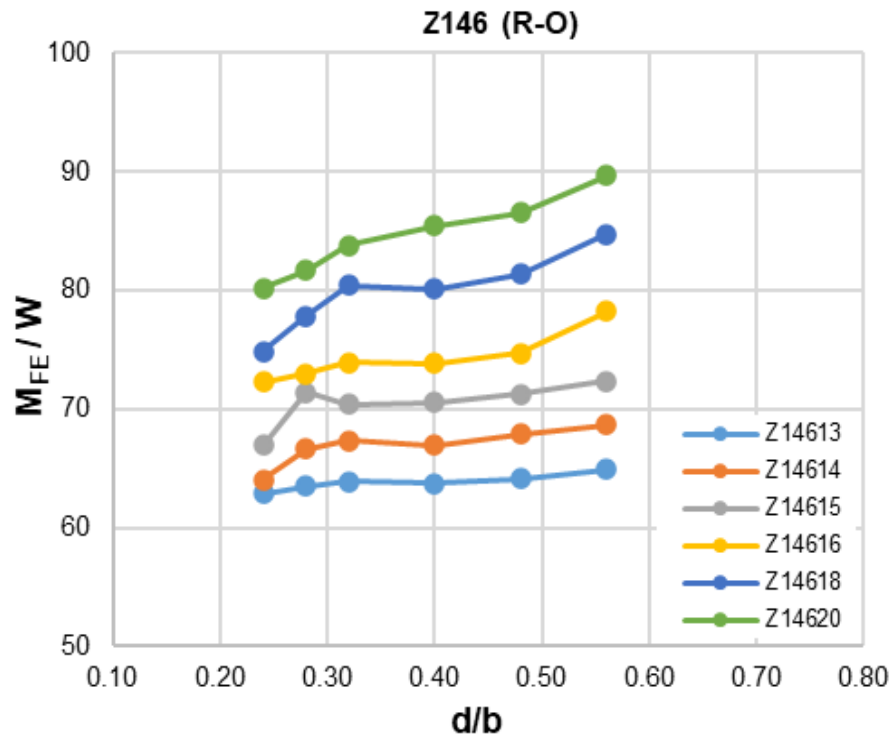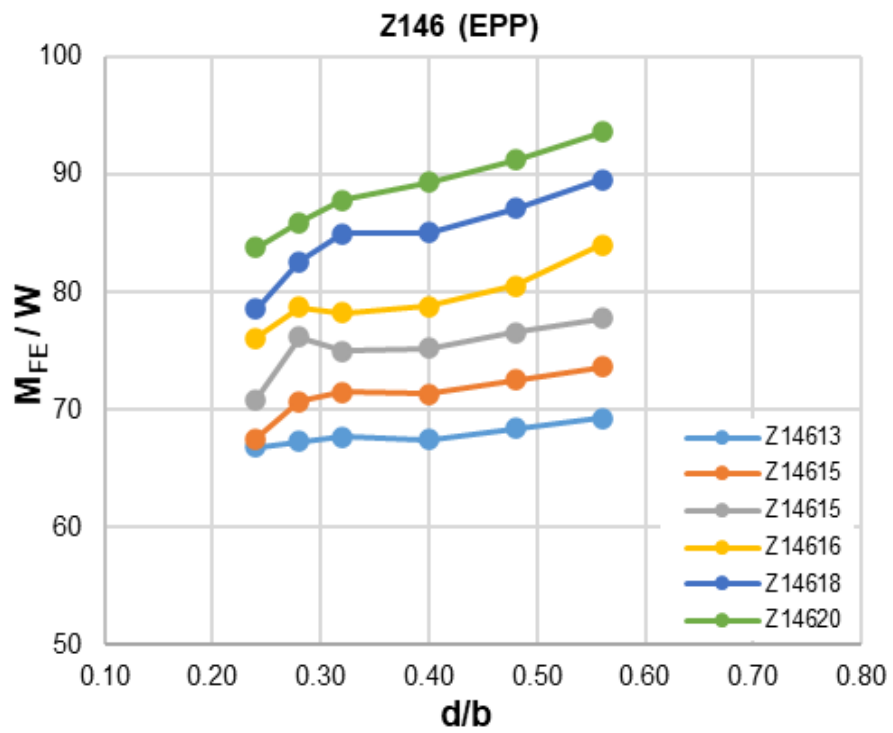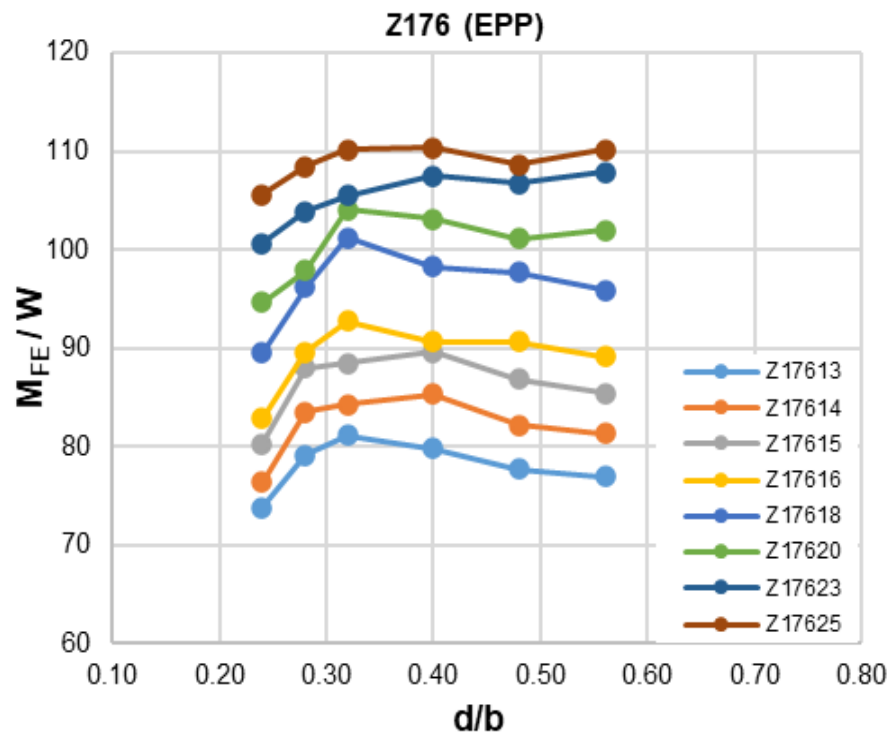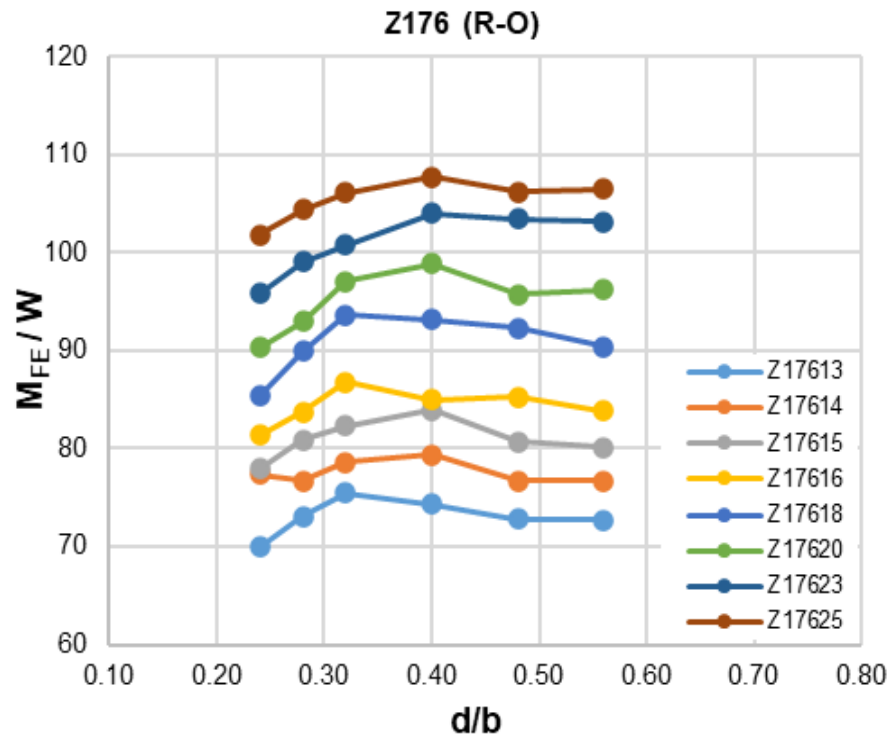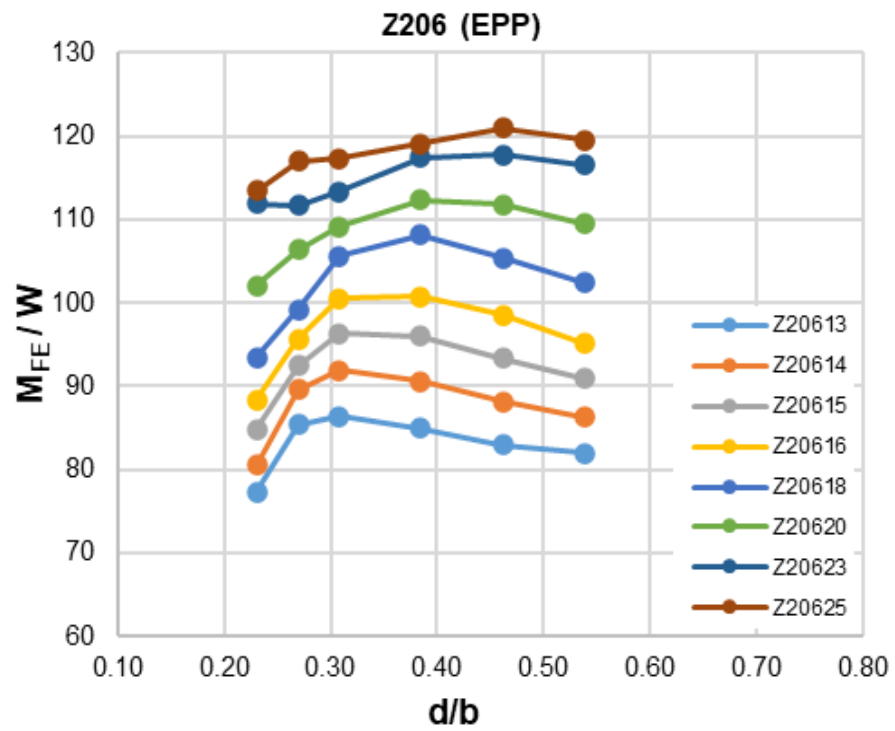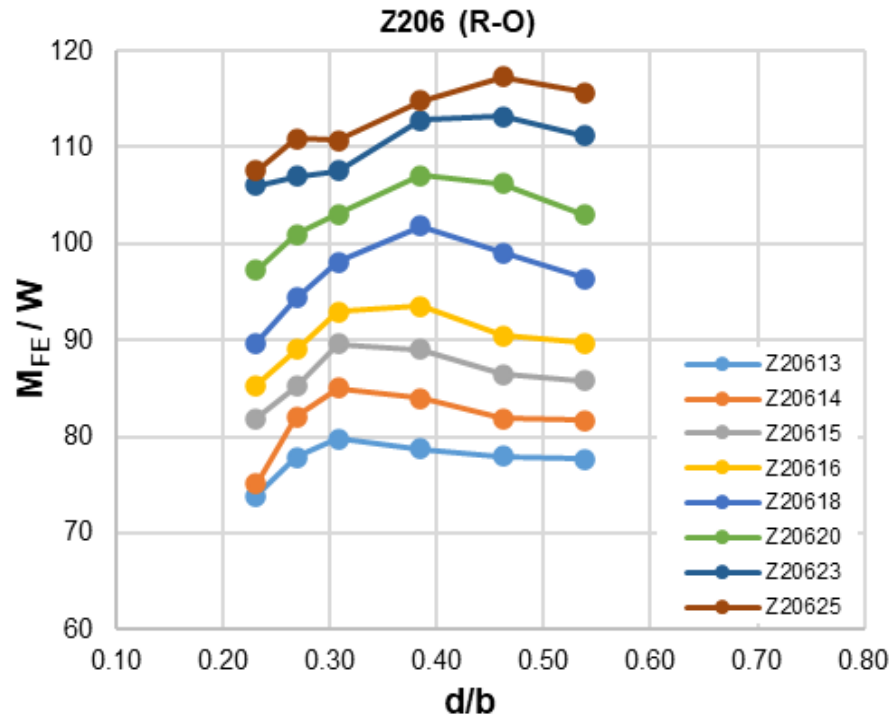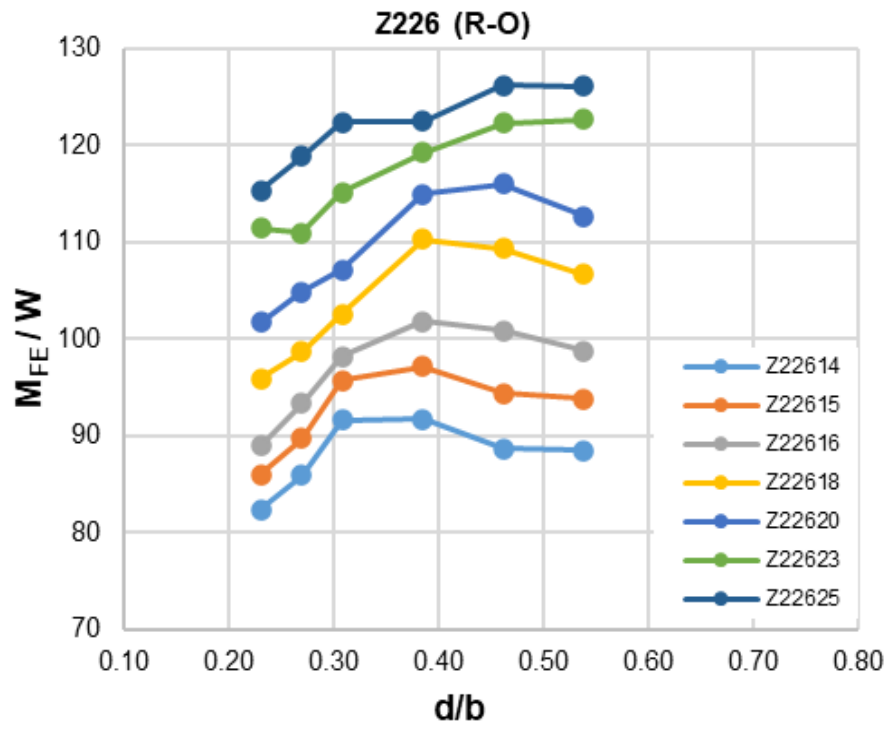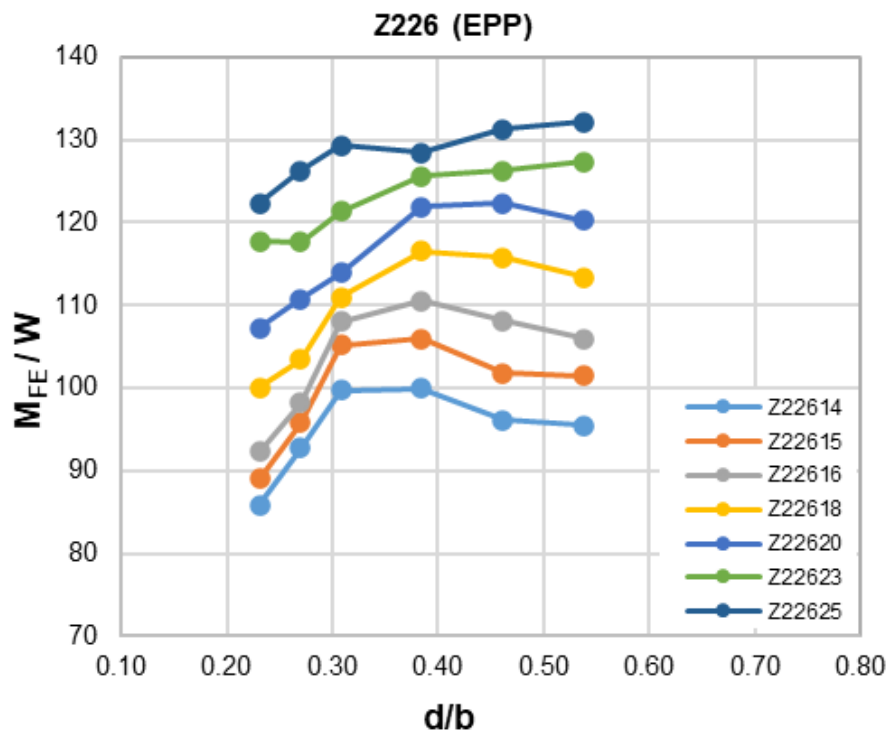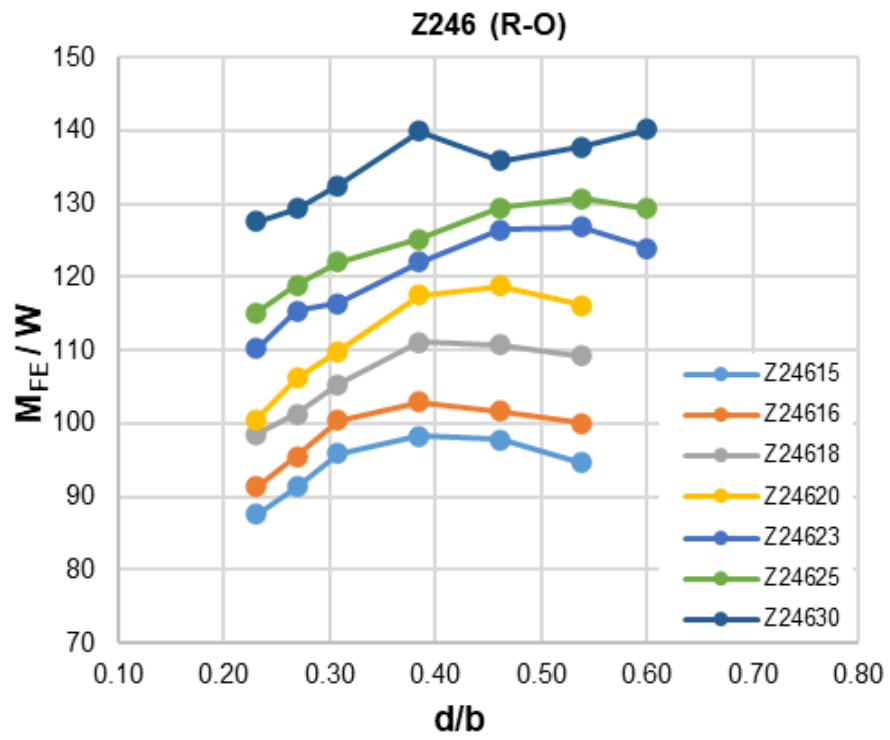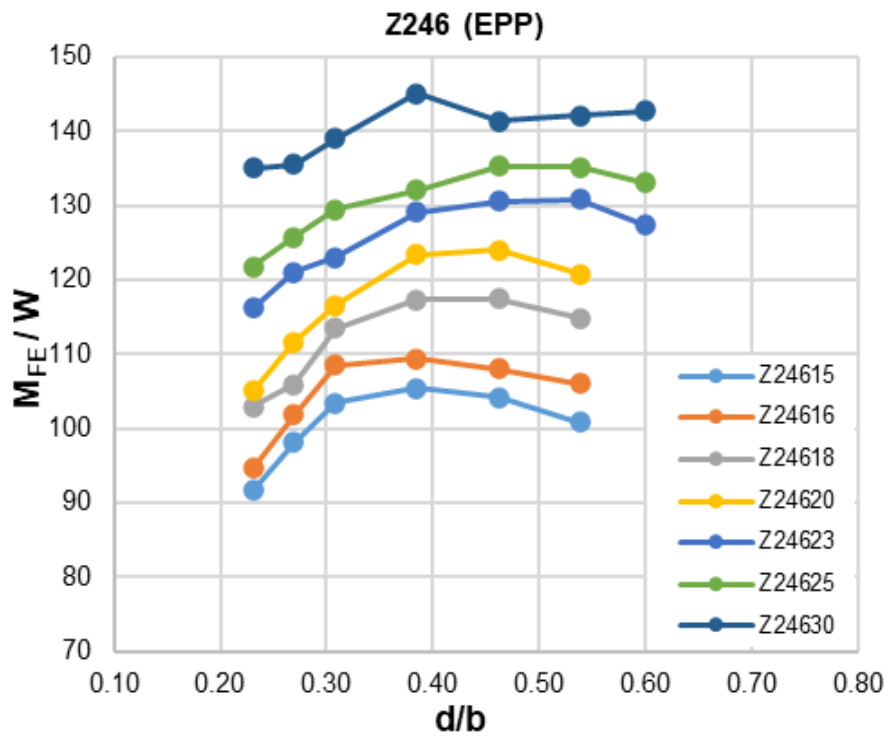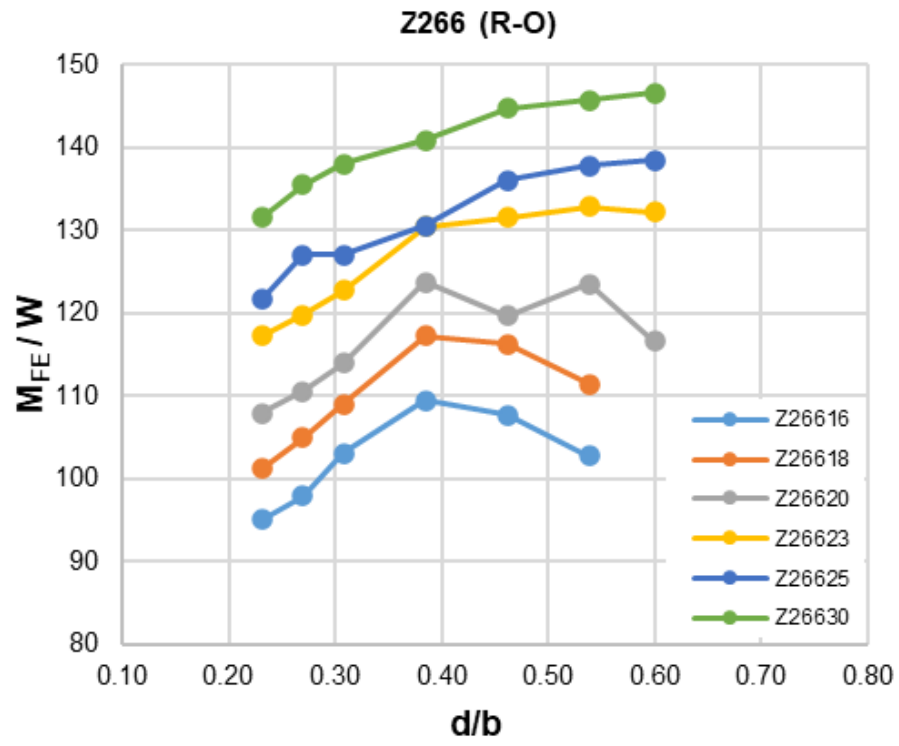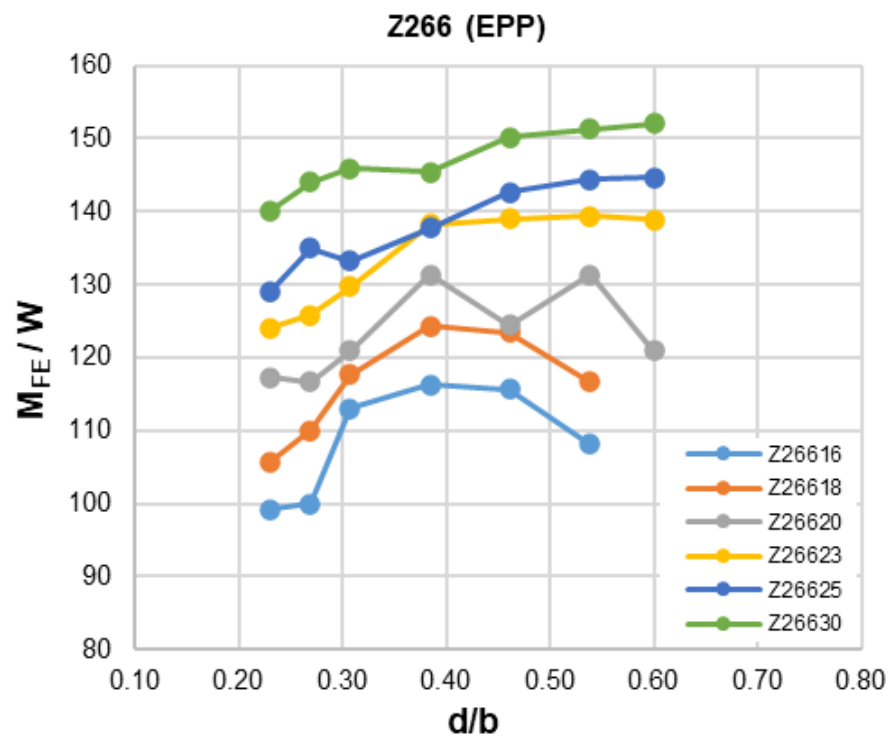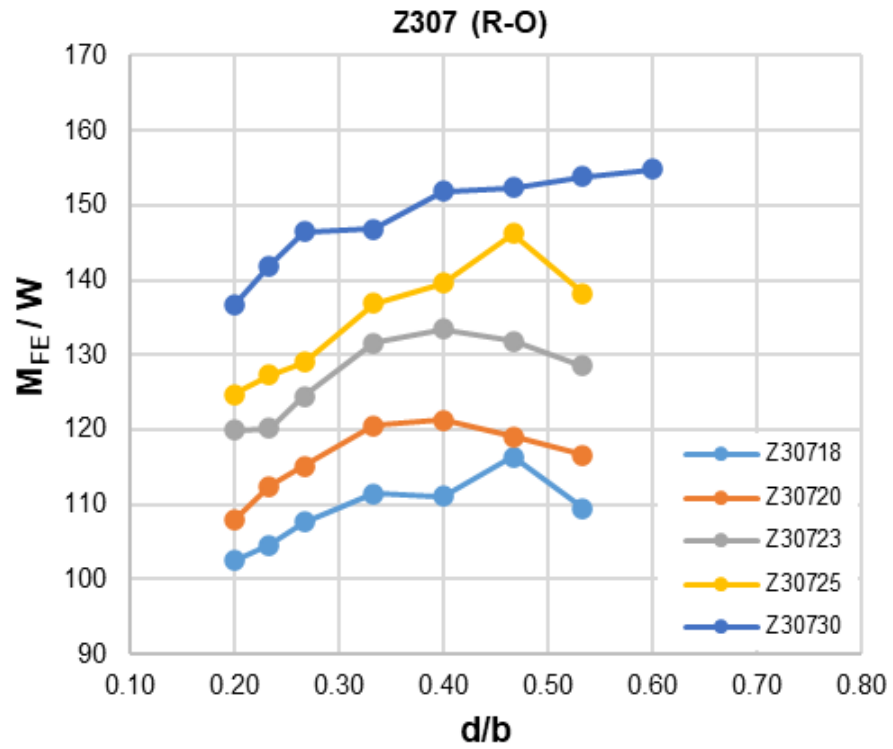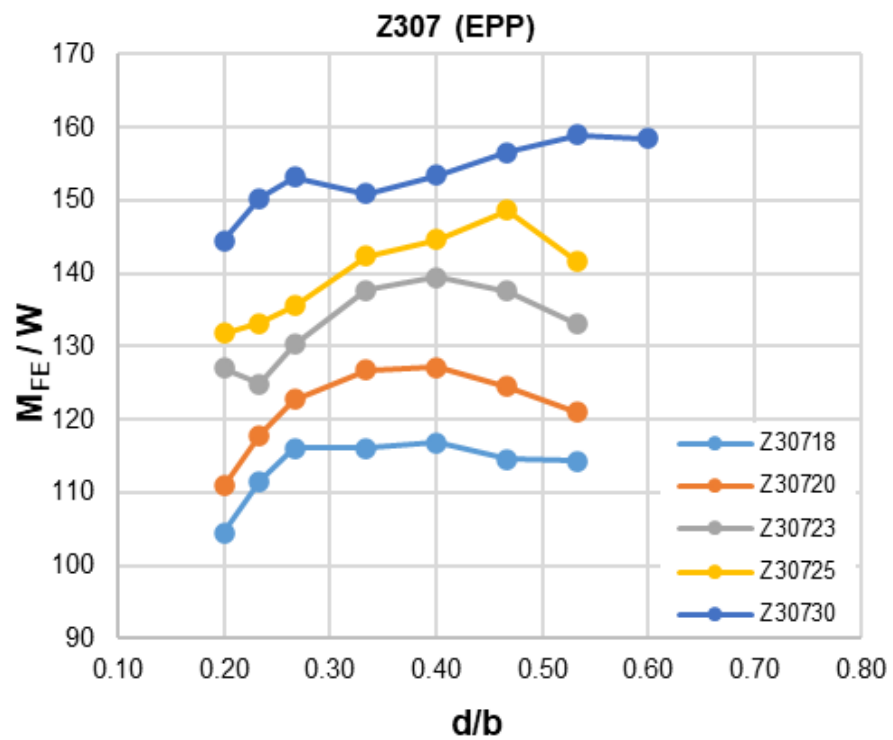
(n)

Figure 4.11 Effect of lip size to flange width ratio on moment to weight ratio.

4.6 Assessment of design provisions

Finally, the performance of the design provisions for bending and local buckling design given in the parts of the European code EN 1993-1-3 and the EN 1993-1-5 (labelled as EC3) (CEN, 2006a, CEN, 2006b) as well as the DSM (AISI, 2016) method from the American standard AISI are assessed. To facilitate direct comparison between the two design methods which incorporate different approaches to reliability and assume different variations for material strength and cross-section dimensions, all safety factors were set to unity. Since both design codes specify design rules applicable throughout the full slenderness range, the comparison includes all results regardless of their slenderness. Furthermore, in the Eurocode 3 design method, local and distortional buckling are treated together, hence there is no way to separately assess the accuracy of the Eurocode 3 design provisions for local and distortional buckling. The predicted moment capacities M_{pred} determined by both design approaches are compared with the moment capacities obtained from the FE analysis M_{FE}. The comparison is shown in Table 4.7 in terms of the average value of the M_{pred}/M_{FE} ratio of the various cross-sectional thickness taken into consideration within each cross-section range whilst highlighting the material type. A graphical representation is also provided in Figure 4.12 where the M_{pred}/M_{FE} ratio is plotted against the non-dimensional slenderness for distortional buckling λ_d determined as given by Equation 4.7, where σ_y is the material yield strength (or equivalent 0.2% proof strength for R-O material) and σ_{crd} is the distortional buckling critical strength which has been determined with the CUFSM (Li and Schafer, 2010).

$$\lambda_d = (\sigma_y/\sigma_{crd})^{0.5} \tag{4.7}$$

Overall, both design approaches are observed to be safe though the EC3 predictions are overly conservative underestimating the cross-sectional bending capacity by 10% for the R-O material and raising the level of conservativeness up to 15% when material strain hardening is not considered (i.e. EPP material). The EC3 predictions also show a reasonable scatter with COV values of 6 and 7% for the RO and the EPP material, respectively. In comparison, the DSM reduces the conservatism by 5% with less scattered predictions and therefore is deemed more efficient and reliable than EC3 for all the geometric configurations considered and regardless of material model. The same observations are depicted in Figure 4.12 where it can also be seen that for λ_d values less than 0.9, both design approaches yield results of very similar accuracy but the EC3 approach appears to be less accurate with increasing λ_d, whereas the DSM appears equally consistent and accurate throughout the slenderness range considered.

Table 4.7 Mean values of M_{pred}/M_{FE} ratio for Eurocode 3 (EC3) and the DSM.

Section	R-O		EPP	
	EC3	DSM	EC3	DSM
Z146	0.90	0.97	0.84	0.92
Z176	0.88	0.96	0.84	0.90
Z206	0.88	0.96	0.83	0.90
Z226	0.88	0.94	0.82	0.88
Z246	0.90	0.94	0.86	0.89
Z266	0.92	0.93	0.87	0.88
Z307	0.93	0.96	0.89	0.92
Overall mean	0.90	0.95	0.85	0.90
COV	0.060	0.040	0.070	0.039
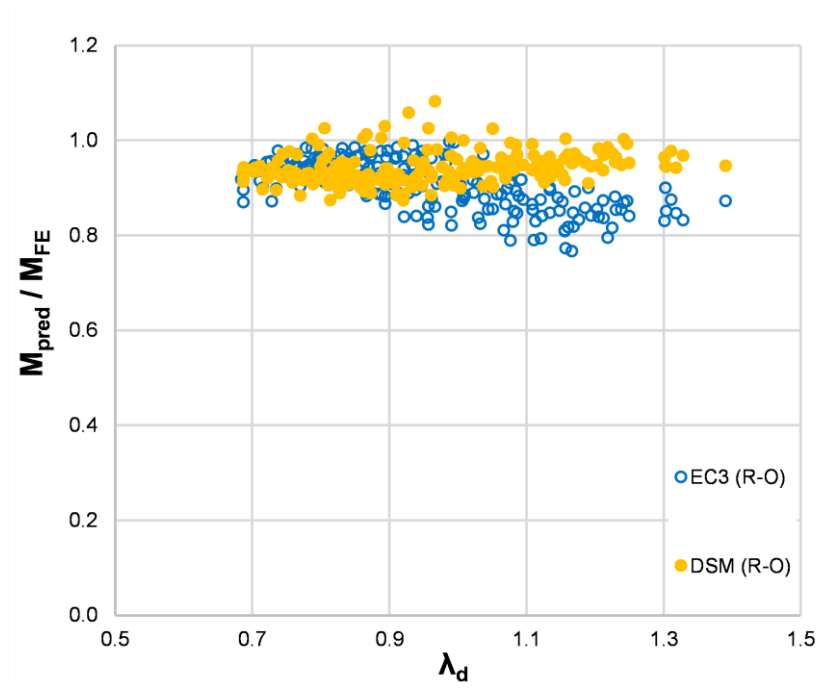
(a)

(b)

Figure 4.12 Comparison between the Eurocode 3 and the DSM(a) R-O material and (b) EPP material.

4.7 Summary

The development of an FE model for the simulation of Z-section purlins failing by local and /or distortional buckling has been reported in this study. Particular attention was paid to the modelling strategy for considering the effect of structural details such as angle struts and cladding on the structural response of the purlins, whilst a systematic study was carried out to study the effect of initial geometric imperfections and select the most suitable amplitudes and combinations thereof. Upon validation of the results, a parametric study was conducted to study the effect of the lip size to flange ratio on the flexural resistance of the studied sections. It was determined that all sections, would be less efficient if their current d/b ratio was decreased, whilst some of them would benefit from an increase of the current d/b ratio. The recommendations offer on average material savings of about 6% for the deeper sections and 4% for shallow sections, thus increasing the efficiency of the manufactured purlins. Finally, all generated numerical results were utilized to assess the accuracy of Eurocode 3 (CEN, 2006a, CEN, 2006b) and DSM (AISI, 2016) design predictions. In all cases, the Direct Strength Method leads to a moderate increase in the predicted strength compared to the European design approach, whilst the scatter of the predictions also decreases.

Chapter 5: Experimental tests on cold-formed steel sigma sections subjected to interior one flange loading

5.1 Introduction

This Chapter reports a series of experiments on sigma purlins under the interior-one-flange (IOF) loading condition. Two different section geometries and three different bearing plate widths are examined. The expected failure mode is web crippling since the minimum distance specified in AISI S100-16 was selected which minimising the impact of the bending moment on the web crippling strength of the tested specimens. The experimental results are utilized in chapter 6 to develop numerical model and extend a slenderness-based design approach previously developed for channel sections and hat sections (Duarte and Silvestre, 2013, Bock and Real, 2014) to the design of sigma sections subjected to IOF.

5.2 Experimental investigation

5.2.1 Specimens

A series of tests were performed on sigma purlins subjected to a concentrated load parallel to their web. The tested specimens are cold- formed and have a nominal yield strength of 450 N/mm^2. Tensile coupon tests on flat coupons extracted from the web of the sections were conducted by the manufacturer and the obtained key material properties, including Young's modulus, yield strength, 1% proof strength, ultimate tensile stress and strain at fracture are reported in Table 5.1, where it can be observed that the actual yield strength is very close to the nominal one. Both material coupons exhibited a well-defined yield point followed by mild strain-hardening until the attainment of the ultimate tensile stress as shown in Figure 5.1

Table 5.1 Material properties from tensile coupon tests.

t (mm)	E (N/mm²)	f_y (N/mm²)	$f_{1.0}$ (N/mm²)	f_u (N/mm²)	ε_f (%)
1.2	193000	447	470	480	14.7
2.47	206000	461	470	517	24.0

The minimum required lengths of the tested specimens were determined according to the requirements of the American Specification for cold-formed steel structures AISI S100-16 (AISI, 2016). which specify a minimum distance between the end of the bearing plate and the support equal to 1.5 times the overall depth of the web for tests corresponding to the IOF loading case. Since IOF will always be accompanied by a coexisting bending moment, the minimum distance specified in AISI S100-16 was selected to minimise the effect of the bending moment on the web crippling strength of the tested specimens. An overhang of 75 mm was provided beyond the ends on either side of the specimen.
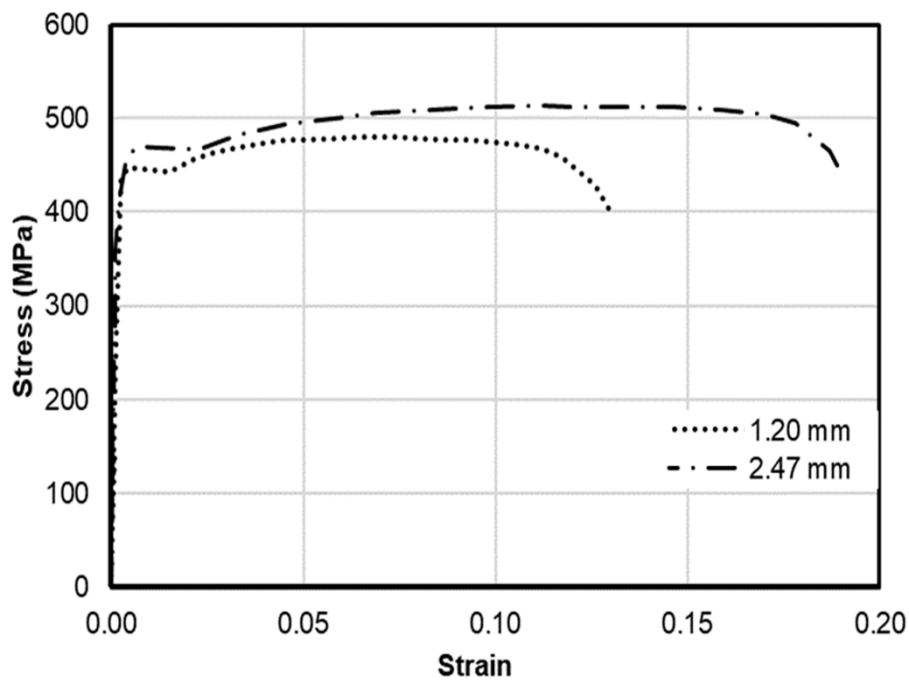
Figure 5.1 Stress strain curves of material coupons.

Two different section geometries were considered in the experimental studies. The chosen sections have nominal total web depths of 225 and 265 mm, and nominal thicknesses of 1.2 and 2.5 respectively, thus resulting in two nominal web slenderness (total web depth/thickness) values 106 and 188. For each cross-section three different bearing plate widths (N) namely, 50 mm, 75 mm and 100 mm were employed to examine the effect of bearing plate width on the web crippling strength. Prior to testing, measurements of the geometry of each specimen were taken at three locations along their length using a digital vernier caliper for the flat parts of the sections and a radius gauge for the corners; the results were averaged to obtain representative values. In Table 5.2, the measured cross-sectional dimensions of the cold-formed steel lipped sigma sections considered in the tests are reported, where t is the thickness, h is the total web depth, h_1 is the outer web depth, h_2 is the middle web depth, d is lip depth, r_1 is the internal root radius at the flange-web and flange-lip junctions and r_2 the internal root radius at the outer web-middle web junctions. The specimens were labelled according to their nominal cross-sectional dimensions and employed bearing plate width, e.g. specimen "22512-50" corresponds to a nominal total web depth of 225 mm, a nominal thickness of 1.2 mm, and the width of bearing plate of 50 mm. Figure 5.2 shows the definition of the symbols used to define cross-sectional dimensions.

Table 5.2 Measured geometric dimensions of tested specimens.

Specimen	h (mm)	b (mm)	h_1 (mm)	h_2 (mm)	t (mm)	d (mm)	r_1 (mm)	r_2 (mm)
22512-50	227.1	61.9	51.6	121.1	1.19	19.01	4.5	5.5
22512-75	226.8	62.3	51.1	121.8	1.20	19.07	4.5	5.5
22512-100	227	61.8	51.6	121	1.20	18.90	4	5
26525-50	265.3	63.6	64.3	133.9	2.49	20.31	4	5
26525-75	265.4	63.6	64.8	133	2.47	20.28	4	5
26525-100	265.4	63.6	64.8	133	2.47	20.28	4	5
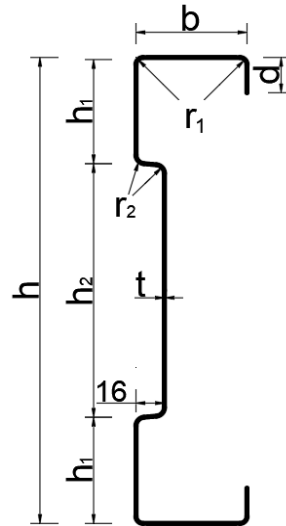
Figure 5.2 Cross-section geometry and symbols.

5.2.2 Setup and instrumentation

The sigma sections were tested under the interior-one-flange (IOF) loading condition specified in AISI S100-16 as shown in Figure 5.3a. As shown in Figure 5.3b, angle cleats bolted to the specimen were used at the support locations in accordance with current practice to prevent failure of the end cross-sections. The angle cleats were also bolted to a bearing plate which was resting on half rollers to allow free rotation of the ends in the plane of loading and achieve pin ended conditions. Loading was

applied on the top flange at mid-span through a bearing plate that was loaded by a hydraulic actuator. A load cell positioned such that its centroid coincided with the centroid of the actuator and with the web flange to web junction of the specimen was positioned between the actuator and the bearing plate. Since the only available degree of freedom of the actuator was the vertical displacement and due to the continuous contact of the actuator with the load cell and of the load cell with the bearing plate, all rotations of the bearing plate were effectively restrained. The width of the bearing plate was varied as part of the experimental investigation.

(a)
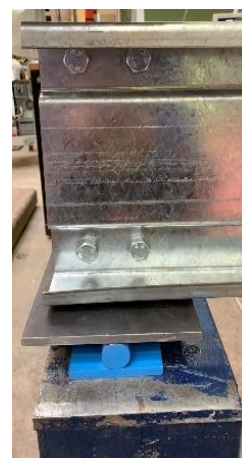
(b)

Figure 5.3 Web crippling test set up.

All test specimens were first loaded up to 2 KN and kept for 1 minute to attain a complete contact between the actuator and the bearing plate, and to check that everything was working as expected. Afterwards, the load was continuously applied until the ultimate load reached and specimens failed. The employed loading rate was 1.6 mm/min.

The employed instrumentation included a load cell to measure the applied force, which was positioned between the bearing plate and the hydraulic actuator, and three linear vertical displacement transducers (LVDTs), which were used to measure the vertical displacements at three points along the depth of the specimens' mid-section. These three points were the top flange $LVDT_1$, the bottom flange $LVDT_2$ and the bottom of the upper outer web $LVDT_3$ (i.e. the upper horizontal web folding). The utilisation of several LVDTs along the depth of the section allowed the quantification of the web-crippling deformation of the upper and middle web and thus the identification of distinct failure modes. To determine the web-crippling deformation of the upper outer web, the readings from $LVDT_3$ were subtracted from the readings from $LVDT_1$, while the web crippling deformation of middle web was determined subtracting the $LVDT_2$ readings from the readings from $LVDT_3$. All instrumentation was connected to a data acquisition system that logged data every second.

5.2.3 Test Results

The experimentally obtained ultimate load for all tests is reported in Table 5.3 together with the observed failure mode for each tested specimen. As expected, all specimens failed by web crippling, albeit the corresponding deformation patterns differed. For the more slender sections, web crippling deformations were contained only within the

upper web and the top part of the middle web, whilst for the thicker sections, deformations were spread throughout the whole upper and middle web with exception of specimen 26525-50 where web crippling occurred only within the upper web, as illustrated in Figures 5.4-5.6. During the test, the upper outer web deformation of the thinner sections continuously increased until the maximum capacity was reached, whilst for the thicker sections the upper outer web crippled initially and twisted thereafter as shown in Figure 5.5 (b). Following the distinction between yield-arc mechanism and rolling mechanism discussed in (Bakker and Stark, 1994), all slender (i.e. 1.2 mm thick) sections exhibited a rolling mechanism, as can be seen in Figure 5.4, where the flange can be observed to remain horizontal as the corner radius rolls down through the web. All thick (2.5 mm thick) sections developed a mixture of a yield arc mechanism followed by a rolling mechanism, as can be clearly observed in Figure 5.5.

Table 5.3 Summary of experimental results.

Specimen	$R_{w,Exp}$ (kN)	Failure mode
22512-50	9.47	Web crippling of the upper web and the top part of the middle web
22512-75	9.20	Web crippling of the upper web and the top part of the middle web
22512-100	9.01	Web crippling of the upper web and the top part of the middle web
26525-50	30.49	Web crippling of the upper web only
26525-75	33.87	Web crippling of the upper and whole middle web followed by twisting of the upper web
26525-100	36.00	Web crippling of the upper and whole middle web followed by twisting of the upper web
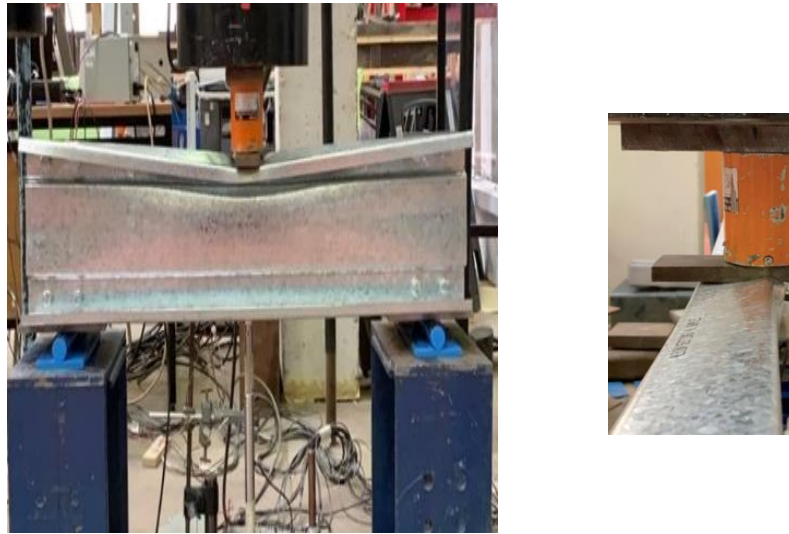
Figure 5.4 Failure mode of specimen 22512-50

(a)
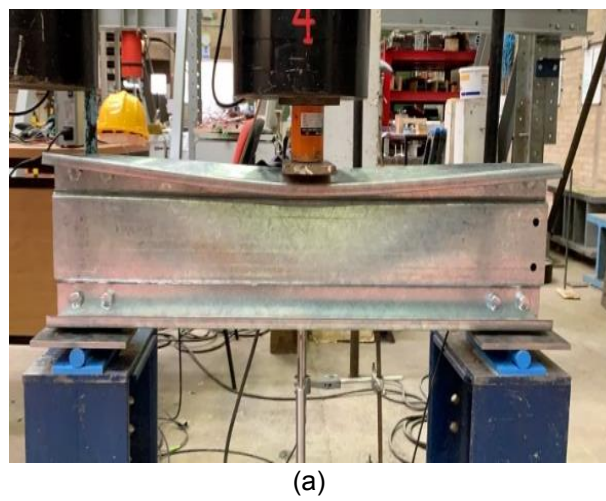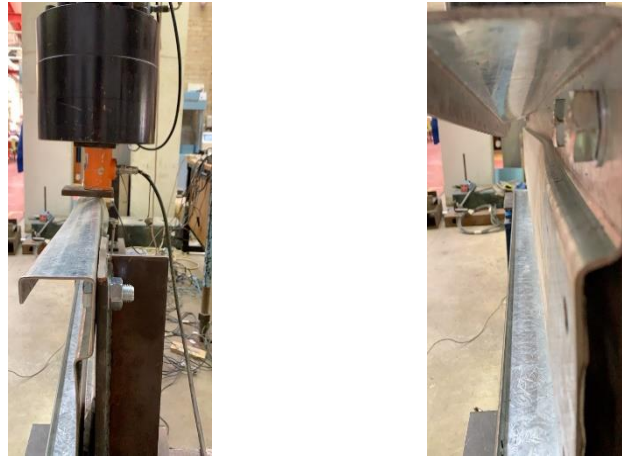
(b)

Figure 5.5 Web crippling at the whole upper and middle web (a) followed by upper web twist (b) (26525-100).

Figure 5.6 Web crippling of the upper web of specimen 26525-50.

The applied transverse load is plotted against the three displacements measured by the three LVDTs as shown in Figure 5.7 where the top, mid and bottom deflection corresponds to the readings from $LVDT_1$, $LVDT_3$ and $LVDT_2$, respectively. In this figure It can be seen that both tested specimens display similar response where the top and middle deformations are large in comparison with bottom one. The two distinct failure modes observed for the tested sections are also associated with qualitatively different

load deformation responses. The more slender sections display an initially linear response followed by a secondary linear region of reduced stiffness, within which the deformations of the top part of the section increase faster than those of the upper part of the middle web thus indicating that crippling deformations are primarily combined within the upper web. The gradual transition from the initial to the secondary linear part of the response is accompanied by significant plastic deformations and the stable nature of this secondary curve demonstrates the ability of the section to redistribute the stresses internally and accommodate increased load. This behaviour is consistent with a rolling mechanism (Bakker and Stark, 1994). On the contrary, the stockier sections display a linear response which gradually degrades until the maximum load corresponding to web crippling of the upper web is reached, whereupon the load bearing capacity is lost and the load decreases gradually. The gradual decrease in load is consistent with a section failing by a combination of a yield arc and a rolling mechanism, as pure yield arc type of failure results in a more abrupt loss of strength upon the attainment of the ultimate load, whilst, as previously discussed, a rolling mechanism results in a response with two distinct linear regions prior to the attainment of the ultimate load.
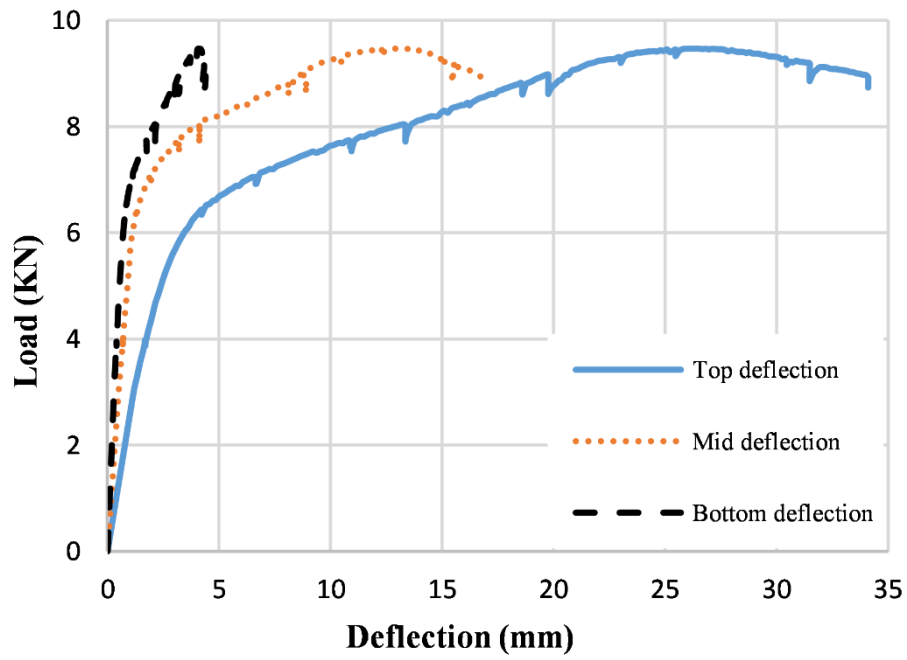
(a)
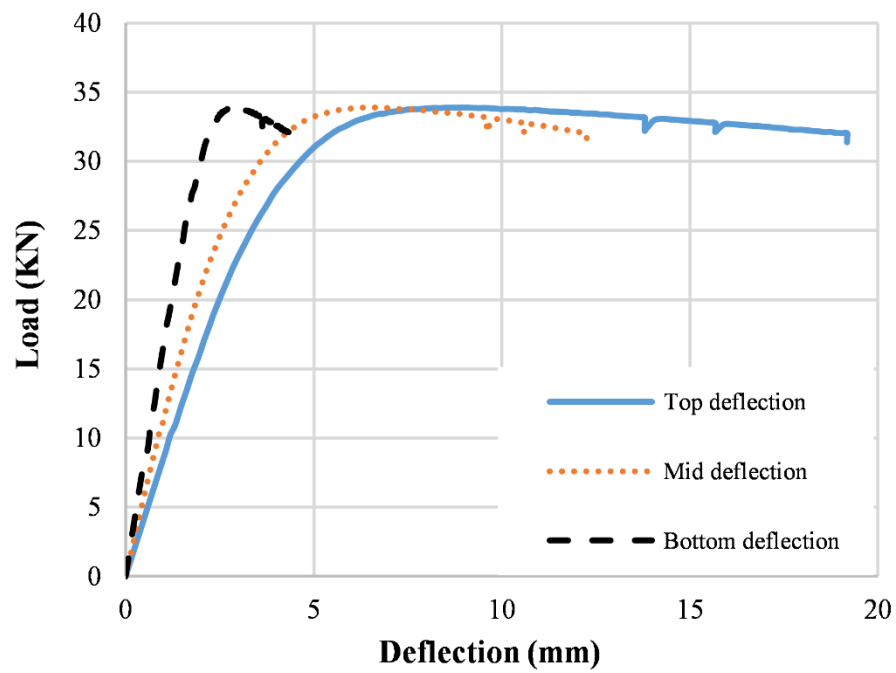
(b)

Figure 5.7 Load-deformation response of specimens (a)22512-50 and (b) 26525-75.

Employing wider bearing plates was expected to increase the resistance area under the load application, hence to lead to higher web crippling capacities as observed in the thicker sections. However, this was not the case in the thinner sections where slightly larger web crippling loads were obtained by the smallest bearing plate width. Similar results have been previously observed in (Sundararajah et al., 2018). This can be attributed to the variations of initial imperfection levels and experimental scatter; the numerical models displayed the expected response as discussed in Chapter 6.

5.3 Summary

In this study, six experimental tests on sigma sections subjected IOF loading were reported. It was found that the web crippling is the failure mode for all tested specimens, but the deformation patterns varied. For thinner sections, the rolling mechanism occurred, whereas for thicker sections a mixture of a yield arc mechanism and a rolling mechanism were developed. The obtained experimental results will be utilised in the following chapter (Chapter 6) to validate the developed numerical model and extend a slenderness-based design approach previously developed for channel sections and hat sections (Duarte and Silvestre, 2013, Bock and Real, 2014) to the design of sigma sections subjected to IOF

Chapter 6: Slenderness-based design for sigma sections subjected to interior one flange loading

6.1 Introduction

This chapter reports numerical study on sigma sections subjected to web crippling. To investigate further the effect of web geometry on the IOF web crippling strength of sigma sections, numerical models will be developed and validated against a total of 6 experimental results on sigma sections that failed in web crippling as reported in Chapter 5. Following successful replication of the experimental observations, a comprehensive parametric study will be performed, and several sigma sections covering a wide range of cross-sectional geometries and slenderness will be numerically modelled. By utilising the experimental and FE results, the north American specifications NAS S100-16 (AISI, 2016) will be assessed and design recommendations will be offered. Finally, a slenderness-based design approach previously developed by Duarte and Silvestre (2013) and (Bock and Real, 2014) for the web crippling design of channel and hat sections respectively will be extended to sigma sections.

6.2 Modelling assumptions

A nonlinear static analysis was conducted to simulate the response of the specimens accounting for material and geometric nonlinearities as well as for the contact interaction between the specimen and the bearing plate. The curved corner of the cross-sections means that the load is applied eccentrically to web. Hence there was no need to perturb the idealized geometry to trigger web crippling as the magnitude of the initial geometric imperfections would have been significantly smaller than the 2nd order effect caused by the eccentric application of the load. Therefore, no initial geometric imperfections were incorporated in the numerical models. The employed

analysis type was general static and displacement control was utilized to apply the load and obtain the post-ultimate response.

The linear four-nodded shell element with reduced the integration S4R was used to discretise the midline dimensions of the tested cold-formed steel sigma sections, as determined from the measured geometry reported in Table 5.2. The SR4 element has been shown in past studies to give accurate results when modelling cold-formed sections subjected to web crippling (Zhou and Young, 2007a, Bock et al., 2013, Natário et al., 2014, Bock et al., 2015, Li and Young, 2017b, Li and Young, 2018). As in the tests, three bearing plate widths were employed to load each section and an analytical rigid plate was used to simulate them and facilitate the load application on the sections. In accordance with the material properties reported in Table 5.1, an elastic perfectly plastic material was assumed in the modelling with a Young's modulus E = 200 GPa, a Poisson's ratio v = 0.3 and a yield stress f_y = 450 MPa. As the material coupons exhibited a well-defined yield plateau and given the minimal strain-hardening observed, no hardening was assumed for the material.

Achieving a balance between accuracy and computational efficiency requires employing a suitable mesh size, usually determined via a mesh convergence study. An element size of 10 mm was used for all flat parts of the sigma sections except for the top lip of the section where two elements were used in all models. The geometry of the curved corner at the flange to upper web junction has a profound influence on the structural behaviour of sections subjected to IOF. With increasing loading, the loaded flange rotates and the line of contact between the bearing plate and the

specimen moves along the curved corner region towards the section's web. Furthermore, due to the progressive yielding of the integration points of the curve region, the yield lines also move along the curved region. Hence, due to the changing contact conditions between the specimen and the bearing plate and the movement of the yield lines over the curved corner region, a sufficiently fine mesh is required to discretise the curved corners. The appropriate mesh density in the corner regions was assessed through a separate mesh convergence study and the effect of adopting five different mesh size for the upper curved corner region at the flange to web junction was investigated. Figure 6.1 shows the obtained load deformation response for each of the element number variations considered in the corner region. Clearly significant oscillations of the load-deflection response are exhibited when a small number of elements is employed, because of the effect of the mesh density on the contact with the bearing plate. It can be clearly observed that when 3 elements are used to discretise the corner region, there are three local maxima in the load deflection curve, as extensive yielding of the corner region leads to a drop in strength until the adjacent corner element comes in contact with the plate, thus decreasing the eccentricity of the applied load and allowing higher loads to be carried. The more the employed elements, the smoother the load transfer from the plate to the web of the section and the more accurately the development of the yield lines is captured, hence the smaller the apparent oscillations in the load-deflection curve. It is recommended herein that the top corners should be discretised by at least 15 elements to obtain a smooth response and sufficiently accurate results. All other corners were discretised using 3 elements. A typical mesh utilised in this study is illustrated in Figure 6.2.
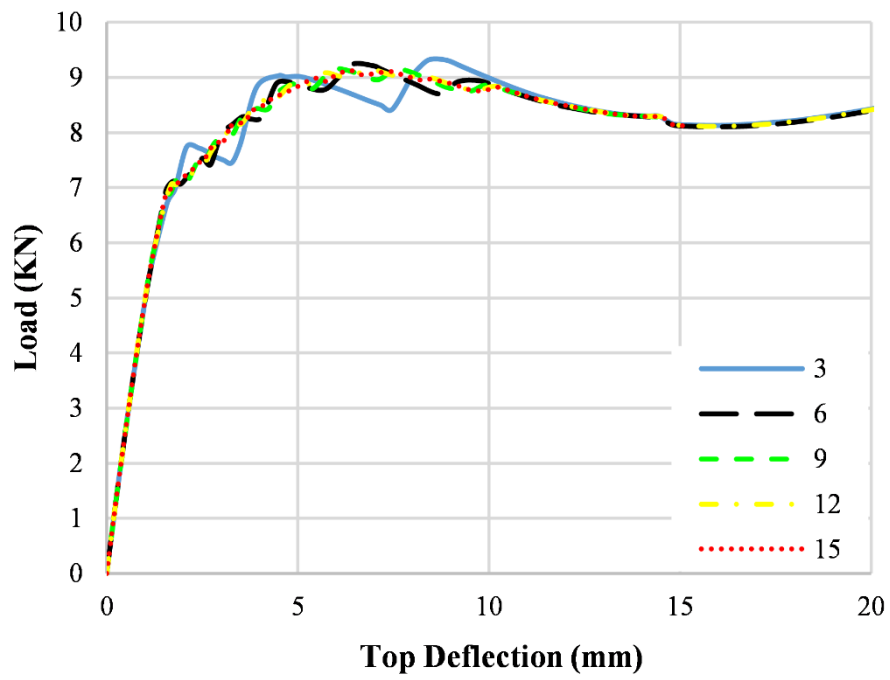
Figure 6.1 Effect of corner region discretisation on obtained response.
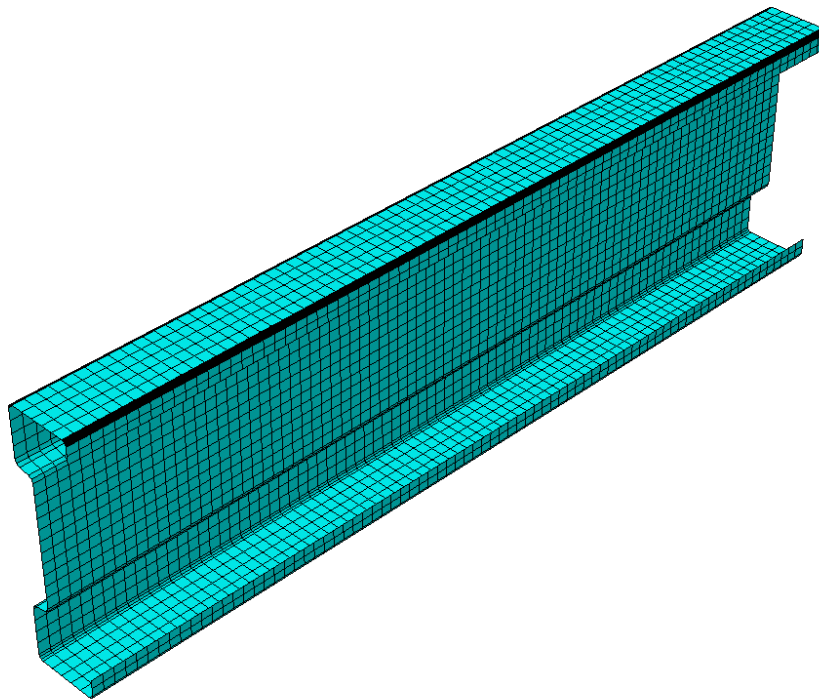
Figure 6.2 Employed mesh size.

An analytical rigid surface was used to simulate the bearing plate used in the tests and displacement control was used to load the model. The degrees of freedom of the analytical surface, defined at its reference point, were restrained except for the translation in the y-direction (i.e. parallel to the section web). To simulate the effect of the angle cleats and eliminate localised failure at the supports, kinematic coupling was utilised to tie the degrees of freedom along the web of the specimens at mid width of the angle cleats to the degrees of freedom of the constrained reference point to which boundary conditions were assigned as shown in Figure 6.3. It is noted that rotations about both y and z axes and translations in the y and x directions were restrained at both supports, whilst the translation along the specimen axis (z-axis) and the rotation about the x-axis (in the plane of loading) were free at both ends.

$Ux=Uz=UR_x=UR_y=UR_z=0$

$U_x=U_y=UR_y=UR_z=0$

$U_x=U_y=UR_y=UR_z=0$
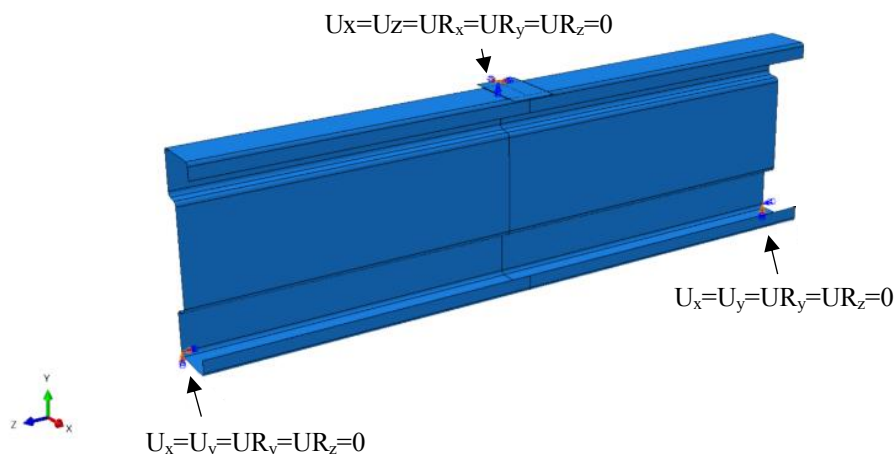
Figure 6.3 Applied boundary conditions at the reference points controlling the degrees of freedom of the end cross-sections and the loading plate.

The interaction between the sigma sections and bearing plates was simulated using contact pairs (surface-to-surface contact). The bottom surface of the bearing plates was defined as the master surface whilst, the top surface of the compression flange

of the specimen and corner elements along with the flange were assigned as the slave surface, as they employed a finer mesh. The corner regions were included in the slave contact surface because they experience significant deformations and do eventually come in contact with the bearing plate at high localised deformations. Hard contact was assumed in the normal behaviour and the friction penalty contact with a friction coefficient of 0.2 was employed for the tangential behaviour.

6.2.1 Validation

Table 5.4 reports the comparison between the web crippling capacities obtained from the numerical analysis and the experiments, whilst a typical comparison of experimental and numerical load-deflection response is shown in Figure 6.4. The numerical failure modes were in good agreement with the experimentally observed failure modes as shown in Figure 6.5. Overall, the numerical results show a reasonably good agreement with the experimental results with a mean $R_{w,Exp}$ / $R_{w,FE}$ ratio of 0.96 and a coefficient of variation (COV) of 0.08. From Table 6.1 it can be seen that larger differences between numerical and experimental results were observed for specimens 22512-100 and 26525-100. This is believed to be due to the use of wider plates. Wide plates can be less flat than narrower plates and moreover the contact with the specimens take place over a longer specimen length where geometric imperfections may be more pronounced. The inconsistency between the initial stiffness of the tests and the numerical models has been previously observed by other researchers (Kaitila, 2007, Natário et al., 2014, Bock and Real, 2014, Sundararajah et al., 2018, Janarthanan et al., 2019a, Janarthanan et al., 2019b) and is attributed to the sensitivity of the numerical model to initial imperfections and boundary conditions (Bock and

Real, 2014). Possible reasons for the observed discrepancy relate to the actual contact conditions between the loading plates and the specimen, which may differ from the perfect contact along the plate width assumed in the FE analysis. Furthermore, critical for the observed stiffness is the actual eccentricity of the load with respect to the loaded web, which in turn depends mainly on the radius of the flange to web junction. The radius of the specimens was measured using a radius gauge and the average of the recorded values was used, which might not be representative of the actual radius in the vicinity of load application. From the comparisons of the experimental and numerical results in terms of web crippling capacity, the failure mode and load-defection response, it can be concluded that the model is capable of replicating the main features of cold-formed steel lipped sigma sections behaviour failing by web crippling and is hence used in subsequent parametric studies.

Table 6.1 Comparison of the experimental and numerical web crippling loads.

Specimen	N (mm)	$R_{w,Exp}$ (KN)	$R_{w,FE}$ (KN)	$R_{w,Exp}/R_{w,FE}$
22512-50	50	9.47	9.13	1.04
22512-75	75	9.20	9.45	0.97
22512-100	100	9.01	10.84	0.83
26525-50	50	30.49	29.88	1.02
26525-75	75	33.87	35.21	0.96
26525-100	100	36.00	39.89	0.90
			Mean	0.96
			COV	0.08
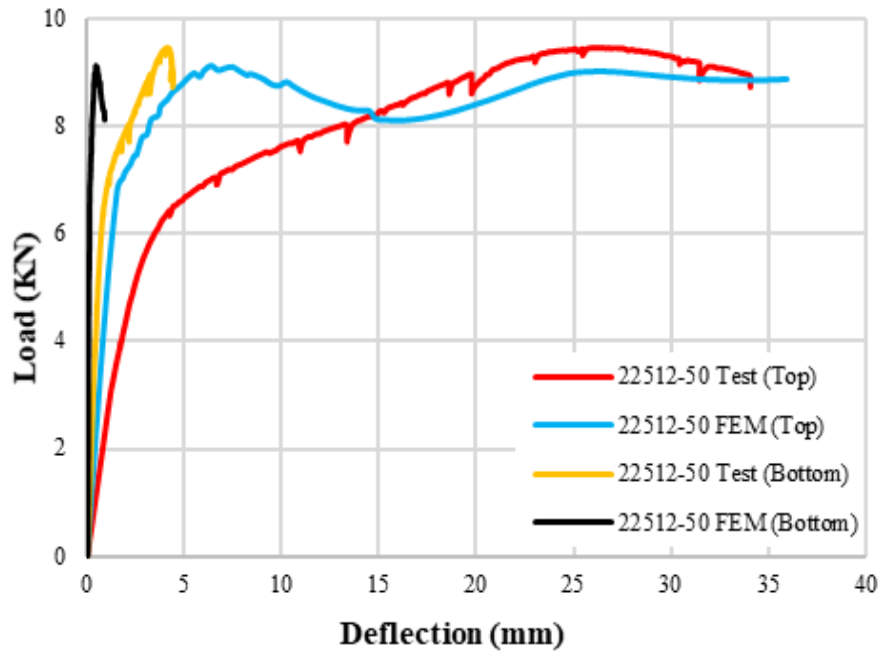
(a)
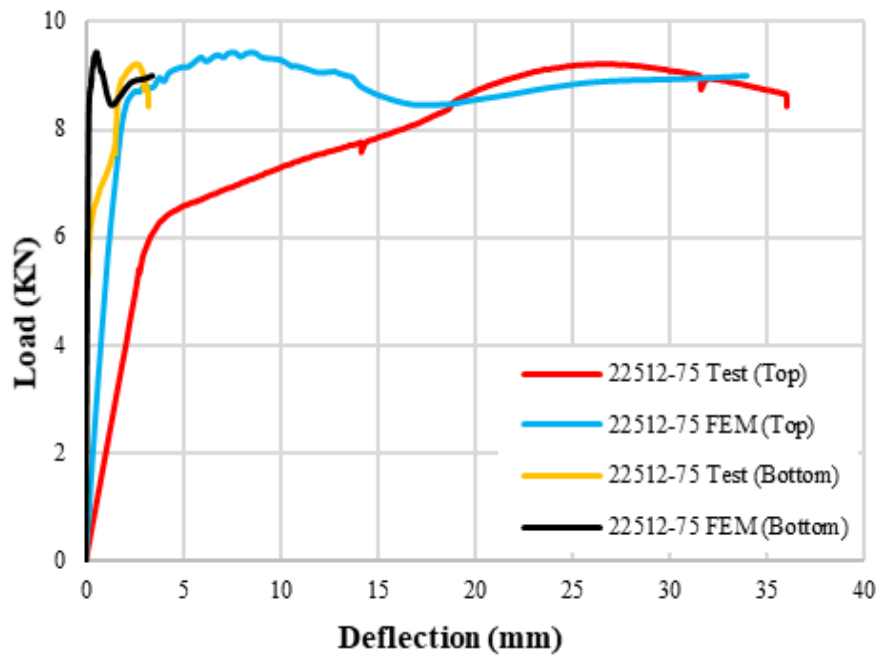
(b)

Figure 6.4 Load-deflection response for sigma section (a) 22512-50 and (b) 22512-75.
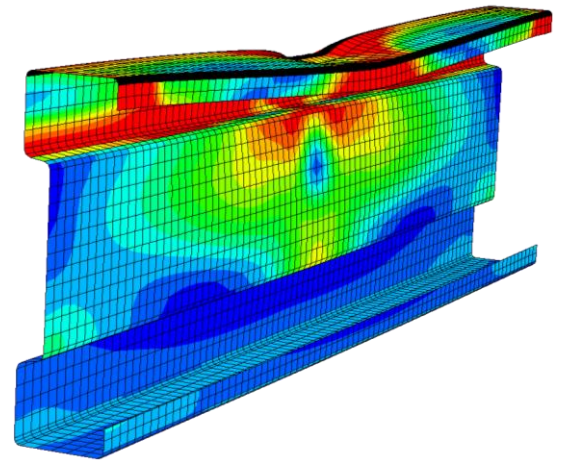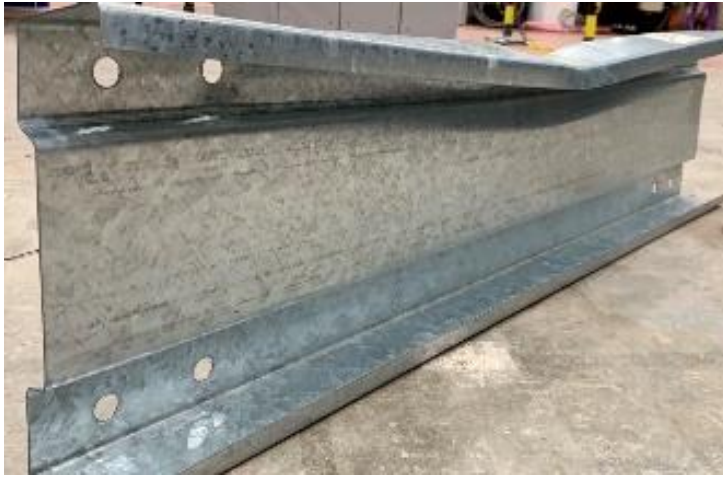
(a) 22512-75
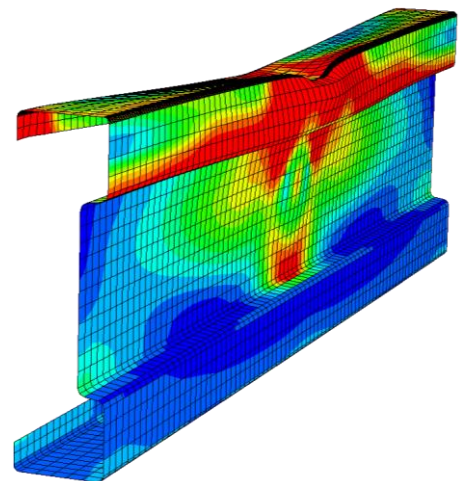
(b) 22512-50
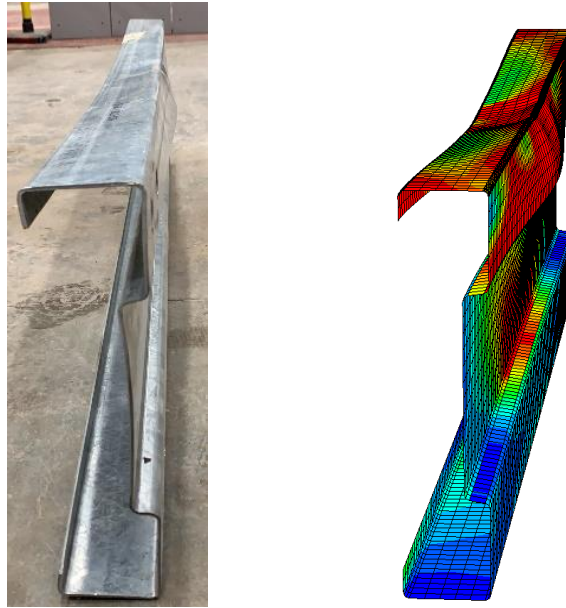
(c) 26525-100

Figure 6.5 Comparison of failure from experiments and numerical models.

6.3 Parametric study

6.3.1 Modelled geometries

Following successful replication of the experimental observations, a comprehensive parametric study was performed, and several sigma sections were numerically tested. The parametric study consisted of sixty-three sigma section geometries, having web depths ranged from 200 to 300 mm, the thickness ranged from 1.2 to 3 mm, and three middle to total web depth ratios (h_2/h): 0.4, 0.6 and 0.8. For all section, the lip depth (d), the internal root radius at the flange-web and flange-lip junctions (r_1) and the internal root radius at the outer web-middle web junctions (r_2) were fixed at 20 mm, 4 mm and 5 mm respectively. It should be highlighted that cross-section with middle to total web depth ratio of 0.6 represent existing sigma sections, whilst the other middle to total web depth ratios were considered to examine their influence in web crippling

behaviour and evaluate the applicability of the slenderness- based design approach to a wide range of cross-section geometries likely to be employed in the future. The cross-section dimensions for all sections are summarised in Table 6.2. Similar to the tests, three bearing plate widths: 50, 75 and 100 mm were employed for each cross-section. In the parametric study, the lengths of the specimens are determined according to the American Specification (AISI, 2016) as the minimum length required for IOF loading conditions. The material adopted in the validation was utilised in the parametric study with E=200 GPa, v=0.3 and f_y=450 MPa.

Table 6.2 Summary of section geometries employed in the parametric study.

Specime	h (mm)	b (mm)	h$_1$ (mm)	t (mm)	d (mm)	r$_1$ (mm)	r$_2$ (mm)	L (mm)
ASB200	200	62.5	20, 45, 60	1.2, 1.4, 1.6, 2, 2.5	20	4	5	700
ASB225	225	62.5	23, 45, 68	1.2, 1.4, 1.6, 2, 2.5	20	4	5	800
ASB240	240	62.5	24, 50, 72	1.5, 1.8, 2.3, 2.8	20	4	5	820
ASB265	265	62.5	27, 60, 80	1.5, 1.8, 2.3, 2.8	20	4	5	900
ASB300	300	75	30, 60, 90	1.8, 2.5, 3	20	4	5	1000

6.3.2 Analysis

Three types of analysis were conducted in this parametric study: (a) eigenvalue analysis to obtain the critical buckling load $R_{w,cr}$, (b) first-order plastic analysis considering elastic-perfectly plastic material and no geometrical nonlinearities to

obtain the plastic load $R_{w,pl}$ and (c) geometrically and materially nonlinear analysis to obtain the web crippling resistance R_w. The elastic critical buckling load and the plastic load are required to define the slenderness of the modelled sections, since, it has been shown (Duarte and Silvestre, 2013, Bock and Real, 2014), that there is a strong correlation between slenderness and web crippling resistance R_w. It has to be noted that the critical buckling load $R_{w,cr}$ and plastic load can only be obtained numerically $R_{w,pl}$ whilst, the web crippling load can be determined numerically and experimentally. All numerical results obtained from the three analyses are utilized hereafter to derive suitable predictive equations.

6.3.2.1 Elastic critical buckling $\mathbf{R_{w,cr}}$

From the eigenvalue analysis, the lowest elastic buckling load pertinent to web buckling was obtained as the critical buckling load of lipped sigma sections. Since contact interaction cannot be used in the eigenvalue elastic analysis in Abaqus, the interaction between the specimen and the bearing plate at midspan was simulated with kinematic coupling. All degrees of freedom of the nodes at the interface between the flat part of the flange closer to the web and bend radius along a width equals to the bearing plate width were constrained to a reference point as shown in Figure 6.6. This approach provided a good representation of the pertinent web crippling mode shape as shown in Figure 6.7. The modelling of the supports was not changed in the elastic buckling analysis.
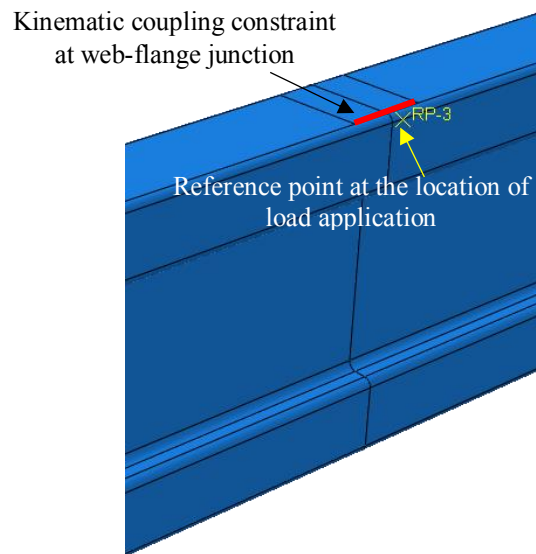
Figure 6.6 Detail of the employed load application strategy for the elastic critical buckling analysis.
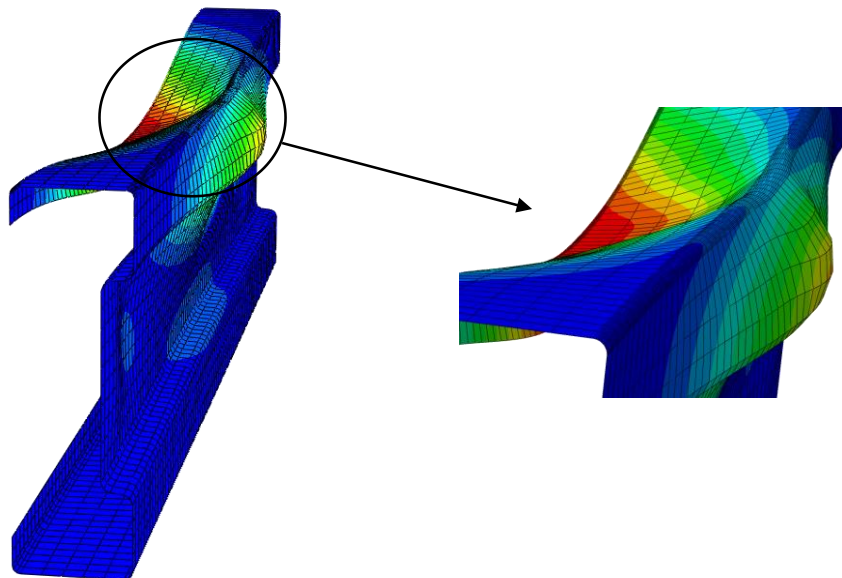
Figure 6.7 Buckling mode shape corresponding to the elastic critical buckling load for web crippling $R_{w,cr}$.

6.3.2.2 Plastic load $R_{w,pl}$

Apart from considering geometrical nonlinearities, all modelling assumptions adopted in previous validations were used in first-order plastic analysis to obtain the plastic buckling load. Determining the plastic load from the first-order plastic analysis was complex due to three reasons (Dos Santos et al., 2018): (i) the load-deflection curves sometimes dropped after obtaining unrealistically high deformations; (ii) on some occasions the numerical analysis terminated without achieving a maximum load; and (iii) the models may not reach a well-defined maximum and the load-deflection curves may keep increasing albeit with an ever-reducing slope. From the first order plastic analysis results, the latter problem was mostly observed, as depicted in Figure 6.8.

To overcome this problem and determine the plastic load $R_{w,pl}$ from the load-deformation response obtained numerically, a graphical method was used. Graphical methods are available in the literature such as the Southwell plot (Southwell, 1932), the modified Southwell plot (HORNE and MERCHANT, 1965) the convergence indicator plot (Doerich and Rotter, 2011). Research carried out by Dos Santos et al. (2018) concluded that all the above methods provide similar estimations for the plastic load with similar calculation efforts and derived a new simplified method based on the tangent stiffness plot which. Dos Santos et al. (2018) method was used herein to extract the plastic load $R_{w,pl}$ from the load-deformation response. This approach relies on the variation of tangent stiffness of a structural member obtained from the slope of the load-deformation response. The tangent stiffness Ki for each increment can be determined as the change of the applied load over the change in deflection. Following this approach, the plastic load is assumed to be reached when the tangent stiffness is equal to 1% of the initial stiffness. The plastic loads obtained by applying this technique

are assumed to be the plastic loads of the sections and are utilised subsequently to derive a design method for the determination of the strength of sigma sections subjected to IOF.
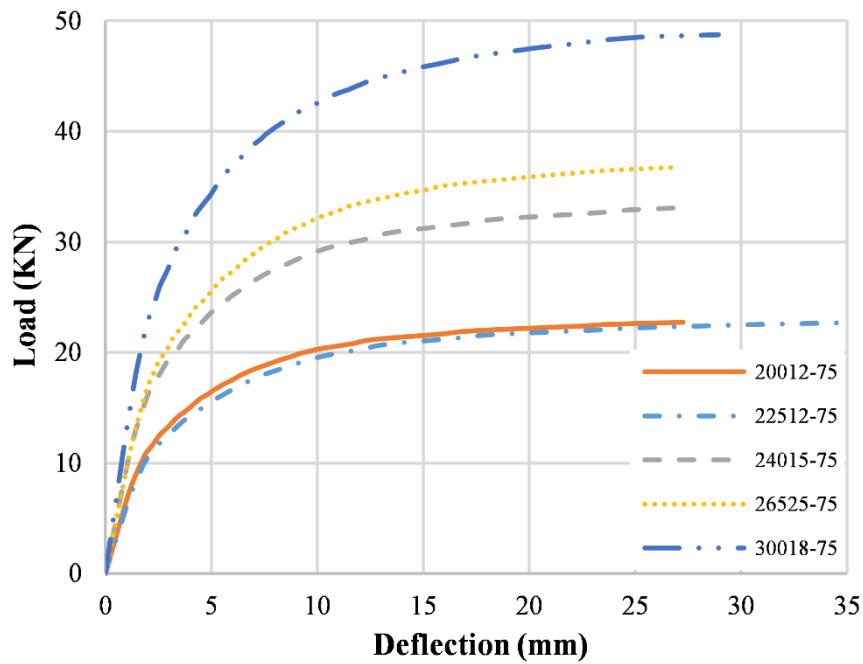
Figure 6.8 load-deformation response obtained from the first-order analysis.

6.3.3 Assessment and improvement of design guidance

The north American specifications NAS S100-16 (AISI, 2016) specifies the unified empirical equation given in Equation 6.1 to determine web crippling capacity of different cross-sections for all four loading condition.

$$R_w = Ct^2 f_y sin\theta \left(1 - C_r \sqrt{\frac{r}{t}}\right)\left(1 + C_N \sqrt{\frac{N}{t}}\right)\left(1 - C_w \sqrt{\frac{h_w}{t}}\right)$$ (6.1)

As it is in the NAS S100-16 (AISI, 2016), Equation 6.1 is not applicable to sections having stiffened webs such as sigma sections. Sundararajah et al. (2018) conducted experimental and numerical investigations on SupaCee sections, which are C-sections with four web stiffeners, under IOF and EOF loading conditions to assess the applicability of Equation 6.1. They compared experimental and numerical data against the NAS S100-16 predictions and found a reasonably good agreement. Sundararajah et al. (2018) also proposed a new set of dimensionless coefficients for SupaCee sections, shown in Table 6.3.

The applicability of the dimensionless coefficients given in the NAS S100-16 (AISI, 2016) and those proposed by Sundararajah et al. (2018) for SupaCee sections to Sigma sections is assessed herein. The accuracy of the predictions can be seen in Table 6.4 where it is observed that the predictions from the NAS S100-16 overestimate web crippling capacities (i.e mean ratio greater than 1), whilst reasonably good predictions are achieved by Sundararajah et al. (2018) recalibrated proposal though the scatter is relatively high. The reason why Equation 6.1 provides more scattered predictions for both sets of dimensionless coefficients is the negligence of effect of the folded webs on the web crippling strength. In other words, Equation 6.1 will give the same predictions for cross-section with the same web slenderness (h/t) regardless the middle to total web depth ratios (h_2/h). Therefore, the north American specifications NAS S100-16 (AISI, 2016) is adapted herein by adding an extra term $\left(1 + C_{h1}\sqrt{\frac{h_1}{h_w}}\right)$ that accounts for the presence of fold lines in a web as given in Equation 6.2. The term consists of the outer web coefficient C_{h1} and the outer web over the flat web height ratio (h_1/h_w). Furthermore, a new set of dimensionless coefficients for sigma sections

are proposed as shown in Table 6.3. It is clear that the Equation 6.2 with the proposal coefficients offer excellent agreements with experimental results and FE predictions for sigma sections. Also offering a significant reduction in the scatter of the predictions compared to Equation 6.1.

$$R_w = Ct^2 f_y \sin\theta \left(1 - C_r\sqrt{\frac{r}{t}}\right)\left(1 + C_N\sqrt{\frac{N}{t}}\right)\left(1 - C_w\sqrt{\frac{h_w}{t}}\right)\left(1 + C_{h1}\sqrt{\frac{h_1}{h_w}}\right) \qquad (6.2)$$

Table 6.3 web crippling coefficients.

Proposed by	C	C_r	C_N	C_w	C_{h1}
NAS S100-16 (2016)	13	0.23	0.14	0.01	
Sundararajah et al. (2018)	12.1	0.22	0.13	0.01	
The author	6.3	0.09	0.2	0.01	0.40

Table 6.4 Comparison of experimental and numerical results with predicted web crippling loads.

No.of tests: 6	NAS (AISI, 2016)		Sundararajah et al. (2018)		Proposed	
No. of FE models:189	$R_{w,pred}/R_{w,EXP}$	$R_{w,pred}/R_{w,FE}$	$R_{w,pred}/R_{w,EXP}$	$R_{w,pred}/R_{w,FE}$	$R_{w,pred}/R_{w,EXP}$	$R_{w,pred}/R_{w,FE}$
Mean	1.08	1.11	0.99	1.02	1.00	0.99
COV	0.18	0.11	0.17	0.11	0.09	0.05

It is worth noting that the EN 1993-1-3 (2006) approach has not been assessed herein because it is not applicable for sigma sections. The web crippling equations of EN 1993-1-5 are applicable webs with stiffeners, provided they are "folded in such a way that the two folds in the web are on opposite sides of the system line of the web joining the points of intersection of the midline of the web with the midlines of the flanges" (CEN, 2006a).

6.4 Slenderness-based design

6.4.1 Proposed strength curve for sigma sections

The obtained numerical results for the $R_{w,cr}$ and $R_{w,pl}$ loads are utilised to define the non-dimensional slenderness $\bar{\lambda}$ of the simulated sections, whilst the obtained web crippling strength R_w normalised by $R_{w,pl}$ defines the buckling reduction factor χ. Plotting the buckling reduction factor against the non-dimensional slenderness, a strong correlation can be observed in Figure 6.9. Hence, as for other buckling modes, the buckling reduction factor can be determined as a function of slenderness for sigma sections. Following a similar approach to that of (Duarte and Silvestre, 2013) and (Bock and Real, 2014) for channel sections and hat sections respectively, a strength curve for the web crippling resistance of sigma sections is proposed in Equation 6.3 and depicted in Figure 6.9.

$$\chi = \frac{R_w}{R_{w,pl}} = \frac{0.37}{\bar{\lambda}^{0,71}} \qquad (6.3)$$

It can be observed that, for the range of slenderness considered (i.e. $0.39 - 1.3$), the proposed strength curve provides an excellent fit to the obtained results, whilst it

follows a simple design framework similar to that adopted for other instability related failure modes. Key to the successful application of the design method based on strength curves is the prediction of the elastic critical buckling load $R_{w,cr}$ and the plastic load $R_{w,pl}$, as discussed hereafter.
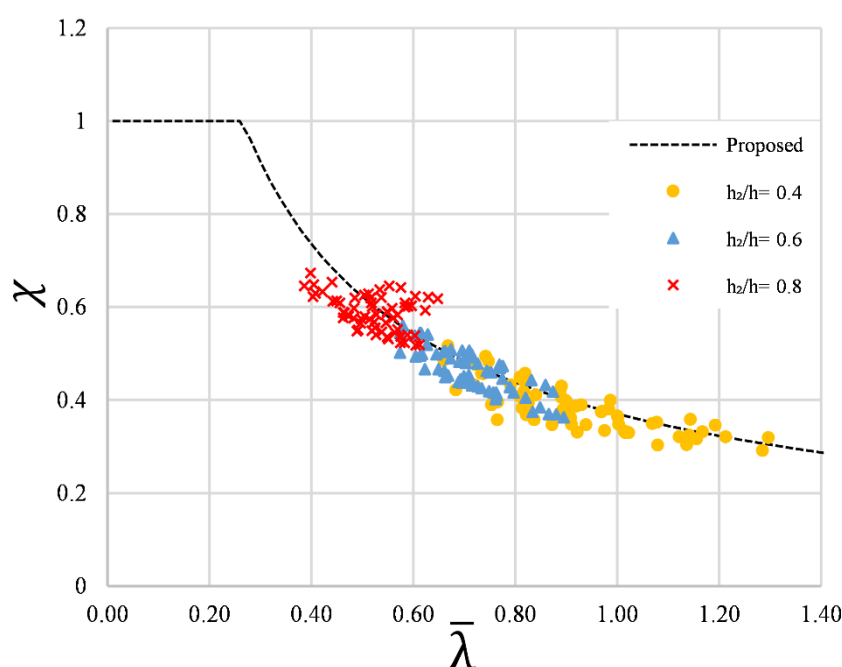
Figure 6.9 FE results and strength curve for sigma sections.

6.4.2 Predictive model for $R_{w,pl}$

Unlike the plastic resistance of a cross-section, the plastic resistance to web crippling $R_{w,pl}$ is not straightforward to obtain, however, several attempts have been conducted to predict the plastic resistance of web crippling theoretically (Bakker and Stark, 1994, Hofmeyer et al., 2002). Researchers have also developed analytical methods based on yield line mechanism (Zhao and Hancock, 1992, Zhao and Hancock, 1995, Gerges and Schuster, 1998, Hofmeyer, 2005b, Zhou and Young, 2006, Heurkens et al., 2018). While yield line mechanisms were adopted in (Duarte and Silvestre, 2013) and (Bock

and Real, 2014), due to the complex cross-sectional geometry an empirical approach is adopted in this study.

The empirical model defined by Equation 6.4 is proposed for the prediction of the plastic web crippling resistance of Sigma sections subjected to IOF loading. The accuracy of the obtained predictions can be assessed in Figure 6.10, where the predicted plastic resistances $R_{w,pl,pred}$ have been plotted against the numerical ones $R_{w,pl,FE}$. Overall, a reasonably good agreement between the predicted and the numerically obtained $R_{w,pl}$ is observed. The mean value of the predicted over the numerical $R_{w,pl}$ is 0.98 and the COV is 0.06.

$$R_{w,pl} = f_y \cdot \frac{3t\left[N+2.5\left[(h_1-2r_1)+2.5(t+r_1)\right]\right]}{16-2t} \qquad (6.4)$$
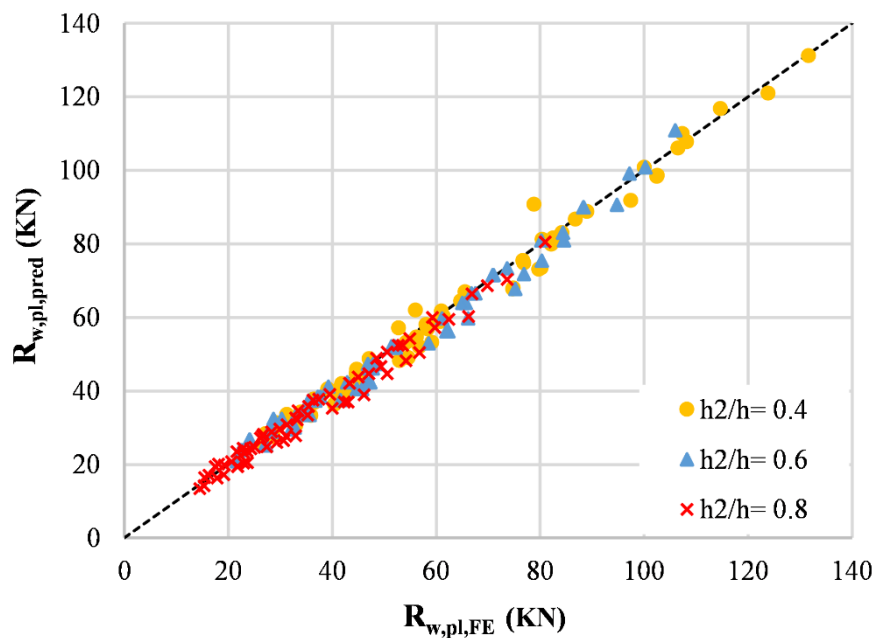
Figure 6.10 Predicted vs FE values for the plastic web crippling load $R_{w,pl}$.

6.4.3 Predictive model for $R_{w,cr}$

To the best of the author's knowledge there is no closed formed solution for the determination of the elastic critical buckling load for web crippling $R_{w,cr}$. It may be determined numerically using either the traditional finite element method as done in this study or the constrained shell finite element method (Ádány et al., 2018). The predictive model derived herein is based on the critical buckling load equation for plates subjected to in-plane loading given in Equation 6.5, where E is Young's modulus, t is the thickness of the plate, h is the width of the plate and k_f is a buckling factor. For Sigma sections, h was set equal to h_1 since the buckling mode shapes obtained from eigenvalue buckling analysis displayed very limited deformation of the middle and lower web, with the upper web experiencing most of the buckling deformations.

$$R_{w,cr} = k_f \cdot \frac{\pi^2 E t^3}{12(1-v^2)h} \tag{6.5}$$

A buckling factor k_f was therefore derived through multi-regression analysis as successfully done in (Duarte and Silvestre, 2013) and (Bock and Real, 2014). The main parameters considered in the multi-regression analysis included the section flange width over the upper web depth ratio b/h_1, the bearing width over the beam length ratio N/L, the overall depth over thickness ratio h/t, the ratio of the upper web depth over the overall section depth h_1/h and the mean root radius over thickness ratio $(0.5t + r_1)/t$. The derived buckling factor is presented in Equation 6.6 while a graphical assessment is shown in Figure 6.11, where the predicted buckling factor

$k_{f,pred}$ have been plotted against the numerical ones $k_{f,FE}$. The overall mean value of the predicted over the numerical $R_{w,cr}$ is 0.98 and the COV is 0.14.

$$k_f = -0.78\frac{b}{h_1} + 11.62\frac{N}{L} - 0.006\frac{h}{t} + 0.87\frac{h_1}{h} + 1.59\frac{r_i+0.5t}{t} \tag{6.6}$$
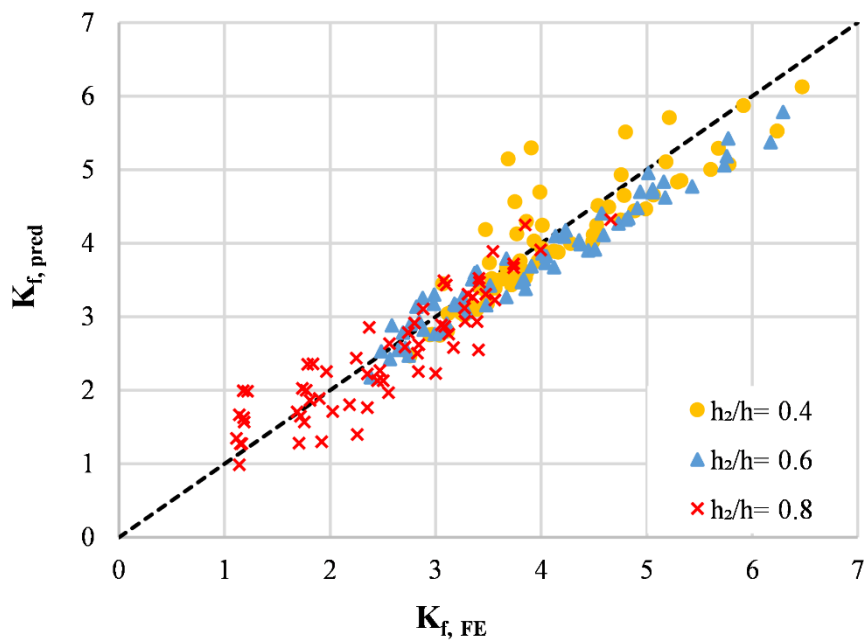
Figure 6.11 Predicted vs FE values for buckling factor k_f of the elastic critical web crippling load $R_{w,cr}$.

6.4.4 Assessment of the proposed method

Using the predictive models presented in Equations 6.4-6.6 and the derived strength curve given in Equations 6.3, the web crippling strength of Sigma sections subjected to IOF loading can be determined. The predicted web crippling strengths by the proposed method $R_{w,pred}$ are plotted against the numerical web crippling loads achieved by the full nonlinear models $R_{w,FE}$ in Figure 6.12 where overall an excellent

agreement can be observed with an average predicted over numerical web crippling strength of 1.00 and a COV of 0.07. Table 6.5 reports a breakdown of the average predicted over numerical web crippling strength for different data sets.
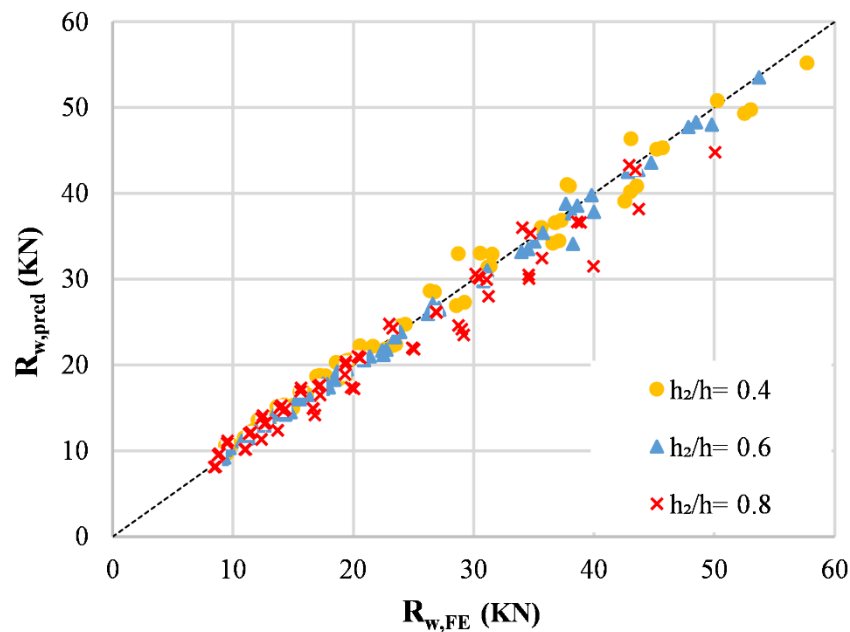
Figure 6.12 Predicted vs FE values for the web crippling load R_w of sigma sections.

Table 6.5 Assessment of design recommendations.

Web ratio (h₂/h)	$R_{w,pred}/R_{w,FE}$	
	Mean	COV
0.4	1.03	0.06
0.6	1.00	0.03
0.8	0.98	0.09
All	1.00	0.07

6.5 Summary

The development of an FE model for sigma sections failing by web crippling has been reported in this study. Based on validation of the FE model, parametric studies were conducted to generate additional data considering a wide range of cross-section geometries and a slenderness ranging from 0.39 to 1.3. The obtained results were used to assess the applicability of the north American specifications to sigma sections. It was found that the predictions of the north American specifications are unsafe for sigma sections, therefore, a modification has been proposed by introducing a new term to the original design equation to account for the presence of fold lines in a web.

The obtained results were also used to extend a slenderness-based design approach previously developed for channel sections and hat sections (Duarte and Silvestre, 2013, Bock and Real, 2014) to the design of sigma sections subjected to IOF. Empirical equations for the prediction of the plastic resistance and the elastic critical buckling load of sigma sections were reported and a new strength curve relating the slenderness to the web crippling reduction factor χ has been calibrated for sigma sections. The proposed method in Equations 6.3-6.6 gives excellent results within the range of parameters adopted for its calibration. The research presented in this chapter corroborates yet again that slenderness based approaches are possible for web crippling design.

Chapter 7: Conclusions and suggestions for future research

7.1 General

This thesis has investigated the structural response of laterally restrained cold-formed steel purlins with lipped Z-sections subjected to gravity loads with the view to determine the optimal lip size to flange width ratio that increases the effectiveness of cross-section and reduce the amount of material used as reported in Chapter 3 and 4. This thesis has also investigated the structural behaviour of cold-formed steel sigma section subjected to web crippling with the aim of assessing and improving the current design specifications, and expanding the slenderness-based design approach previously developed by Duarte and Silvestre (2013) and (Bock and Real, 2014) for the web crippling design as reported in Chapter 5 and 6.

Overall, 8 tests and 590 FE simulations have been conducted on Z-sections, whilst 6 tests and 189 FE simulations have been conducted on sigma-sections. The most important findings of this thesis are listed in the section 7.2, and suggestions for further research are made in section 7.3.

7.2 Main findings of the thesis

Most of tested Z-sections failed by local-distortional interaction, while two tested Z-sections displayed pure distortional buckling. The support conditions applied in the experimental tests and in particular the use of angle struts/anti-sag bars and the attachment of cladding to the top flange provided sufficient lateral and torsional restrain to the purlin since no lateral torsional buckling was observed during testing.

In all tested Z-sections, failure occurred at moments below the elastic moment resistance of the cross-section with the exception of most stocky specimen, which

exceeded its elastic moment resistance. The more slender (i.e. thinner) Z-sections display linear structural response with minimal loss of stiffness prior to the attainment of the ultimate load, whilst for the thicker Z-sections stiffness gradually decreases as a result of yielding prior to failure and the response becomes more curved near the ultimate load.

The test results of Z-sections were used to develop and generate FE modal using Abaqus. Four modelling strategies were established to examine the effect of angle struts and cladding on structural response and moment resistance of the cross-section. In the first modelling strategy, the simplified model, both angel struts and cladding modelled as boundary conditions, whilst the other three either one of the angel struts and cladding explicitly modelled or both. It was found that all modelling strategies have an excellent agreement with the experimental results, however, the simplified model has been selected for the rest of the study since modelling explicit struts and/or cladding would provide the marginal enhancements in accuracy with considerable increase in computational cost.

Since most of the tested Z-sections failed by the interaction of local and distortional buckling, employing a pure imperfection mode, whether local or distortional, would result in worse agreement with the test results. Therefore, the incorporation of initial geometric imperfections pertinent to both local and distortional buckling is necessary so that the observed response can be accurately replicated. During the validation of the FE model of zed-section, imperfection sensitivity was studied in detail and the most appropriate imperfection amplitudes and combinations of local and distortional buckling mode shapes have been selected and adopted in the parametric studies.

Parametric studies were conducted on a wide range of current Albion Section Z-sections to investigate whether the current lip size to flange width ratio is the optimal one or it should be modified to increase the cross-section efficiency. To this end, different lip size to flange width ratios (d/b) were considered in the parametric studies. These ratios are within the limits specified in Eurocode 3 (CEN, 2006a) (i.e.0.2≤ d/b ≤ 0.6). For most of sections, small lip size to flange width ratios (i.e. d/b ≤ 0.28) leads to decreased efficiency by about 8%, whilst lip size to flange width ratios above 0.4 leads to improved efficiencies particularly for deeper sections, for which gains in the region of 5% can be achieved. It is noteworthy that the optimal d/b ratio is not significantly affected by the adopted material model.

The obtained experimental and numerical results of Z-sections were also used to assess the applicability of Eurocode 3 (CEN, 2006a, CEN, 2006b) as well as the Direct strength method (DSM) (AISI, 2016). Both design methods were found to offer reasonably good ultimate capacity predictions, however, the DSM leads to more favourable ultimate capacity predictions and reduced scatter.

The failure mode for all the six tested sigma sections was web crippling, however, the patterns of deformation differed. For the thinner sigma sections, deformations occurred only within the upper web and the top part of the middle web, whereas for the thicker sigma sections, deformations were distributed throughout the whole upper and middle web apart from one specimen in which web crippling took place only within the upper web.

A numerical model of sigma section was developed and validated against the experimental results. The numerical model showed the capability of predicting web

crippling resistance and corresponding failure mode of cold-formed steel lipped sigma sections subjected to interior one flange loading. Therefore, the model has been unitised in parametric studies.

Parametric were studies carried out on a wide range of sigma sections having three middle to total web depth ratios (h_2/h): 0.4, 0.6 and 0.8. Three different analyses have been conducted namely, eigenvalue analysis to obtain the critical buckling load $R_{w,cr}$, first-order plastic analysis to obtain the plastic load $R_{w,pl}$ and geometrically and materially nonlinear analysis to obtain the web crippling resistance R_w.

It was found that the web crippling resistance increases with increasing the outer web depth of sigma sections. Furthermore, the current North American specification NAS S100-16 (AISI, 2016) has been assessed using the obtained experimental and numerical results of sigma sections. The assessment revealed that the North American specification is unsafe for sigma section since its predictions are overestimated. In absence of design guidance for sections with folded webs, the NAS specification was augmented by adding an extra term that accounts for the presence of fold lines in a web.

The Eurocode 3 method (CEN, 2006a, CEN, 2006b) cannot be applied to sigma sections because one of its criteria dose not satisfied, which is the folded web stiffeners should be in such a manner that "the two folds in the web are on opposite sides of the system line of the web joining the points of intersection of the midline of the web with the midlines of the flanges" (CEN, 2006a).

A strength curve was proposed for web crippling resistance sigma sections using the obtained numerical results. Since the critical buckling load and the plastic buckling load can be only determined numerically, an empirical equation has been proposed for plastic buckling load, while for critical buckling load a web was idealized as simply

supported thin rectangular plates along the edges, undergoing locally distributed in-plane edge compressive forces, so that the current equations for critical buckling load of plate can be used as well for web. A buckling factor of plate was derived through multi-regression analysis. The contribution of this study has been to confirm that slenderness-based approach can be successfully unitised for web crippling design.

7.3 Suggestions for future research

This thesis has addressed some significant issues regarding increasing the efficiency of cold-formed steel lipped Z-section purlin via determining the optimal lip size to flange width ratio, and the structural behaviour of sigma section subjected to web crippling. Further research is underway for sigma sections subjected to combined web crippling and bending moment, however, due to Covid-19 the test still incomplete. Therefore, it was not included in this thesis. There are still many possible areas of future research as a direct continuation of the research reported herein, as listed below:

- In this thesis the determination of optimal lip size to flange ratio of cold-formed steel Z-section has been achieved in absence of lateral tortional buckling. However, in some cases lateral tortional buckling might be present, therefore, further research should be carried out to determine the optimal lip size to flange ratio of unrestrained or partially restrained Z-section purlins.

- The structural behaviour of sigma sections subjected to exterior one flange loading (EOF), interior two flange loading (ITF) and exterior two flanges loading (ETF) remains unverified; hence further experimental and numerical research addressing these loading arrangements is warranted.

- When point loads are applied to unstiffened webs of purlins spanning over moderate distances an interaction between bending and web crippling occurs. To this end, the experimental tests reported in Chapter 5 should be repeated on similar specimens but with longer spans so that the interaction between bending and web crippling can be studied and the design equation of EN 1993-1-3 assessed.

- In this project only cold-formed steel sections with a yield (or nominal yield) strength of 450 MPa have been considered. Both experimental and numerical research is needed on sigma section made of different materials such as aluminium and stainless steel and subjected to web crippling or the interaction of bending and web crippling.

- Finally, further experimental and numerical research is necessary to extend the scope of slenderness-based design approach to study the web crippling strength of purlins employing cross-section geometries other than the sigma section considered herein.

References

References

Abdel-Rahman, N. and Sivakumaran, K. (1997) Material properties models for analysis of cold-formed steel members. *Journal of Structural Engineering, 123*(9), pp. 1135-1143.

Ádány, S., Visy, D. and Nagy, R. (2018) Constrained shell Finite Element Method, Part 2: application to linear buckling analysis of thin-walled members. *Thin-Walled Structures, 128*, pp. 56-70.

Adeli, H. and Karim, A. (1997) Neural network model for optimization of cold-formed steel beams. *Journal of Structural Engineering, 123*(11), pp. 1535-1543.

AISI (2007) *North American specification for the design of cold-formed steel structural members,* American Iron & Steel Institute, Committee of Steel Plate Producers ….

AISI, A. (2016) S100. *North Amercian Specifications for the Design of Cold-Formed Steel Structural Members. AISI S100-16, American Iron and Steel Institute, Washington, DC*.

Albion Sections. Z-purlin, cladding rail and Eaves beams technical manual. (2019). Albion sections [Accessed at: http://albionsections.co.uk/doc/52.pdf].

Alsanat, H., Gunalan, S., Guan, H., Keerthan, P. and Bull, J. (2019) Experimental study of aluminium lipped channel sections subjected to web crippling under two flange load cases. *Thin-Walled Structures, 141*, pp. 460-476.

American, I. and Steel, I. (1969) *Specification for the design of cold-formed stainless steel structural members: cold-formed steel design manual, Cold-formed steel design manual,* New York, N.Y.: American Iron and Steel Institute.

Anbarasu, M. (2016) Local-distortional buckling interaction on cold-formed steel lipped channel beams. *Thin-Walled Structures, 98*, pp. 351-359.

AS/NZS (2005) Cold-formed steel structures. in: Standards Australia Sydney, Australia.

Baehre, R. (1975) Sheet metal panels for use in building construction–Recent research projects in Sweden. in *Proceeding of the third international specialty conference on cold formed steel structures*.

Bähr, G. (1978) EINE EINFACHE ABSCHAETZUNG DER AUFNEHMBAREN ENDAUFLAGERKRAEFTE VON STAHL-TRAPEZLOLECHPROFILEN.

Bakker, M., Rosmanit, M. and Hofmeyer, H. (2008) Approximate large-deflection analysis of simply supported rectangular plates under transverse loading using plate post-buckling solutions. *Thin-Walled Structures, 46*(11), pp. 1224-1235.

Bakker, M. C. and Stark, J. W. (1994) Theoretical and experimental research on web crippling of cold-formed flexural steel members. *Thin-Walled Structures, 18*(4), pp. 261-290.

Batista, E. d. M. and Rodrigues, F. (1992) Residual stress measurements on cold-formed profiles. *Experimental Techniques, 16*(5), pp. 25-29.

Becque, J. and Rasmussen, K. J. (2013) Stability of Z-Section Purlins Used as Temporary Struts during Construction. *Journal of Structural Engineering, 139*(12), pp. 04013009.

Beshara, B. and Schuster, R. (2000) Web crippling data and calibrations of cold-formed steel members. *Final Report, University of Waterloo, Waterloo, Canada*.

Bhakta, B. H., LaBoube, R. A. and Yu, W.-w. (1992) The effect of flange restraint on web crippling strength.

Bock, M., Arrayago, I., Real, E. and Mirambell, E. (2013) Study of web crippling in ferritic stainless steel cold formed sections. *Thin-Walled Structures, 69*, pp. 29-44.

Bock, M., Mirada, F. and Real, E. (2015) Statistical evaluation of a new resistance model for cold-formed stainless steel cross-sections subjected to web crippling. *International Journal of steel structures, 15*(1), pp. 227-244.

Bock, M. and Real, E. (2014) Strength curves for web crippling design of cold-formed stainless steel hat sections. *Thin-Walled Structures, 85*, pp. 93-105.

Bock, M., Theofanous, M., Dirar, S. and Raybone, P. (2019) Assessment of web crippling design provisions for application to proprietary soldier beams. in *Structures*: Elsevier. pp. 147-156.

Bryan, G. H. (1890) On the Stability of a Plane Plate under Thrusts in its own Plane, with Applications to the "Buckling" of the Sides of a Ship. *Proceedings of the London Mathematical Society, s1-22*(1), pp. 54-67.

Bulson, P. S. (1970) *The Stability of Flat Plates,* Chatto and Windus.

Cain, D. E., LaBoube, R. A. and Yu, W.-w. (1995) The effect of flange restraint on web crippling strength of cold-formed steel Z-and I-sections.

CEN. (2006a) Eurocode 3: design of steel structures, Part 1.3: General rules—supplementary rules for cold formed members and sheeting. *Brussels: European Comittee for Standardization*.

CEN. (2006b) Eurocode 3: Design of Steel Structures, part 1-5: Plated structural elements. *Brussels: European Comittee for Standardization*.

Chen, M.-T. and Young, B. (2019) Material properties and structural behavior of cold-formed steel elliptical hollow section stub columns. *Thin-Walled Structures, 134*, pp. 111-126.

Chen, M.-T., Young, B., Martins, A. D., Camotim, D. and Dinis, P. B. (2020) Uniformly bent CFS lipped channel beams experiencing local-distortional interaction: Experimental investigation. *Journal of Constructional Steel Research, 170*, pp. 106098.

Chen, Y., Chen, X. and Wang, C. (2015) Experimental and finite element analysis research on cold-formed steel lipped channel beams under web crippling. *Thin-Walled Structures, 87*, pp. 41-52.

Dawson, R. G. and Walker, A. C. (1972) Post-buckling of geometrically imperfect plates. *Journal of the Structural Division, 98*(1), pp. 75-94.

Desmond, T. P. (1977) THE BEHAVIOR AND STRENGTH OF THIN-WALLED COMPRESSION ELEMENTS WITH LONGITUDINAL STIFFENERS.

Desmond, T. P., Winter, G. and Pekoz, T. (1981a) Edge stiffeners for thin-walled members. *Journal of the Structural Division, 107*(2), pp. 329-353.

Desmond, T. P., Winter, G. and Pekoz, T. (1981b) Intermediate stiffeners for thin-walled members. *Journal of the Structural Division, 107*(4), pp. 627-648.

Dinis, P. B. and Camotim, D. (2010) Local/distortional mode interaction in cold-formed steel lipped channel beams. *Thin-Walled Structures, 48*(10-11), pp. 771-785.

Doerich, C. and Rotter, J. (2011) Accurate determination of plastic collapse loads from finite element analyses. *Journal of pressure vessel technology, 133*(1).

Doran, D. and Cather, B. (2013) *Construction materials reference book,* Routledge.

Dos Santos, G., Gardner, L. and Kucukler, M. (2018) A method for the numerical derivation of plastic collapse loads. *Thin-Walled Structures, 124*, pp. 258-277.

Duarte, A. and Silvestre, N. (2013) A new slenderness-based approach for the web crippling design of plain channel steel beams. *International Journal of steel structures, 13*(3), pp. 421-434.

Dubina, D. and Ungureanu, V. (2002) Effect of imperfections on numerical simulation of instability behaviour of cold-formed steel members. *Thin-Walled Structures, 40*(3), pp. 239-262.

Dubina, D., Ungureanu, V. and Landolfo, R. (2012) Design of Cold-formed Steel Structures: Eurocode 3: Desgin of Steel Structures. in: ECCS-European Convention for Constructional Steelwork.

Dwight, J. (1963) Aluminum sections with lipped flanges and their resistance to local buckling. in *Proceedings*.

Gallaher, G. L. and Boughan, R. B. (1947) A method of calculating the compressive strength of Z-stiffened panels that develop local instability.

Gardner, L. and Cruise, R. (2009) Modeling of residual stresses in structural stainless steel sections. *Journal of Structural Engineering, 135*(1), pp. 42-53.

Gardner, L. and Nethercot, D. A. (2004) Experiments on stainless steel hollow sections—Part 1: Material and cross-sectional behaviour. *Journal of Constructional Steel Research, 60*(9), pp. 1291-1318.

Gardner, L., Talja, A. and Baddoo, N. (2006) Structural design of high-strength austenitic stainless steel. *Thin-Walled Structures, 44*(5), pp. 517-528.

Gerges, R. R. and Schuster, R. (1998) Web crippling of single web cold formed steel members subjected to end one-flange loading.

Gunalan, S. and Mahendran, M. (2015) Web crippling tests of cold-formed steel channels under two flange load cases. *Journal of Constructional Steel Research, 110*, pp. 1-15.

Haidarali, M. R. and Nethercot, D. A. (2011) Finite element modelling of cold-formed steel beams under local buckling or combined local/distortional buckling. *Thin-Walled Structures, 49*(12), pp. 1554-1562.

Haidarali, M. R. and Nethercot, D. A. (2012) Local and distortional buckling of cold-formed steel beams with edge-stiffened flanges. *Journal of Constructional Steel Research, 73*, pp. 31-42.

Hancock, G. (1997) Design for distortional buckling of flexural members. *Thin-Walled Structures, 27*(1), pp. 3-12.

Hancock, G. J. (1978) Local, Distortional, and Lateral Buckling of I-Beams. *Journal of the Structural Division, 104*(11), pp. 1787-1798.

Hancock, G. J. (1985) Distortional buckling of steel storage rack columns. *Journal of Structural Engineering, 111*(12), pp. 2770-2783.

Hancock, G. J. and Pham, C. H. (2015) Buckling analysis of thin-walled sections under localised loading using the semi-analytical finite strip method. *Thin-Walled Structures, 86*, pp. 35-46.

Hetrakul, N. and Yu, W. (1978) Structural behavior of beam webs subjected to web crippling and a combination of web crippling and bending. *Final report, civil engineering study*, pp. 78-4.

Heurkens, R., Hofmeyer, H., Mahendran, M. and Snijder, H. (2018) Direct strength method for web crippling—Lipped channels under EOF and IOF loading. *Thin-Walled Structures, 123*, pp. 126-141.

Hill, H. (1944) *Determination of stress-strain relations from offset yield strength values*: ALUMINUM CO OF AMERICA PITTSBURGH PA.

Hofmeyer, H. (2005a) Cross-section crushing behaviour of hat-sections (Part I: Numerical modelling). *Thin-Walled Structures, 43*(8), pp. 1143-1154.

Hofmeyer, H. (2005b) Cross-section crushing behaviour of hat-sections (Part II: Analytical modelling). *Thin-Walled Structures, 43*(8), pp. 1155-1165.

Hofmeyer, H. and Bakker, M. (2008) Sheeting interaction failure, from yield-line to two-strip model. *Thin-Walled Structures, 46*(7-9), pp. 839-847.

Hofmeyer, H., Kerstens, J., Snijder, H. and Bakker, M. (1999) Numerical and Analytical Modelling of Hat-section Web Crippling Behaviour. *Acta Polytechnica, 39*(5), pp. 87-104.

Hofmeyer, H., Kerstens, J., Snijder, H. and Bakker, M. (2001) New prediction model for failure of steel sheeting subject to concentrated load (web crippling) and bending. *Thin-Walled Structures, 39*(9), pp. 773-796.

Hofmeyer, H., Kerstens, J., Snijder, H. and Bakker, M. (2002) Combined web crippling and bending moment failure of first-generation trapezoidal steel sheeting. *Journal of Constructional Steel Research, 58*(12), pp. 1509-1529.

HORNE, M. and MERCHANT, W. (1965) The stability of frames(Book on elastic stability of plane rigid-jointed triangulated and nontriangulated frames). *OXFORD-NEW YORK, PERGAMON PRESS, 1965. 179 P*.

Ingvarsson, L. (1975) Cold-forming residual stresses effect on buckling.

Janarthanan, B., Mahendran, M. and Gunalan, S. (2019a) Numerical modelling of web crippling failures in cold-formed steel unlipped channel sections. *Journal of Constructional Steel Research, 158*, pp. 486-501.

Janarthanan, B., Sundararajah, L., Mahendran, M., Keerthan, P. and Gunalan, S. (2019b) Web crippling behaviour and design of cold-formed steel sections. *Thin-Walled Structures, 140*, pp. 387-403.

Kaitila, O. (2007) Web crippling of thin-walled cold formed steel cassettes. *Journal of Constructional Steel Research, 63*(6), pp. 766-778.

Karren, K. W. (1967) Corner properties of cold-formed shapes. *Journal of the Structural Division, 93*(1), pp. 401-433.

Karren, K. W. and Winter, G. (1967) Effects of Cold-Forming on Light-Gage Steel Members. *Journal of the Structural Division, 93*(1), pp. 433-469.

Kwon, Y. B. and Hancock, G. J. (1992) Tests of cold-formed channels with local and distortional buckling. *Journal of Structural Engineering, 118*(7), pp. 1786-1803.

Kyvelou, P., Gardner, L. and Nethercot, D. A. (2018) Finite element modelling of composite cold-formed steel flooring systems. *Engineering structures, 158*, pp. 28-42.

LaBoube, R. A. (1984) Simplified design approach for laterally braced purlins subjected to wind uplift.

Langan, J. E., LaBoube, R. A. and Yu, W.-w. (1994) Structural behavior of perforated web elements of cold-formed steel flexural members subjected to web crippling and a combination of web crippling and bending.

Lau, S. C. and Hancock, G. J. (1987) Distortional buckling formulas for channel columns. *Journal of Structural Engineering, 113*(5), pp. 1063-1078.

Lee, J., Kim, S.-M., Park, H.-S. and Woo, B.-H. (2005) Optimum design of cold-formed steel channel beams using micro Genetic Algorithm. *Engineering structures, 27*(1), pp. 17-24.

Lee, J., Kim, S.-M. and Park, H. S. (2006) Optimum design of cold-formed steel columns by using micro genetic algorithms. *Thin-Walled Structures, 44*(9), pp. 952-960.

Leng, J., Guest, J. K. and Schafer, B. W. (2011) Shape optimization of cold-formed steel columns. *Thin-Walled Structures, 49*(12), pp. 1492-1503.

Leng, J., Li, Z., Guest, J. K. and Schafer, B. W. (2014) Shape optimization of cold-formed steel columns with fabrication and geometric end-use constraints. *Thin-Walled Structures, 85*, pp. 271-290.

Li, H.-T. and Young, B. (2017a) Cold-formed ferritic stainless steel tubular structural members subjected to concentrated bearing loads. *Engineering structures, 145*, pp. 392-405.

Li, H.-T. and Young, B. (2017b) Tests of cold-formed high strength steel tubular sections undergoing web crippling. *Engineering structures, 141*, pp. 571-583.

Li, H.-T. and Young, B. (2018) Design of cold-formed high strength steel tubular sections undergoing web crippling. *Thin-Walled Structures, 133*, pp. 192-205.

Li, Z., Ádány, S. and Schafer, B. (2013) Modal identification for shell finite element models of thin-walled members in nonlinear collapse analysis. *Thin-Walled Structures, 67*, pp. 15-24.

Li, Z. and Schafer, B. W. (2010) Buckling analysis of cold-formed steel members with general boundary conditions using CUFSM conventional and constrained finite strip methods.

Liew, A. and Gardner, L. (2015) Ultimate capacity of structural steel cross-sections under compression, bending and combined loading. in *Structures*: Elsevier. pp. 2-11.

Liu, H., Igusa, T. and Schafer, B. (2004) Knowledge-based global optimization of cold-formed steel columns. *Thin-Walled Structures, 42*(6), pp. 785-801.

Lundquist, E. E., Stowell, E. Z. and Schuette, E. H. (1943) Principles of moment distribution applied to stability of structures composed of bars or plates.

Ma, J.-L., Chan, T.-M. and Young, B. (2015) Material properties and residual stresses of cold-formed high strength steel hollow sections. *Journal of Constructional Steel Research, 109*, pp. 152-165.

Macdonald, M., Don, M. H., KoteŁko, M. and Rhodes, J. (2011) Web crippling behaviour of thin-walled lipped channel beams. *Thin-Walled Structures, 49*(5), pp. 682-690.

Macdonald, M., Heiyantuduwa, M. and Rhodes, J. (2008) Recent developments in the design of cold-formed steel members and structures. *Thin-Walled Structures, 46*(7-9), pp. 1047-1053.

Martins, A. D., Camotim, D. and Dinis, P. B. (2017a) Local-distortional interaction in cold-formed steel beams: Behaviour, strength and DSM design. *Thin-Walled Structures, 119*, pp. 879-901.

Martins, A. D., Landesmann, A., Camotim, D. and Dinis, P. B. (2017b) Distortional failure of cold-formed steel beams under uniform bending: Behaviour, strength and DSM design. *Thin-Walled Structures, 118*, pp. 196-213.

Mirambell, E. and Real, E. (2000) On the calculation of deflections in structural stainless steel beams: an experimental and numerical investigation. *Journal of Constructional Steel Research, 54*(1), pp. 109-133.

Moen, C. and Schafer, B. (2006) Stability of cold-formed steel columns with holes. in *Proc. of the Int. colloquium on stability and ductility of steel structures. Lisbon, Portugal*. pp. 697-704.

Moen, C. and Schafer, B. (2011) Direct strength method for design of cold-formed steel columns with holes. *Journal of Structural Engineering, 137*(5), pp. 559-570.

Moharrami, M., Louhghalam, A. and Tootkaboni, M. (2014) Optimal folding of cold formed steel cross sections under compression. *Thin-Walled Structures, 76*, pp. 145-156.

Natário, P., Silvestre, N. and Camotim, D. (2014) Web crippling failure using quasi-static FE models. *Thin-Walled Structures, 84*, pp. 34-49.

Natário, P., Silvestre, N. and Camotim, D. (2016) Direct strength prediction of web crippling failure of beams under ETF loading. *Thin-Walled Structures, 98*, pp. 360-374.

Nguyen, V. B., Pham, C. H., Cartwright, B. and English, M. (2017) Design of new cold rolled purlins by experimental testing and Direct Strength Method. *Thin-Walled Structures, 118*, pp. 105-112.

Nguyen, V. V., Hancock, G. J. and Pham, C. H. (2017a) Analyses of thin-walled sections under localised loading for general end boundary conditions–Part 1: Pre-buckling. *Thin-Walled Structures, 119*, pp. 956-972.

Nguyen, V. V., Hancock, G. J. and Pham, C. H. (2017b) New developments in the direct strength method (DSM) for the design of cold-formed steel sections under localised loading. *Steel Construction, 10*(3), pp. 227-233.

Pham, C. H. and Hancock, G. J. (2009) Direct strength design of cold-formed purlins. *Journal of Structural Engineering, 135*(3), pp. 229-238.

Quach, W., Teng, J. and Chung, K. (2006) Finite element predictions of residual stresses in press-braked thin-walled steel sections. *Engineering structures, 28*(11), pp. 1609-1619.

Ramberg, W. and Osgood, W. R. (1943) Description of stress-strain curves by three parameters.

Rasmussen, K. J. (2003) Full-range stress–strain curves for stainless steel alloys. *Journal of Constructional Steel Research, 59*(1), pp. 47-61.

Real, E., Arrayago, I., Mirambell, E. and Westeel, R. (2014) Comparative study of analytical expressions for the modelling of stainless steel behaviour. *Thin-Walled Structures, 83*, pp. 2-11.

Reinsch, W. (1983) *Das Kantenbeulen zur rechnerischen Ermittlung von Stahltrapezblech-Trägern,* Technische Hochschule.

Ren, W.-X., Fang, S.-E. and Young, B. (2006) Finite-element simulation and design of cold-formed steel channels subjected to web crippling. *Journal of Structural Engineering, 132*(12), pp. 1967-1975.

Rhodes, J. (1991) *Design of cold formed steel members,* Elsevier Applied Science London and New York.

Rhodes, J. and Nash, D. (1998) An investigation of web crushing behaviour in thin-walled beams. *Thin-Walled Structures, 32*(1-3), pp. 207-230.

Roberts, T. and Jhita, P. (1983) Lateral, local and distortional buckling of I-beams. *Thin-Walled Structures, 1*(4), pp. 289-308.

Santaputra, C., Parks, M. B. and Yu, W.-w. (1986) Web crippling strength of high strength steel beams.

Schafer, B. and Peköz, T. (1998) Computational modeling of cold-formed steel: characterizing geometric imperfections and residual stresses. *Journal of Constructional Steel Research, 47*(3), pp. 193-210.

Schafer, B. W. (2000) *Distortional buckling of cold-formed steel columns.*

Schafer, B. W. (2019) Advances in the Direct Strength Method of cold-formed steel design. *Thin-Walled Structures, 140*, pp. 533-541.

Schafer, B. W., Li, Z. and Moen, C. D. (2010) Computational modeling of cold-formed steel. *Thin-Walled Structures, 48*(10-11), pp. 752-762.

Schafer, B. W. and Pekoz, T. (1998) Direct strength prediction of cold-formed steel members using numerical elastic buckling solutions.

Schafer, B. W. and Peköz, T. (1999) Laterally braced cold-formed steel flexural members with edge stiffened flanges. *Journal of Structural Engineering, 125*(2), pp. 118-127.

Schafer, B. W. and Trestain, T. (2002) Interim design rules for flexure in cold-formed steel webs.

Sharp, M. L. (1966) Longitudinal stiffeners for compression members. *Journal of the Structural Division, 92*(5), pp. 187-212.

Sharp, M. L. (1989) Behavior of Plates Under Partial Edge Loading. in *Steel Structures*: ASCE. pp. 215-224.

Shifferaw, Y. and Schafer, B. (2012) Inelastic bending capacity of cold-formed steel members. *Journal of Structural Engineering, 138*(4), pp. 468-480.

Simulia (2014) Abaqus user manual 6.14. in: Simulia Providence, RI.

Sivakumaran, K. (1989) Analysis for web crippling behaviour of cold-formed steel members. *Computers & Structures, 32*(3-4), pp. 707-719.

Southwell, R. V. (1932) On the analysis of experimental observations in problems of elastic stability. *Proceedings of the Royal Society of London. Series A, Containing Papers of a Mathematical and Physical Character, 135*(828), pp. 601-616.

Studnicka, J. (1990) Web crippling of wide deck sections.

Sundararajah, L., Mahendran, M. and Keerthan, P. (2016) Experimental studies of lipped channel beams subject to web crippling under two-flange load cases. *Journal of Structural Engineering, 142*(9), pp. 04016058.

Sundararajah, L., Mahendran, M. and Keerthan, P. (2018) Design of SupaCee sections subject to web crippling under one-flange load cases. *Journal of Structural Engineering, 144*(12), pp. 04018222.

Theofanous, M. and Gardner, L. (2012) Effect of element interaction and material nonlinearity on the ultimate capacity of stainless steel cross-sections. *Steel & Composite Structures, 12*(1), pp. 73-92.

Thomasson, P.-O. (1978) THIN-WALLED C-SHAPED PANELS IN AXIAL COMPRESSION.

Timoshenko, S., P, T. S., Gere, J. M., Gere, J. G. and Young, D. (1961) *Theory of Elastic Stability,* McGraw-Hill.

Uzzaman, A., Lim, J. B., Nash, D., Rhodes, J. and Young, B. (2012a) Cold-formed steel sections with web openings subjected to web crippling under two-flange loading conditions—Part II: Parametric study and proposed design equations. *Thin-Walled Structures, 56*, pp. 79-87.

Uzzaman, A., Lim, J. B., Nash, D., Rhodes, J. and Young, B. (2012b) Web crippling behaviour of cold-formed steel channel sections with offset web holes subjected to interior-two-flange loading. *Thin-Walled Structures, 50*(1), pp. 76-86.

Uzzaman, A., Lim, J. B., Nash, D., Rhodes, J. and Young, B. (2013) Effect of offset web holes on web crippling strength of cold-formed steel channel sections under end-two-flange loading condition. *Thin-Walled Structures, 65*, pp. 34-48.

Vaessen, M. (1995) On the elastic web crippling stiffness of thin-walled cold-formed steel members. *The Netherlands: Department of Structural Design, Eindhoven University of Technology*.

Van Der Maas, C. J. (1954) Charts for the calculation of the critical compressive stress for local instability of columns with hat sections. *Journal of the Aeronautical Sciences, 21*(6), pp. 399-403.

Van der Neut, A. (1969) The interaction of local buckling and column failure of thin-walled compression members. in *Applied Mechanics*: Springer. pp. 389-399.

Vieira Jr, L., Malite, M. and Schafer, B. W. (2010) Simplified models for cross-section stress demands on C-section purlins in uplift. *Thin-Walled Structures, 48*(1), pp. 33-41.

Von Kármán, T. (1932) The strength of thin plates in compression. *Trans. ASME, 54*, pp. 53-57.

Wang, J., Afshan, S., Gkantou, M., Theofanous, M., Baniotopoulos, C. and Gardner, L. (2016) Flexural behaviour of hot-finished high strength steel square and rectangular hollow sections. *Journal of Constructional Steel Research, 121*, pp. 97-109.

Weng, C. C. and Pekoz, T. (1990) Residual stresses in cold-formed steel members. *Journal of Structural Engineering, 116*(6), pp. 1611-1625.

Willis, C. T. and Wallace, B. (1990) Behavior of cold-formed steel purlins under gravity loading. *Journal of Structural Engineering, 116*(8), pp. 2061-2069.

Wing, B. (1981) *Web Crippling and the Interaction of Bending and Web Crippling of Unreinforced Multi-Web Cold Formed Steel Sections. MA Sc*. Unpublished, Thesis, University of Waterloo, Canada.

Winter, G. (1947) Strength of thin steel compression flanges. *Trans. ASCE, 112*, pp. 527.

Winter, G. and Pian, R. (1946) *Crushing strength of thin steel webs*.

Wu, S., Yu, W.-w. and LaBoube, R. A. (1997) Strength of flexural members using structural grade 80 of A653 steel (web crippling tests).

Yang, D. and Hancock, G. J. (2004) Compression tests of high strength steel channel columns with interaction between local and distortional buckling. *Journal of Structural Engineering, 130*(12), pp. 1954-1963.

Yang, J. and Liu, Q. (2012) An experimental study into flexural behaviour of sigma purlins attached with roof sheets. *Engineering structures, 45*, pp. 481-495.

Ye, J., Hajirasouliha, I., Becque, J. and Eslami, A. (2016) Optimum design of cold-formed steel beams using Particle Swarm Optimisation method. *Journal of Constructional Steel Research, 122*, pp. 80-93.

Ye, J., Meza, F. J., Hajirasouliha, I., Becque, J., Shepherd, P. and Pilakoutas, K. (2019) Experimental investigation of cross-sectional bending capacity of cold-formed steel channels subject to local-distortional buckling interaction. *Journal of Structural Engineering, 145*(7), pp. 04019064.

Ye, J., Mojtabaei, S. M., Hajirasouliha, I., Shepherd, P. and Pilakoutas, K. (2018) Strength and deflection behaviour of cold-formed steel back-to-back channels. Engineering structures, 177, pp. 641-654.

Young, B. and Hancock, G. J. (2001) Design of cold-formed channels subjected to web crippling. *Journal of Structural Engineering, 127*(10), pp. 1137-1144.

Young, B. and Zhou, F. (2008) Aluminum tubular sections subjected to web crippling—Part II: Proposed design equations. *Thin-Walled Structures, 46*(4), pp. 352-361.

Yousefi, A. M., Lim, J. B. and Clifton, G. C. (2017a) Web bearing capacity of unlipped cold-formed ferritic stainless steel channels with perforated web subject to end-two-flange (ETF) loading. *Engineering structures, 152*, pp. 804-818.

Yousefi, A. M., Uzzaman, A., Lim, J. B., Clifton, G. C. and Young, B. (2017b) Web crippling strength of cold-formed stainless-steel lipped channels with web perforations under end-two-flange loading. *Advances in Structural Engineering, 20*(12), pp. 1845-1863.

Yu, C. and Schafer, B. W. (2003) Local buckling tests on cold-formed steel beams. *Journal of Structural Engineering, 129*(12), pp. 1596-1606.

Yu, C. and Schafer, B. W. (2006) Distortional buckling tests on cold-formed steel beams. *Journal of Structural Engineering, 132*(4), pp. 515-528.

Yu, C. and Schafer, B. W. (2007) Simulation of cold-formed steel beams in local and distortional buckling with applications to the direct strength method. *Journal of Constructional Steel Research, 63*(5), pp. 581-590.

Yu, W.-w. (1981) Web crippling and combined web crippling and bending of steel decks.

Yu, W.-W., LaBoube, R. A. and Chen, H. (2010) *Cold-formed steel design,* Wiley Online Library.

Zeinoddini, V. and Schafer, B. (2012) Simulation of geometric imperfections in cold-formed steel members using spectral representation approach. *Thin-Walled Structures, 60*, pp. 105-117.

Zetlin, L. and Winter, G. (1952) 65th. and 66th. progress reports on light gauge steel beams of coldformed steel, unpublished. *Ithaca: Cornell University*.

Zhao, X.-L. and Hancock, G. J. (1992) Square and rectangular hollow sections subject to combined actions. *Journal of Structural Engineering, 118*(3), pp. 648-667.

Zhao, X.-L. and Hancock, G. J. (1995) Square and rectangular hollow sections under transverse end-bearing force. *Journal of Structural Engineering, 121*(9), pp. 1323-1329.

Zhou, F. and Young, B. (2006) Yield line mechanism analysis on web crippling of cold-formed stainless steel tubular sections under two-flange loading. *Engineering structures, 28*(6), pp. 880-892.

Zhou, F. and Young, B. (2007a) Experimental and numerical investigations of cold-formed stainless steel tubular sections subjected to concentrated bearing load. *Journal of Constructional Steel Research, 63*(11), pp. 1452-1466.

Zhou, F. and Young, B. (2007b) Experimental investigation of cold-formed high-strength stainless steel tubular members subjected to combined bending and web crippling. *Journal of Structural Engineering, 133*(7), pp. 1027-1034.

Zhou, F. and Young, B. (2008) Aluminum tubular sections subjected to web crippling—Part I:: Tests and finite element analysis. *Thin-Walled Structures, 46*(4), pp. 339-351.